1-1-1984

Linear polarization and total flux density of silicon monoxide masers and active extragalactic objects at millimeter wavelengths.

Richard Barvainis
University of Massachusetts Amherst

LINEAR POLARIZATION AND TOTAL FLUX DENSITY OF SILICON MONOXIDE MASERS AND ACTIVE EXTRAGALACTIC OBJECTS AT MILLIMETER WAVELENGTHS

A Dissertation Presented

by

RICHARD EDWARD BARVAINIS

Submitted to the Graduate School of the
University of Massachusetts in partial fulfillment
of the requirements for the degree of

DOCTOR OF PHILOSOPHY

February 1984

Physics and Astronomy

LINEAR POLARIZATION AND TOTAL FLUX DENSITY

OF SILICON MONOXIDE MASERS AND ACTIVE EXTRAGALACTIC

OBJECTS AT MILLIMETER WAVELENGTHS

A Dissertation Presented

by

RICHARD EDWARD BARVAINIS

Approved as to style and content by:

William A. Dent

Dr. William A. Dent,
Chairperson of Committee

Dr. George S. Greenstein, Member

David J. Van Blerkom

Dr. David J. Van Blerkom, Member

R. Krotkov

Dr. Robert V. Krotkov, Member

Dr. LeRoy F. Cook, Department Head
Physics and Astronomy

ACKNOWLEDGEMENTS

Four score and seven years ago... no, it only seems that long since the day I walked into Bill Dent's office and asked him what I might do for a thesis. When he suggested observations of millimeter-wave polarization of quasars, little did I realize the timescale and effort involved in developing new instrumentation (a polarimeter), in testing, in developing observing techniques, and in carrying out two large observing projects at the FCRAO. But I also didn't envision how valuable and enriching an experience this would be, and how much I would learn in the process.

First, I would like to thank Bill for giving me direction, and for sharing his knowledge, experience, and friendship over the course of the dissertation. Second, I would like to extend my appreciation to Read Predmore, for pushing for the development of the polarimeter, for teaching me about millimeter instrumentation and techniques, both in the lab and out at Quabbin, and for his time and energy in collaborating on the observing projects.

I would also like thank my thesis committee, as well as the faculty of the Five College Astronomy Department, who have provided a congenial and stimulating atmosphere in which to study and do research. John Kwan, Nick Scoville, David Van Blerkom, and Gene Tademaru in particular have provided helpful discussions and critical readings of manuscripts. The FCRAO scheduling committee has been most generous in providing telescope time for the various projects I have been involved

in, especially those reported in this dissertation. I also thank the FCRAO leadership (G. Richard Huguenin, Paul Goldsmith, and Nick Scoville) for supporting me as a research assistant. Special thanks are due Antal Hartai and John Karakla, for their excellent work in building the polarimeter, and to John Kapitzky for programming support at Quabbin.

Finally, I would like to thank my friends, and fellow graduate students, for making my years here so enjoyable. George Greenstein and Barbara Kunhardt provided me with a "home away from home," where I could always count on finding a warm fire and even warmer friendship. Steve (Rienos) Lord and Naka Ishii kept my spirits up and shared countless dinners, giving me sustenance to work long into the night. For their friendship and encouragement throughout the course of this work, I thank Andrea Hoffman, Randy and Doug Deihl, Jane Niedjalik, Cynthia Patterson, Greg Hartke, Happy Robey, Dan Clemens, Tom Balonek, and especially Jill Franks, who shared with me the difficulties of the final crunch of finishing up the thesis.

ABSTRACT

LINEAR POLARIZATION AND TOTAL FLUX DENSITY
OF SILICON MONOXIDE MASERS AND ACTIVE EXTRAGALACTIC
OBJECTS AT MILLIMETER WAVELENGTHS

(February 1984)

Richard E. Barvainis

B.A., State University College at Buffalo

M.S., Ph.D., University of Massachusetts

Directed by: Professor William A. Dent

In order to investigate the linear polarization properties of millimeter-wave radio sources, a polarimeter was constructed for use on the Five College Radio Astronomy Observatory 14m telescope. Linear polarization and total flux density observations of SiO masers (at 43 and 86 GHz) and active extragalactic objects (at 87 GHz) were conducted, resulting in the first multitransitional study of SiO maser polarization, and the first rapid time sampling (days to weeks) of extragalactic source polarization at millimeter wavelengths.

Measurements of sixteen active extragalactic objects were made over a seven month period; the millimeter polarization variations are qualitatively similar to those seen at centimeter wavelengths. Two rapid and closely spaced outbursts with rise timescales of about one week were seen in OJ287. For 3C345, observed variations in the polarization may indicate the propagation of radiating particles along a jet.

The 87 GHz total flux density measurements are combined with simultaneous centimeter-wave data to derive broadband spectra, which

are compared to the predictions of a relativistic Maxwellian electron distribution model and a power law electron inhomogeneous jet model. A relativistic blast wave model for source variability incorporating a Maxwellian particle distribution is discussed.

Analysis of polarization in up to four masing transitions of SiO in late-type stars and the Orion source indicates that emission from the same rotational transition in different vibrational states often arises in the same volume of gas, but that masers in different rotational transitions within the same vibrational state arise in different regions. An inverse correlation is found between maser fractional polarization and stellar envelope expansion velocity.

A model is developed to explain the observed polarization and total intensity profiles of the Orion masers. The profiles can be simply accounted for by maser emission from a rotating and expanding disk, with an azimuthally dependent magnetic field orientation.

TABLE OF CONTENTS

LIST OF TABLES

LIST OF ILLUSTRATIONS

CHAPTER I

INTRODUCTION

A diverse set of astronomical objects is discussed in this dissertation, one whose members differ widely in age, luminosity, size and distance, as well as in other fundamental aspects. They include late-type stars, a region of star formation, and compact variable quasars. Although disparate in many ways, these phenomena have at least one characteristic in common, that is, they emit polarized radiation at millimeter wavelengths. It is this characteristic which defines the main theme of this dissertation.

The study of polarization is an important avenue of astronomical investigation. Since electromagnetic waves are our primary means of studying astronomical objects, all of the information contained in the radiation field is of value, and the polarized component can sometimes be substantial. Most astronomical observations are conducted without regard to polarization, either because the radiation is known to be unpolarized, the polarization is not germane to a particular study, or the instrumentation and techniques for its measurement are not available. But when possible, the study of polarization can provide unique insight into astrophysical conditions and processes. For instance, an important line of evidence that extragalactic radio sources emit by the synchrotron mechanism is the fact that their radiation is polarized.

The techniques for measuring polarization have been well

established in the optical and in the radio centimeter to meter wavelength bands. However, little work in this field has been done at millimeter wavelengths until fairly recently, mostly due to the scarcity and relative insensitivity of millimeter telescopes, and the specialized technology needed for millimeter polarimetry. For this dissertation, a millimeter wavelength polarimeter was developed for the Five College Radio Astronomy Observatory (FCRAO) 14 m telescope. The polarimeter was used to observe linear polarization in line radiation from Silicon Monoxide (SiO) masers in the vicinity of late-type stars and in the Orion nebula, and in the continuum radiation of compact variable extragalactic sources (quasars, BL Lacertae objects, and a Seyfert galaxy).

We will not follow the usual course of reviewing the topics of study in detail in this introductory chapter, which would be impractical because of the broad range of information that would have to be presented. Instead, each chapter will be self-contained, including background material appropriate to the subject at hand and concluding sections wherein the results of the chapter are reviewed and discussed.

Chapter II will be concerned with the instrumentation and observational techniques for measuring millimeter polarization, developed in collaboration with the FCRAO staff. Since this is a relatively new area of research, the methodology will be described in some detail.

Chapters III and IV will present observations of SiO masers and their interpretation. The former will be devoted primarily to results of the study of masers around late-type stars. In the latter, a model to explain the observations of the Orion masers will be proposed. It

will be shown that a rotating and expanding disk of maser emission can account for the polarization, total intensity profiles, and interferometry measurements of these unique masers.

Variable extragalactic sources will be discussed in Chapters V and VI. Measurements of rapid time variability in total flux density and linear polarization at 87 GHz will be presented and discussed in Chapter V. Chapter VI will be the only chapter not directly concerned with polarization. Instead, the $\lambda 3.5$mm total flux measurements of Chapter V will be combined with simultaneous measurements at centimeter wavelengths to form broadband spectra for thirteen sources. These will be compared with the predictions of current models for explaining the often broad and flat spectra observed. Finally in Chapter VI, a model, based upon the relativistic blast wave theory of Blandford and McKee (1976 and 1977), will be developed and used to account for some aspects of the observed total flux variations of the BL Lac object 0235+164.

CHAPTER II

POLARIMETRY AT FCRAO

§1. Introduction and General Principles

The principles of millimeter-wave polarimetry do not differ fundamentally from those employed in other wavelength regimes of the electromagnetic spectrum, but the techniques used to put these principles into practice are rather specific to the millimeter band. In this chapter these principles will be discussed, together with their application to continuum and spectral line polarization observations at FCRAO. The work presented in this dissertation is confined to the study of linear polarization, because the amount of circular polarization to be found in the radiation of millimeter sources has either been predicted, or has been observed, to be quite small. The measurement of circular polarization would be possible at FCRAO with minor modifications of the existing instrumentation, but will not be discussed further here.

In general, three quantities are sufficient to fully specify the linear polarization properties of an electromagnetic wave. These quantities take on several different representations depending upon the circumstances of their measurement and application, and the whim of the user, but all of course provide the same information. One such representation is in terms of the following: the total flux density, S_T, which is the sum of the polarized plus unpolarized components of

the wave; the linearly polarized flux density, S_p; and the position angle, χ, of the electric vector of the linearly polarized component (which is defined as increasing eastward from north on the celestial sphere). Instead of flux densities, one might specify the total and polarized intensities or antenna temperatures (e.g., for spectral line measurements). In some situations a quantity more physically relevant than the polarized flux is the fractional polarization, defined as $m = S_p / S_T$.

Although the above quantities are intuitively straightforward in interpretation, they are sometimes difficult to measure directly and are cumbersome to use in calculations. Furthermore, the polarized flux density (or fractional polarization) suffers from noise statistics which are non-Gaussian in character (see below). An alternative complete set of quantities are the Stokes parameters, which are free of these disadvantages but are less intuitively meaningful in many circumstances. It is a simple matter to interchange one set of parameters for another. This is accomplished via the definitions of the linear Stokes parameters (see, e.g., Kraus 1965):

$$I = S_T \qquad \text{(II-1a)}$$

$$Q = S_p \cos 2\chi \qquad \text{(II-1b)}$$

$$U = S_p \sin 2\chi . \qquad \text{(II-1c)}$$

Both sets of parameters will be used where appropriate throughout this dissertation. The polarized flux density, fractional polarization, and position angle can be found from I, Q, and U using

$$S_P = (Q^2 + U^2)^{1/2} \qquad \text{(II-2a)}$$

$$m = (Q^2 + U^2)^{1/2} / I \qquad \text{(II-2b)}$$

$$\chi = 1/2 \tan^{-1} U/Q. \qquad \text{(II-2c)}$$

A direct measurement of the Stokes parameters can be accomplished by measuring the flux density of the source with the reciever polarization oriented along position angles 0° (North), 45° (Northeast), 90° (East), and 135° (Southeast). Sums and differences of these measurements are then taken to form the Stokes parameters:

$$I = S_0 + S_{90} = S_{45} + S_{135} \qquad \text{(II-3a)}$$

$$Q = S_0 - S_{90} \qquad \text{(II-3b)}$$

$$U = S_{45} - S_{135}. \qquad \text{(II-3c)}$$

In principle only three measurements are needed, since $S_{135} = I - S_{45}$, but in practice it was found that a minimum of eight position angles must be sampled in order to remove instrumental effects. The nature of these effects and the methods by which they are corrected will be discussed in some detail in the sections to follow.

The measurement of polarization in the presence of noise is biased by the fact that S_P is a positive definite quantity. Although the noise on Q and U may be Gaussian, the vector amplitude S_P will be larger than its true value when noise is present. This effect can be corrected to good approximation by a formula given in Wardle and Kronberg (1974). With S_P and S_P' the true and measured values of

polarized flux density, respectively, and σ the measured uncertainty in S_P',

$$S_P = S_P'\{1 - (\sigma/S_P')^2\}^{1/2} \quad . \qquad \text{(II-4)}$$

All of the polarization measurements reported in this dissertation have been corrected in this way. In cases where $\sigma \geq S_P'$, S_P has been set to zero. In spectral line measurements, the correction has been performed on a channel by channel basis.

§2. Telescope and Receivers

The FCRAO telescope is a 13.7 m diameter parabolic reflector with a Cassegrain focus. The dish is enclosed in a radome which transmits about 84% of the radiation incident on it into the main beam at 87 GHz. During the 1981-82 observing season (when the QSO observations were performed) the aperture efficiency (η_A) of the telescope, including losses due to the radome and polarimeter, was about 0.38 at 87 GHz. This number varied by about 5-10% during the observing season, based upon calibrations using the planets and the compact HII region DR21. The antenna half power beamwidth (HPBW) was 65". During the 1980-81 season (when the SiO maser observations were performed), η_A was somewhat lower, about 0.30 at 87 GHz. Between the 1980-81 and 1981-82 seasons the illumination of the subreflector was improved, hence the higher efficiency in 1981-82. Observations of SiO masers were also made at 43 GHz in the spring of 1981. At this frequency $\eta_A \cong 0.48$, and the HPBW was 120". Since the antenna panel resetting in the summer of 1980 the antenna gain has not shown a significant dependence on

elevation, for elevations between 15° and 70° (Balonek 1982). All measurements were made within this elevation range.

The receivers used at FCRAO are single channel systems with feed horns sensitive to linear polarization. Three different recievers were used over the course of the observations, and are described below.

3mm cooled receiver (1980-81). The 86 GHz observations of SiO masers in the J=2-1, v=1 and v=2 transitions were conducted using a cooled receiver with a Schottky diode mixer and a 4.75 GHz parametric amplifier IF of 400 MHz bandwidth. A quasi-optical beam processing system was used in conjunction with this receiver to provide capabilities for chopper wheel calibration, beam chopping, sideband rejection, and polarimetry. The configuration of the major components in this system is given in Figure II-1. The single-sideband (SSB) receiver temperature was about 500 K.

Although this receiver produced acceptable results in spectral line polarimetry mode, attempts to measure continuum polarization were unsuccessful due to a strong (~ 1%) modulation in the total power with a period of about one second. This period was found to be the same as that of the cooling refrigerator pump cycle, and presumably the total power modulation was due to variations in the parametric amplifier gain as the temperature in the receiver dewar varied within each pump cycle. At times the amplitude of the modulation was equivalent to several degrees in antenna temperature, or about two orders of magnitude larger than the antenna temperature of the polarization in a typical source.

7mm uncooled receiver (Spring 1981). The J=1-0 transitions of SiO

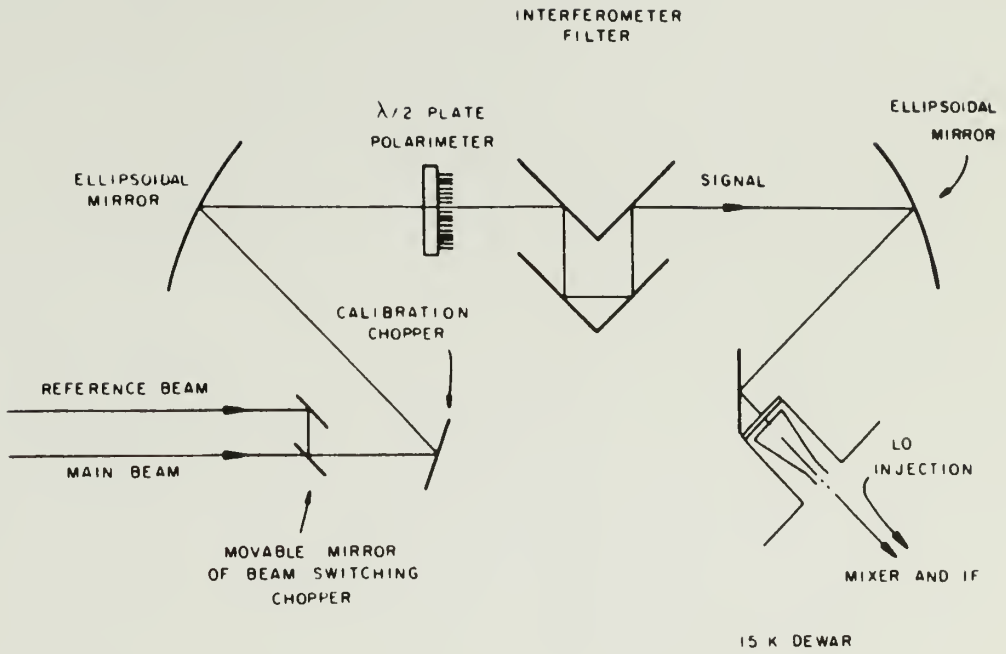

Fig.II-1. Diagram of the major components in the receiver quasi-optical beam path, including the location of the half-wave plate polarimeter. The Fabry-Perot interferometer filter was tuned to double sideband mode for the continuum observations, and was tuned single sideband for the spectral line measurements.

at 43 GHz were observed with an uncooled Spacecom mixer, without quasi-optics, with the feed mounted at the first waist of the antenna beam. The polarimeter and movable ambient temperature calibration load were mounted directly in front of the feed. The receiver IF frequency was 1.4 GHz, and all observations were made in double sideband mode with a receiver tempertature of about 350 K DSB.

3mm cooled receiver (1981-82). All of the observations of continuum polarization of extragalactic sources were made with this receiver, which was similar to the 3mm receiver described above, but with an important modification - the IF parametric amplifier was replaced by a 500 MHz bandwidth GaAs FET amplifier operating at 1.4 GHz. FET amplifiers are known to be very stable against temperature variations, and in this receiver the one second total power modulation seen previously was very weak or non-existent, providing a system with the necessary stability for sensitive continuum polarization measurements. Another significant improvement was a reduction of the receiver noise temperature to ~ 80 K DSB (160 K SSB). The quasi-optical system was the same as that shown in Figure II-1.

§3. The Polarimeter

In order to make the observations reported in this dissertation possible, it was first necessary to design and construct a linear polarimeter for use at FCRAO. The specification of the general working principles of the polarimeter and the design of the half-wave plate were done by the author and Drs. Read Predmore and Peter Schloerb. The mechanical and electronic design and construction of the polarimeter

are due to Antal Hartai and John Karakla. The polarimeter was originally intended principally for use with the cooled 3mm receiver, but was also adapted for use with the uncooled 7mm receiver.

In order to measure linear polarization in an astronomical source, it is necessary to sample the source strength at a number of polarization orientations (Equations II-3). This can be accomplished in a variety of ways:

1. The polarization orientation can be rotated by physically rotating either the feed alone or the entire receiver.
2. The orientation can be rotated using an "optically active" element such as a half-wave plate in the telescope beam.
3. On an az-el mounted telescope, the receiver polarization direction can remain fixed and the source can be observed at different parallactic angles as it moves across the sky. The parallactic angle is defined as the angle between a line of constant azimuth and the direction to north at the position of observation (see, e.g., Smart 1950). As the parallactic angle changes, the source appears to rotate.

The second approach above was chosen, because it was not possible to rotate the receiver, and relying upon parallactic angle changes was considered cumbersome and inefficient.

The FCRAO polarimeter, then, consists of a computer controlled, rotatable half-wave plate fabricated from rexolite (a microwave dielectric). Into a rexolite disk of 5" diameter have been cut an array of ~ 80 deep parallel grooves. The spacings between the grooves

are equal to the groove widths (1/32") resulting in a comb-like configuration of grooves/slats about 1 cm deep, supported by a backing of solid rexolite. By this method the dielectric is made to be anisotropic, and an incident linearly polarized wave will see different dielectric constants for the components of polarization along the "fast" and "slow" axes of the plate (perpendicular and parallel to the grooves, respectively). The depth of the grooves is such that a differential phase shift of 180° is obtained between the two components of polarization, and this depth depends upon the frequency of observation and the dielectric constant of the plate material. A linearly polarized wave will remain linearly polarized after this 180° phase shift, but such a wave would be converted to circular polarization if the shift were 90° (i.e., with a quarter-wave plate). The relevant equations for designing a half-wave plate by this method are given in Kirschbaum and Chen (1957).

The depth of the grooves for a half-wave plate is given by

$$d = \lambda_o \,/\, 2(\varepsilon_y^{1/2} - \varepsilon_x^{1/2}) \,, \qquad \text{(II-5)}$$

where λ_o is the free space wavelength. The ε's are dielectric constants along the y and x directions (parallel and perpendicular to the grooves), and are given by $\varepsilon_x = 2\varepsilon/(1 + \varepsilon)$, $\varepsilon_y = (1 + \varepsilon)/2$, where ε is the dielectric constant of the plate material. For rexolite we used $\varepsilon = 2.55$, a value which appears to be fairly constant from centimeter to infrared wavelengths. The factor 2 in the denominator of Equation II-5 should be replaced by 4 for a quater-wave plate. The width of the grooves and slats should be $< 1/3\ \lambda_o$.

With the half-wave plate as its active element, the remainder of the polarimeter consists of a support housing, a motor and chain drive system for rotating the plate, and an electronic servo system for accurately positioning the plate in response to digital commands from the main computer. The angular resolution is about 0.5°. The polarimeter is located in the 3mm cooled receiver quasi-optics as shown in Figure II-1.

A half-wave plate with the slow axis at position angle (PA) θ will rotate the PA of the electric vector of the incident linearly polarized wave to $\phi' = 2\theta - \phi$, where ϕ and ϕ' are the initial and final PAs referenced to the direction $\theta = 0$ (here vertical). Thought of in the broadcast sense, the polarization of a vertically polarized feed ($\phi_{feed} = 0$) will be rotated to PA $\phi'_{feed} = 2\theta$ on the sky, and any desired polarization orientation can be obtained by the appropriate choice of plate PA.

In measuring the polarization of astronomical sources, it is often desirable to obtain accuracies of less than 1% of the total source intensity. This requires very careful treatment of all instrumental effects which can bias the measurements at this level. One such effect is the generation of small amounts of linear polarization in an initially unpolarized wave by the antenna and radome structure. This can be corrected by observing strong sources which are known (or are at least assumed) to be unpolarized. Another effect which can seriously distort the measured polarization has its genesis in the half-wave plate itself, and is endemic to dielectric differential phase shifters in general. As discussed above, the components of a wave polarized

along the fast and slow axes of the plate encounter different indices of refraction, and hence suffer different reflection and transmission losses in passing through the plate. Even an unpolarized wave will be subject to this effect, since such a wave can be thought of as the sum of two orthogonal linearly polarized waves. Hence there is a variation in antenna temperature with plate PA proportional to the total flux of the source which, if not corrected, can mimic polarization.

As an example, consider an incident wave with intensity I_o and polarization parallel to the feed direction. Insert the half-wave plate into the beam with the fast axis parallel to the feed. Then the alignment of wave and feed polarizations will be retained, but the wave intensity will be reduced by some transmission factor T_{fast}, such that $I = I_o T_{fast}$. Then rotate the plate by 90°. This will rotate the polarization by 180°, and the wave and feed polarizations will still be aligned. However, since the wave now "sees" the index of refraction of the slow axis the transmission coefficient will be different, such that $I = I_o T_{slow}$. Hence the measured intensity in the two cases will be different by an amount $\Delta I = I_o(T_{fast} - T_{slow})$, resulting in a modulation of the measured source intensity with this amplitude.

The modulation has approximately the following form:

$$T(\theta) = \tfrac{1}{2}\alpha T_I(1 + \cos 2\theta), \qquad \text{(II-6)}$$

where $T(\theta)$ is the modulated antenna temperature, T_I is the antenna temperature corresponding to the total intensity of the source, and $\alpha \cong 0.03$. The methods by which this effect is removed from the continuum and spectral line polarization data will be discussed in

§4 and §5.

If there were no transmission losses, it would be possible, in principle, to design a plate in such a way that backward reflections would be eliminated completely along both plate axes. In fact the plates used for this program were designed to minimize reflections by making the thickness of the solid base of the plates equal to an integral number of wavelengths in rexolite. Nevertheless, the modulation of the source strength with plate PA was found to be rather large (of order 3% of I). This is probably due to the fact that the beam is not a plane parallel wave at the location of the polarimeter, but is in fact converging after reflection from an ellipsoidal mirror. The walkoff in each ray of the beam after reflection from the various plate surfaces probably lessens the effects of destructive interference necessary to eliminate reflections. In an attempt to reduce reflections, we tried adding a waffle pattern matching layer onto the solid rexolite side of a plate, but this resulted in no improvement. Contributing to the modulation is the differential attenuation of the fast and slow axes.

§4. Continuum Observations

Observations of the continuum polarization of active extragalactic sources were carried out between 29 November 1981 and 2 July 1982. The reciever LO was tuned within the frequency range 86.5 to 87.5 GHz, and the Fabry-Perot interferometer filter was tuned to double sideband mode. Typical system temperatures were between 250 and 300 K in clear

weather. The continuum backend consisted of a square law detector of nominal bandwidth 400 MHz. The true effective bandwidth was probably closer to 250 MHz, due to the irregular bandpass of the detector and the presence of some IF filteration prior to detection. The DC output voltage from the detector was integrated using one of the voltage-to-frequency converters of a 250 KHz x 256 channel filterbank.

In the observing technique employed, the polarimeter plate was rotated from $\theta = 5°$ to $\theta = 355°$, then back in the opposite direction, with a period of 1 or 2 seconds for 350° rotation. This back and forth method helps to remove linear drifts in receiver gain and sky emission. Although the computer commanded the polarimeter to move in 32 discrete steps per rotation, the motion was for all practical purposes continuous because of the short rotation periods used. The data were binned into 32 channels, with each channel then representing an average over 10.5° in plate position angle. This averaging results in a slight reduction in the polarization signal amplitude, but since this is only on the order of a few percent (of the polarized, not the total, intensity) it was ignored.

When used in conjunction with a linearly polarized feed, a continuously rotating plate will produce a modulation in the polarization signal of the form

$$T(\theta) = \tfrac{1}{2}T_p(1 + \cos(4\theta - 2\phi)), \qquad \text{(II-7)}$$

where $T(\theta)$ is the modulated antenna temperature and T_p is the antenna temperature corresponding to the polarized flux of the source. The angles θ and ϕ are as defined in §3. Plate PA 0° corresponds to

vertical, which is also the polarization direction of the feed. This angle was calibrated by observing the limb of the moon, which was assumed to be polarized in the radial direction. The instrumental calibration uncertainty in the derived source polarization PAs is estimated to be ± 1°.

There is a distinct advantage to polarization switching by continuous rotation of the plate, as opposed to the common technique of discrete switching by 90° in polarization sensitivity. This is because of the aforementioned instrumental effect of the half-wave plate due to the differential index of refraction along the fast and slow axes of the plate. The resulting modulation in antenna temperature is given in Equation II-6. Since this modulation is at a frequency different from that of the polarization signal it can easily be removed from the data, but only if a sufficient number of plate position angles are represented.

The observing technique for the polarization measurements consisted of ON-OFF sequences, rotating the plate on source for 40 seconds, and then off source for 40 seconds. Total flux information is inaccurate using this method, because the ON-OFF switching is far too slow to remove the effects of sky and reciever drift. Consequently, the total flux density was measured at the beginning and end of the polarization integration periods by beam switching at a rate of 10 Hz, in an ON-ON sequence (main beam on source, then reference beam on source). Scans were taken in two orthogonal polarizations to obtain the total (polarized plus unpolarized) flux density. The total flux density measurements were calibrated, and the pointing was checked, by

frequent observations of the planets and DR21 (assumed to have a flux density of 17.3 Jy at 87 GHz, W. Dent, private communication). Planetary brightness temperatures were taken from Ulich (1981). Antenna temperatures were calibrated, and atmospheric attenuation removed, by the standard chopper wheel method (Penzias and Burrus 1974). The total flux density measurements and calibration procedures are similar to those described in detail by Balonek (1982).

The 32 channels of polarization data were fit to the equation

$$T(\theta) = \tfrac{1}{2}T_p\cos(4\theta - 2\phi) + \gamma\cos 2\theta + C, \qquad \text{(II-8)}$$

which is just the sum of Equations II-7 and 6 where the DC terms have been combined in the constant C (which also includes the source total intensity, but is usually dominated by total power changes between the on and off source measurements). The free parameter γ corresponds to $\tfrac{1}{2}\alpha T_s$ from Equation II-6. On occasion another sinusoidal term was also removed if examination of the power spectrum of the 32 channels revealed the presence of a strong component at other than 2θ or 4θ. The polarization phase ϕ is a function of the parallactic angle, η, at the position of observation and the polarization position angle, χ, of the source: $\phi = \chi - \eta$. Derived uncertainties in T_p and χ are based upon the RMS scatter of the data about the fitted function. The induced instrumental polarization due to the antenna/radome structure was calibrated by observing Jupiter and Venus, which were assumed to be unpolarized. The magnitude of this effect was on the order of 0.3% of the total flux density, with an RMS variation from day to day of about 0.1%.

It was not possible to directly calibrate the polarized flux density scale because there are no sources of known polarized flux density in the sky at 87 GHz. It was therefore assumed that the antenna temperature to flux density conversion factor (calibration constant) for the polarized component was the same as that found for the total flux density. In practice, the calibration constant used to obtain the polarized flux density was not that found from beam switched measurements of the calibration sources, but was obtained instead from total power position switched measurements of the planets. It was found that the beam switched and position switched calibration constants were often somewhat different, and it was felt that the position switched calibration was subject to fewer systematic effects and probably better reflected the system response to polarized emission, because such a calibration is in the total power mode, as are the polarization measurements. It is difficult at this stage to estimate how much the polarized flux density measurements are biased by calibration errors resulting from this procedure, but the polarization measurements of the Crab Nebula and 3C274 are quite encouraging and will be discussed below.

The Crab Nebula was periodically used as a check of system performance, since it is the strongest polarized source in the sky, after the sun and moon, at λ3mm. A typical observation of the Crab Nebula polarization is shown in Figure II-2. Seven observations were made at the position of the pulsar, yielding a mean fractional polarization $m = 15.7 \pm 0.3\%$ and position angle $\chi = 155 \pm 1°$. This is in good agreement with what might be expected from the 23 GHz polarization map

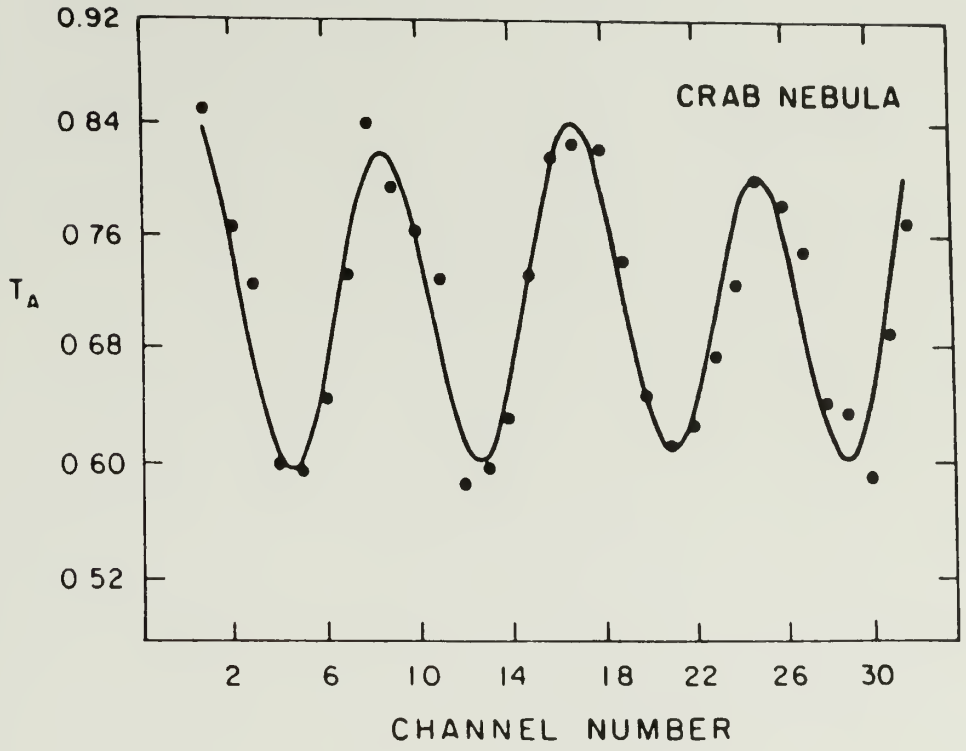

Fig.II-2. Typical observation of the Crab Nebula, showing 32 channels of polarization data and the fit to Eq.II-3 (solid line). Each channel represents an average over 10.5° in polarimeter plate position angle, and has been binned over many rotations of the plate. The peak-to-peak amplitude of the sinusoid represents the antenna temperature of the polarized signal.

of Wright and Forster (1980), from the λ9.55mm results of Hobbs (1968) and Johnston and Hobbs (1969), and from a map of the optical polarization (Wilson 1972). However, at 99 GHz Hobbs, Maran, and Brown (1978, hereafter HMB) obtained m = 11.8 ± 0.9% at χ = 122 ± 1°. This disagrees with the results found here, and those at other frequencies. Since they did not give the position at which their observations were made, a comparison of their results and those reported here is somewhat ambiguous.

For the (presumably) non-variable radio galaxy 3C274 (Virgo A), the fractional polarization was measured to be 5.2 ± 1.0% at position angle 27 ± 5°. The 99 GHz measurements of 3C274 by HMB have high errors (m = 1.6 ± 2.9%, χ = 33 ± 25°), but are statistically consistent with these results. The total flux density was found to be 7.85 ± 0.25 Jy, which is close to the value of 7.50 Jy expected at 87 GHz from the 30.4 and 90.0 GHz measurements of Ulich (1981). Hobbs and Waak (1972) discussed a model for the polarization in this source invoking Faraday rotation and depolarization effects, which predicts an intrinsic polarization of m_{int} = 3.6% and χ_{int} = 27°, based upon a rotation measure of 810 radm^{-2}. At 87 GHz, Faraday effects should be negligible, and the measurements given above are in fairly good agreement with the model prediction, especially considering the large uncertainties in the lower frequency data from which the model fit was obtained. The measured position angle of 27° is nearly orthogonal to the position angle of the optical jet at 292° (Vaucouleurs, Angione, and Fraser 1968), which is consistent with the emission being optically thin synchrotron radiation from a region in which the magnetic field is

aligned along the jet.

§5. Spectral Line Observations

In this section the basic observing techniques of line polarimetry will be discussed. The results of the SiO maser polarization program will be presented in the next chapter. The FCRAO telescope has also been used for polarimetry of thermal emission lines of ^{12}CO, ^{13}CO, and HCN in molecular clouds and circumstellar envelopes, with no positive detection of linear polarization (Wannier, Scoville, and Barvainis 1983).

The observations of the J=2-1 transitions of SiO were performed between January and June of 1981 with the single sideband system temperature, corrected to it's equivalent value outside the earth's atmosphere, typically 700 to 900 K. The observations of the J=1-0 transitions were carried out during the period 25-28 June 1981. Filterbank backends of 250 KHz and 100 KHz resolution were used for the J=1-0 observations. While both of these filterbanks were available for the May and June J=2-1 observations, only the 250 KHz filter bank was used from January to April. The rest frequencies assumed were 86.243270 GHz and 85.640305 Ghz for v=1 and 2, J=2-1, and 43.122027 GHz and 42.820539 GHz for v=1 and 2, J=1-0.

In at least one respect, line measurements have an advantage over continuum measurements in that simple variations in the total power of the system are broadband and have relatively little effect on the shape of a line profile. On the other hand, line data involve hundreds of spectral channels across the line profile and baseline. If one were to

use the continuum technique of continuous plate rotation, with the data binned into 32 polarization channels, then one would have to store 32 full spectra per observation. Furthermore, the 32 polarization bins would have to be fit to a function similar to equation II-8 for each spectral channel. Such a procedure would be rather difficult at FCRAO from a data management standpoint, so an alternative observing procedure was developed. This procedure consists of a direct measurement of the Stokes parameters for all spectral channels simultaneously.

The method is as follows. For the Q Stokes parameter, the polarization sensitivity is rapidly switched (usually at 1 Hz) between North (PA 0°) and East (PA 90°) on the sky and spectra for both of these directions are accumulated during the scan. Q is then just the difference spectrum north - east, as defined in Equation 11-3b. The Stokes parameter U is measured in a similar way, by switching between Northeast (PA 45°) and Southeast (PA 135°) as in Equation II-3c. Polarization switching by 90° is accomplished by switching the half-wave plate by 45°. The actual plate position angles needed to obtain the above polarizations on the sky depend on the parallactic angle of the source during the observation. Thus a parallactic angle compensation is automatically calculated and input into the observing program at the beginning of each scan.

The Stokes parameter I can be found by doing both on and off source scans, and then forming a (source - reference) / reference scan for each of the four polarization angles (Equation II-3a). Alternatively, the total flux density can be found by taking normal position switched spectra in orthogonal polarizations before or after the polarization

switched observations. In this case, only on source polarization observations need be made (unless the baselines are so bad that off source spectra are necessary to correct them). Generally, for the SiO maser observations, it was found to be most efficient to use this second method.

So far in this section, we have ignored the effects of the "2θ" modulation in source strength with plate PA (Equation II-6). Since polarization switching involves differencing spectra taken 45° apart in θ, this can bias the Stokes parameters by several percent. Fortunately, in this case there is a simple solution for correcting this instrumental effect. Note first that the same polarization on the sky is obtained for plate PAs θ and θ ± 90°. However, adding or subtracting 90° from θ results in a 180° change in the phase of the 2θ modulation. Therefore the effect can be cancelled to first order by averging two switched observations of the same Stokes parameter separated by 90° in plate PA. Thus for each polarization measurement four switched spectra were obtained - two complimentary spectra for Q, and two for U. We found that this technique adequately removed instrumental polarization down to the ½% level. It was at this level that a variable antenna and/or radome induced polarization was found in the course of previous continuum observing tests, and we made no attempt to correct for this in the spectral line measurements. As a check of the system, we measured the 88.63 GHz thermal HCN J=1-0 line in Orion, and found that it had no linear polarization greater than the sensitivity limit of about ½%.

The antenna temperatures for spectral line work were calibrated

using the standard chopper wheel method, and antenna temperatures were converted to Janskys by taking a mean calibration constants of 63 Jy/K at 86 GHz and 39 Jy/K at 43 GHz. It is estimated that absolute line fluxes are accurate to about 20%.

CHAPTER III

THE LINEAR POLARIZATION OF SiO MASERS

§1. Introduction

Linear polarization appears to be a common characteristic of SiO maser radiation. Troland et al. (1979) found eight of nine sources to be linearly polarized in the v=1, J=2-1 transition of SiO at 86.2 GHz, with typical fractional polarizations of 10-30%. Higher polarizations, near 100%, are also seen on occasion (Clarke, Troland, and Johnson 1982). In this chapter we present measurements of the linear polarization properties in the v=1, J=2-1 transition for several SiO maser sources over a six month period in 1981. We also present nearly simultaneous measurements of total flux density and polarization in four different SiO maser transitions (v=1 and v=2, J=1-0 and J=2-1) for the S-type long period variable star χ Cygni, and similar measurements in two and three transitions for six other sources. An energy level diagram for the SiO molecule, including the observed transitions, is given in Figure III-1.

A total of eight SiO maser sources were observed in the v=1, J=2-1 transition during the course of this program, with seven of these sources observed more than once between January and June 1981. The source list appears in Table III-1. All of these sources are associated with late-type stars except the Orion masers, which arise in the vicinity of the infrared source IRc2. The observations of most

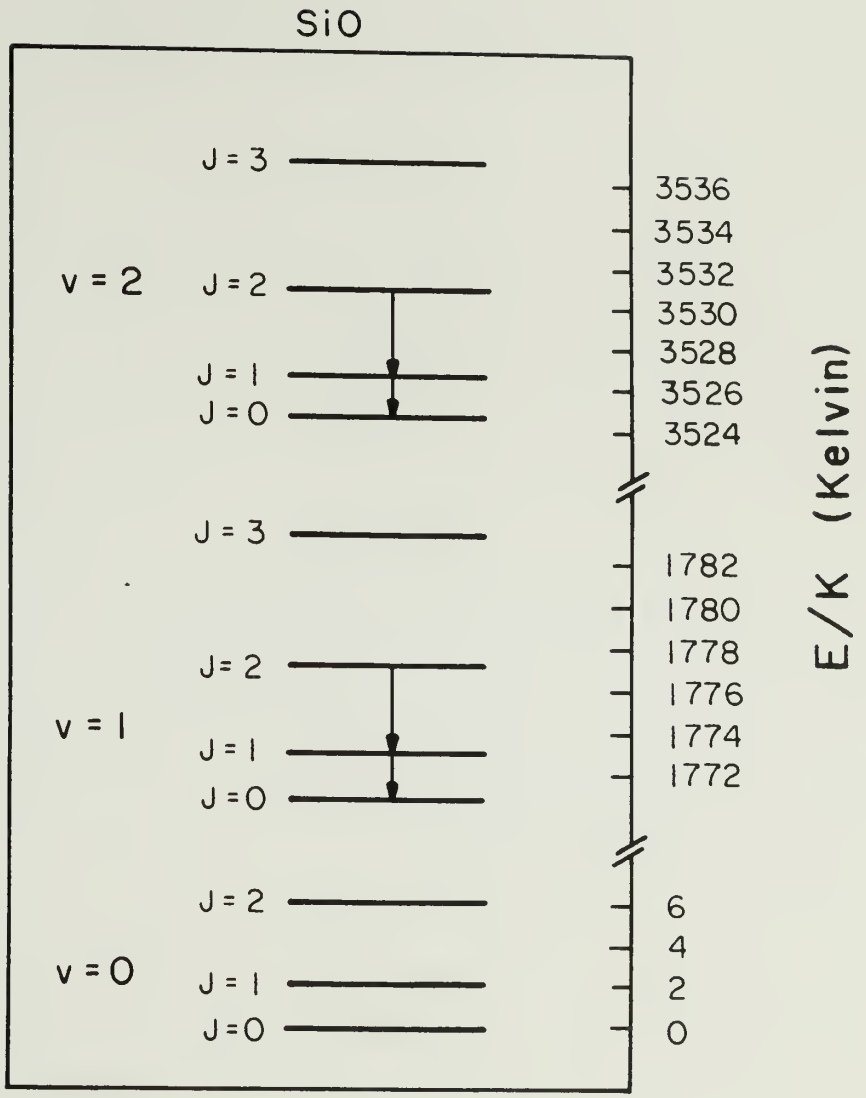

Fig.III-1. Energy level diagram for SiO rotation-vibration states. The rotational transitions observed are shown by arrows.

Table III-1

Source List

Source	α(1950) δ(1950)	Variable Type[a]	$V_{exp}(kms^{-1})$
IK Tau	$03^h50^m43^s7$ 11°15'30"	M	16.5 ±1.0 [b]
Orion	05 32 47.8 -05 24 08	-	17.5 1.0 [c]
VY CMa	07 20 54.6 -25 40 12	unclassified	36.7 2.0 [d]
R Leo	09 44 52.2 11 39 42	M	5.0 0.7 [d]
W Hya	13 46 12.2 -28 07 06	SRa(M?)	8.6 0.7 [d]
VX Sgr	18 05 03.0 -22 13 56	SRc	22.7 3.3 [d]
χ Cyg	19 48 38.0 32 47 12	M	7.5 1.0 [d]
R Cas	23 55 51.7 51 06 36	M	8.9 0.9 [d]

a Kukarkin et al. 1969
b Dickinson, Kollberg, and Yngvesson 1975 (uncertainties estimated)
c From separation of OH peaks (uncertainties estimated)
d Morris et al. 1979

sources are irregularly spaced, and some sources were observed more frequently than others. During observations on 9-12 June emission from v=2, J=2-1 was searched for in three sources (VX Sgr, R Cas, and χ Cygni) but significant total flux was detected only in χ Cygni, which also showed significant linearly polarized flux. Upper limits (2σ) for v=2, J=2-1 emission in R Cas and VX Sgr are approximately 50 Jy. Emission was detected from each of these sources in v=1, J=2-1 during this period. Seven sources were observed in the v=1 and v=2, J=1-0 transitions. Five of these sources (Orion, VY CMa, R Leo, VX Sgr, and χ Cygni) were searched for emission from v=3, J=1-0, but none were detected (2σ upper limits of 50 Jy).

§2. Results and Discussion

A summary of selected parameters derived from the polarization measurements is given in Table III-2 for each source and each date of observation. Included are integrals over the velocity profiles for total flux density I, and measures of the profile-averaged fractional polarization

$$\langle m \rangle = \int P dv / \int I dv \ ,$$

and position angle

$$\langle \chi \rangle = 1/2 \ \tan^{-1}(\int U dv / \int Q dv) \ .$$

In this chapter $I \equiv S_T$, and $P \equiv S_P$. The large number of observations precludes the presentation of all the spectra from which Table III-2 is derived. Instead we present observations of representative sources showing high polarization (R Leo) and low polarization (Orion) in

Table III-2

SiO Maser Total Flux and Profile-Averaged Polarization Parameters (continued on next page).

SOURCE	DATE (1981)	TRANSITION	$\int Idv$ [a] ($10^{-20} Wm^{-2}$)	$\langle m \rangle \pm \sigma$ (%)		$\langle \chi \rangle \pm \sigma$ (°)	
IK Tau	5/22	v=1, J=2-1	414	16.1 ±	0.7	136 ±	2
	6/29	v=1, J=1-0	47	17.3	3.4	7	6
	6/30	v=2, J=1-0	46	20.9	2.2	79	4
Orion							
($-5 kms^{-1}$)	2/17	v=1, J=2-1	1072	4.8	0.6	92	4
($16 kms^{-1}$)			731	4.6	0.6	98	4
	3/17	v=1, J=2-1	940	4.0	0.7	79	5
			694	4.3	0.7	94	5
	4/22	v=1, J=2-1	1119	5.0	0.6	91	4
			827	5.7	0.7	96	4
	6/9	v=1, J=2-1	994	5.7	0.8	70	4
			847	6.1	0.8	76	4
	6/27	v=1, J=1-0	405	3.0	0.7	31	7
			181	4.6	0.8	135	5
	6/28	v=2, J=1-0	357	1.1	0.6	112	16
			130	2.8	1.0	110	10
VY CMa	2/17	v=1, J=2-1	1063	8.6	0.9	40	4
	6/27	v=1, J=1-0	844	3.8	0.7	136	6
	6/28	v=2, J=1-0	207	5.3	1.3	62	7
R Leo	5/21	v=1, J=2-1	426	29.6	0.8	38	2
	6/9	v=1, J=2-1	458	31.5	0.7	34	2
	6/28	v=1, J=1-0	64	13.3	2.0	128	5
	6/29	v=1, J=1-0	61	15.2	2.2	165	5

a. Values accurate to ~20%

Table III-2 (cont.)

SOURCE	DATE (1981)	TRANSITION	$\int Idv$ [a] ($10^{-20} Wm^{-2}$)	$\langle m \rangle \pm \sigma$ (%)		$\langle \chi \rangle \pm \sigma$ (°)	
W Hya	1/28	v=1, J=2-1	656	7.2	0.7	149	4
	5/22	v=1, J=2-1	765	14.3	0.8	38	3
	6/10	v=1, J=2-1	541	9.2	0.7	15	3
	6/27	v=1, J=1-0	270	11.2	0.8	24	3
	6/28	v=2, J=1-0	521	11.5	0.7	113	3
VX Sgr	1/31	v=1, J=2-1	804	6.6	0.8	94	4
	5/22	v=1, J=2-1	1187	4.3	0.6	151	4
	6/10	v=1, J=2-1	1256	4.7	0.6	158	4
	6/28	v=1, J=1-0	658	3.8	0.6	47	5
	6/29	v=2, J=1-0	679	3.5	0.7	27	6
χ Cyg	1/9	v=1, J=2-1	286	23.4	1.4	164	3
	2/16	v=1, J=2-1	395	23.9	0.7	158	2
	5/22	v=1, J=2-1	459	29.9	0.8	164	2
	6/10	v=1, J=2-1	638	32.1	0.8	161	2
	6/11	v=2, J=2-1	222	33.3	0.9	145	2
	6/28	v=1, J=1-0	68	30.5	1.9	169	3
	6/29	v=2, J=1-0	19	30.0	9.1	147	9
R Cas	2/16	v=1, J=2-1	50	35.5	4.0	37	4
	4/23	v=1, J=2-1	70	29.7	2.5	146	3

a. Values accurate to ~20%

Figures III-2 and 3. In Figure III-4 spectra of I, P, and χ are presented for four transitions in χ Cygni. Of special interest is the symmetry apparent in the polarization between the -5 km s^{-1} and +16 km s^{-1} components of Orion, and the rotation of position angle across the line profiles of both components. Although there was some variation in the position angles (15 to 20°) over the course of our observations, the general effect seen in Figure III-3 was apparent in most of our measurements. Based on this data, the Orion masers are modelled in the next chapter as arising in a rotating and expanding disk around the infrared source IRc2.

Our overall results confirm those of Troland et al. (1979, hereafter THJC) that the v=1, J=2-1 SiO masers can be highly polarized in some sources, while all sources for which sufficient sensitivity was obtained showed at least a few percent linear polarization. Similar polarization characteristics were found in the v=1, J=1-0 transitions, and there is a remarkable uniformity in profile-averaged fractional polarization, $\langle m \rangle$, between different transitions in individual sources. However, the average position angles, $\langle \chi \rangle$, show little correlation, as is discussed in more detail later.

Polarization and expansion velocity.

Figure III-5 is a plot of the maximum value of $\langle m \rangle$ for each source versus V_{exp}, the stellar expansion velocity (see Table III-1 for references; for Orion V_{exp} was taken to be half the separation between the OH peaks). What is notable in Figure III-5 is a tendency for sources with low V_{exp} to be strongly polarized, and those with high

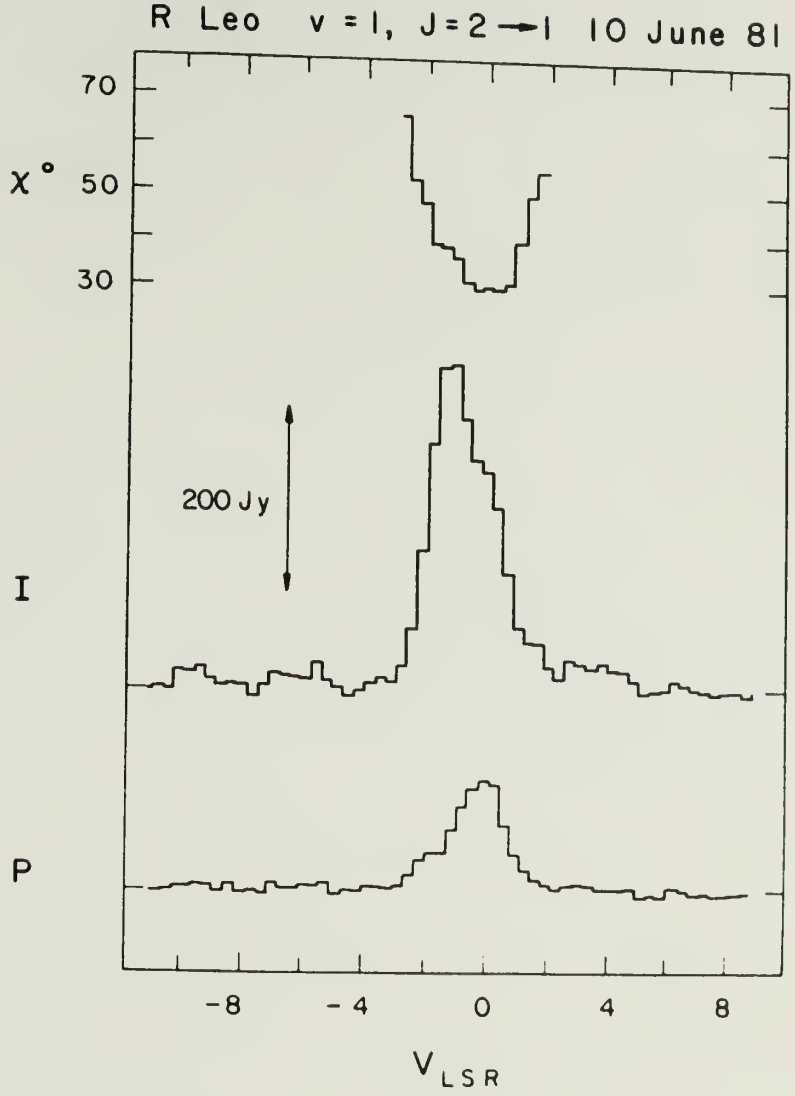

Fig.III-2. Profiles of P, I, and χ for R Leo. The fractional polarization is as high as 65% on the positive velocity side of the line.

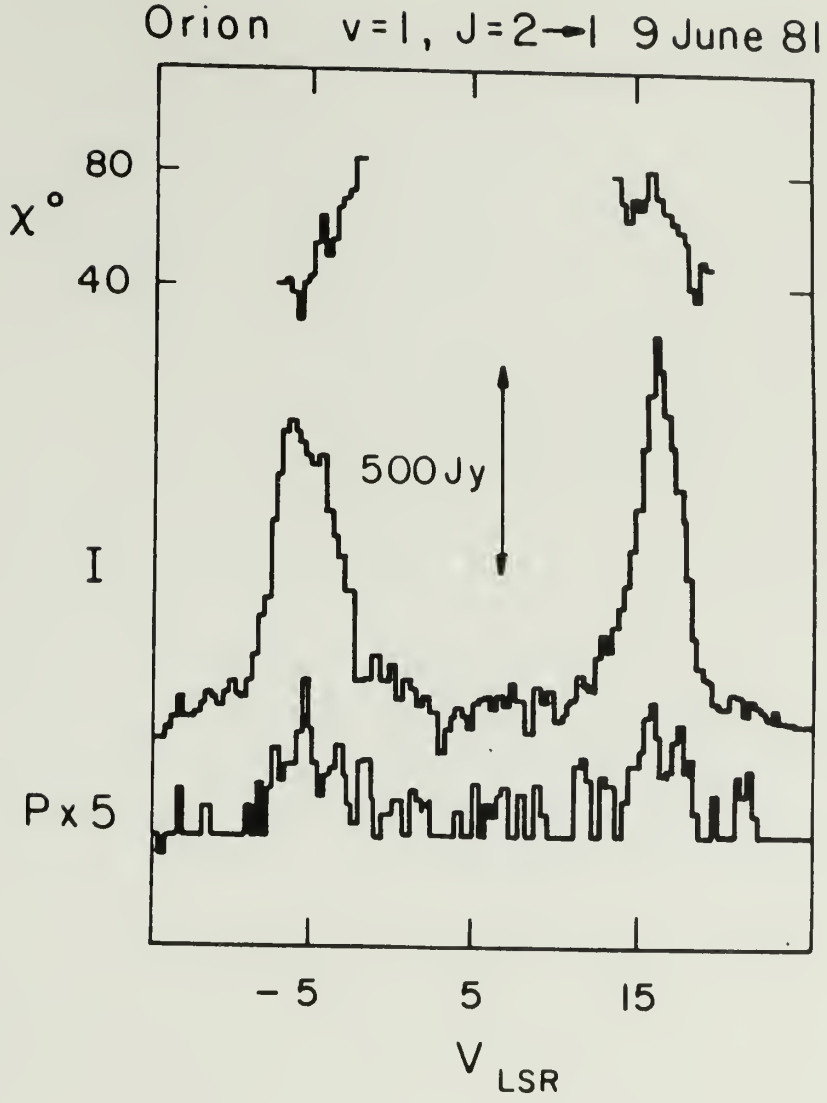

Fig.III-3. Profiles of P, I, and χ for Orion on 6/9/81. The polarized flux density is expanded by a factor of 5 relative to the total flux density scale. The fractional polarization is about 5% across the line profiles.

Fig.III-4. Comparison of total flux density and polarization for four SiO transitions in χ Cygni. The profile-averaged fractional polarizations and position angles are similar in all transitions.

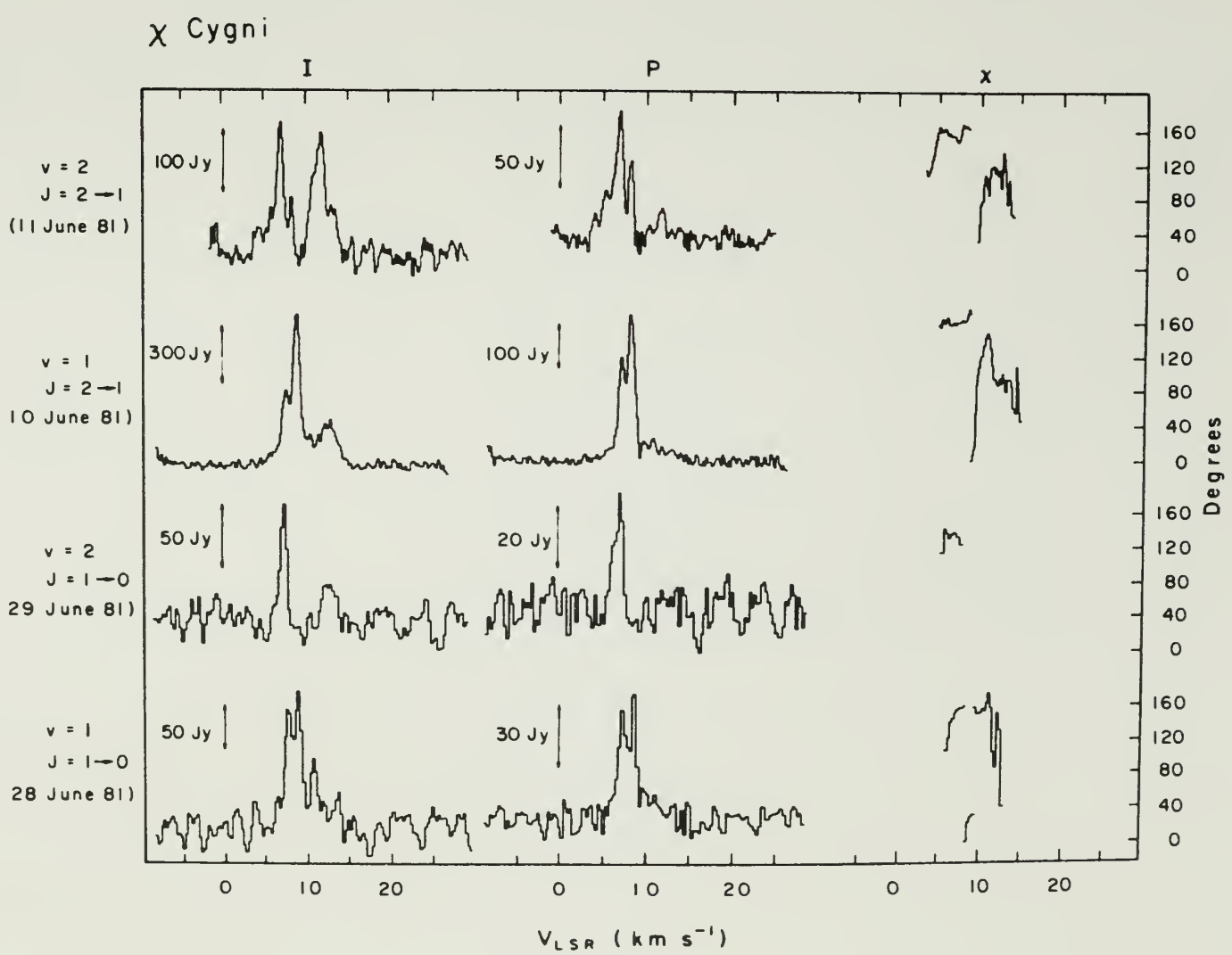
χ Cygni
I
P
X
v = 2
J = 2—1
(11 June 81)
100 Jy
50 Jy
v = 1
J = 2—1
10 June 81)
300 Jy
100 Jy
v = 2
J = 1—0
29 June 81)
50 Jy
20 Jy
v = 1
J = 1—0
28 June 81)
50 Jy
30 Jy
160
120
80
40
0
Degrees
0
10
20
V_{LSR} (km s^{-1})

V_{exp} to be weakly polarized. The data are consistent with an approximately hyperbolic relationship between $\langle m \rangle$ and V_{exp} such that

$$\langle m \rangle V_{exp} \cong 2.0 \ (\text{km s}^{-1}). \qquad \text{(III-1)}$$

We have roughly estimated the average polarizations, for essentially the same source sample, from I, Q, and U spectra presented by THJC, and find a qualitatively similar relationship between $\langle m \rangle$ and V_{exp}.

Interpretation of this result is difficult due to the lack of current knowledge of physical conditions in the regions where SiO masers arise. Goldreich, Keely, and Kwan (1973a, hereafter GKK) have formulated a theory of maser polarization which requires the presence of a magnetic field. They predict that the fractional polarization, as a function of the angle, θ, between field direction and maser gain path for saturated masers, will be given by (their case 2a)

$$m = \text{abs}\{(3\sin^2\theta - 2)/3\sin^2\theta\} \quad \text{for } \sin^2\theta \geq 1/3 \ , \qquad \text{(III-2)}$$

$$m = 1 \quad \text{for } \sin^2\theta \leq 1/3 \ .$$

This relation is plotted in Figure III-6, where it can be seen that the predicted polarization is much higher for $\theta \leq 45°$ than for $\theta \geq 45°$. It is tempting to suggest that a difference in $\langle m \rangle$ for different sources may be due to a different geometry between masers and fields, and that this geometry may be influenced by envelope expansion. For instance, in a slowly accelerated envelope (resulting in low V_{exp}), masers might be preferentially amplified along radial directions, because maximum gain paths are radial for $dv/dr < v/r$ and tangential for $dv/dr > v/r$. If the magnetic field were also radial, this would result in strongly

Fig.III-5. Plot of maximum observed value of profile-averaged fractional polarization, $\langle m \rangle$, versus envelope expansion velocity. Expansion velocities are from Table III-1, and values for $\langle m \rangle$ are from Table III-2.

Fig.III-6. Plot of m versus θ from Equation III-1 in text. The polarization position angle flips by 90° at $\theta \cong 55°$, where m goes to zero. This is discussed further in Chapter IV.

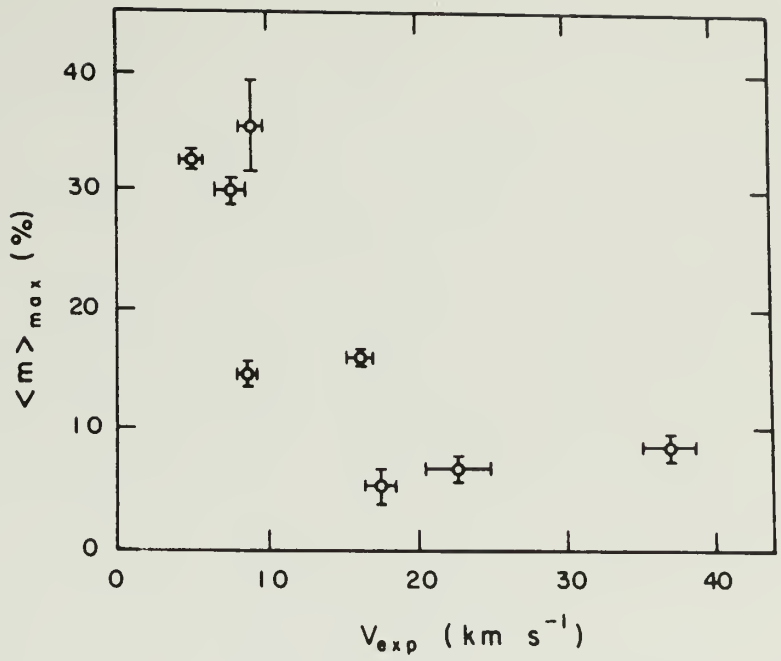
40
30
20
10
0
0
10
20
30
40
$\langle m \rangle_{max}$ (%)
V_{exp} (km s^{-1})

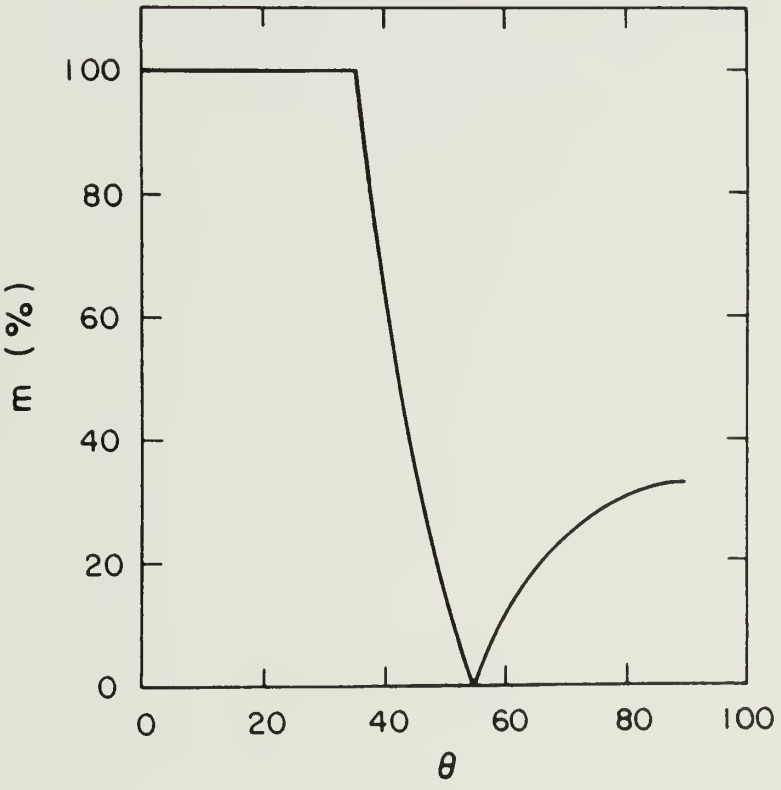
100
80
60
40
20
0
0
20
40
60
80
100
m (%)
θ

polarized masers since the angle θ in Equation III-2 would be small. In stars with high V_{exp} and rapid acceleration, the maximum gain paths would be tangential and the polarization weak. Other maser and field configurations might produce similar effects.

Alternatively, the strength of the polarization might be physically more related to other factors which are correlated with expansion velocity, such as stellar luminosity (Cahn and Wyatt 1978). Another possibility is that maser polarization may be influenced by conditions which differ with variable type. The stars with the most highly polarized masers (R Leo, R Cas, χ Cygni, and IK Tau) are all regular Mira variables, while of the four sources with lower polarization, two are semi-regular variables (W Hya and VX Sgr), one has no apparent period (VY CMa), and the fourth, Orion, is unique in many ways (see Genzel et al. 1980 and Elitzur 1982 for discussion), and is associated with the infrared source IRc2 (Wright and Plambeck 1983).

Comparision of polarization between transitions.

It has been argued that similarities in total flux density spectra between v=1 and v=2, J=1-0 indicate that masers in these two transitions arise in the same volume of gas (Schwartz et al. 1979; Spencer et al. 1981). Comparison of polarization provides another method of assessing the relative location of emission in different transitions, and we have examined the data in two somewhat different ways in order to address this question.

First, we have chosen well defined features (Table III-3) from the velocity profiles of v=1 and v=2 emission (for the same rotational

Table III-3

Total Flux Density and Polarization of
Individual SiO Maser Features
(continued on next page)

Source	J=1-0, v=1		J=1-0, v=2		J=2-1, v=1		J=2-1, v=2
	V	P, I [a] m(χ)					
IK Tau	30.0	17,170 10(110)	30.0	14,120 12(91)	33.2	18,260 7(60)	not observed
					35.3	66,275 24(140)	
					40.5	~0,85 ~0(-)	
Orion	-7.5	16,710 2(45)	-9.8	6,610 1(30)	-6.4	25,650 4(40)	
	-1.0	26,50 52(45)	-7.2	~0,350 ~0(-)	15.8	42,880 5(80)	not observed
	14.3	15,160 9(103)	18.2	~0,238 ~0(-)			
	16.7	0,310 0(-)					
VY CMa	11.4	24,780 3(100)	12.5	9,100 9(145)	not simultaneous		not observed
	14.7	~0,360 ~0(-)	20.7	11,350 3(70)			
	20.7	29,725 4(88)	22.1	17,330 5(100)			
	35.1	~0,138 ~0(-)	23.8	21,195 11(70)			
			31.0	~0,80 ~0(-)			

a. Velocity is in km s^{-1}, P and I are in Janskys, and χ is in degrees.

Table III-3 (cont.)

Source	J=1-0, v=1 V	J=1-0, v=1 P, I[a] m(χ)	J=1-0, v=2 V	J=1-0, v=2 P, I[a] m(χ)	J=2-1, v=1 V	J=2-1, v=1 P, I[a] m(χ)	J=2-1, v=2 V	J=2-1, v=2 P, I[a] m(χ)
R Leo		b		b	-1.0	115,625 18(35)		not observed
W Hya	37.0	28,250 11(50)	36.9	45,800 6(105)	37.0	9,250 4(60)		
	39.0	46,300 15(50)	41.0	105,700 15(115)	39.5	35,400 9(30)		not observed
	40.5	15,505 3(110)	43.4	90,400 23(100)				
	43.0	45,200 23(0)						
VX Sgr	3.0	17,600 3(40)	3.3	23,580 4(35)	-2.0	12,210 6(15)		
	4.0	22,550 4(155)	4.3	18,530 3(160)	1.0	~0,310 ~0(-)		
	8.5	22,660 3(40)	8.8	34,600 5(40)	3.0	33,365 9(0)		not detected
	12.9	14,250 6(100)	12.4	5,365 1(140)	4.0	31,391 8(175)		
					8.5	22,240 9(160)		
					10.4	5,165 3(96)		
χ Cyg	7.5	42,135 31(155)	7.3	34,98 35(140)	7.3	243,400 61(160)	7.1	107,205 52(152)
	8.8	59,158 37(32)	13.0	4,35 11(20)	8.7	345,800 43(175)	8.3	67,100 67(167)
					12.4	33,220 15(95)	11.9	26,190 14(110)

a. Velocity is in km s^{-1}, P and I are in Janskys, and χ is in degrees.
b. Data too noisy to discern individual features.

transition), and compared them for velocity coincidence and similarity of polarization. The features in these complex spectra are almost never isolated from other features and underlying "pedestal" emission. This will inevitably result in contamination of the polarization of individual features. It is difficult to evalute the magnitude of this effect, but we estimate, judging from blending of total flux density profiles, that the polarizations will be reduced by at least 10-20% by a confusing component in most sources. We therefore used the following somewhat conservative criteria in comparing features: individual features were deemed "coincident" if they peaked within 0.5 km s^{-1} of each other in velocity, and polarizations were considered "similar" if $m_1 \pm 0.1m_1$ overlapped $m_2 \pm 0.1m_2$ and if χ_1 and χ_2 were within 20° of each other. Here m_1, m_2, χ_1, and χ_2 are the fractional polarizations and position angles for velocity coincident features in v=1 and v=2.

A comparison of v=1 and v=2 spectra for seven sources in J=1-0, and including the J=2-1 transitions of χ Cygni, yielded a total of 43 features, in which 14 pairs of velocity coincident features were found (or, stated somewhat differently, 65% of all features are paired in velocity). Of these 14 pairs, 8 pairs were found to be similarly polarized. Comparing different rotational transitions (J=1-0 versus J=2-1) for the same vibrational state resulted in a total of 37 features, but with only 8 velocity pairs (45% of features paired), with no pair showing similar polarization.

Before concluding that these velocity and polarization pairings indicate a physical association of the emitting regions, it should be

shown that they are unlikely to have come about by chance. Adding together all the velocity intervals examined for all sources in the comparison of v=1 and v=2 spectra, we have found 43 features over about 100 km s^{-1}. To obtain an estimate of how many velocity pairs would occur by chance, we have considered these features to be delta functions and asked how many would be expected to coincide to within 0.5 km s^{-1} of each other if half were randomly distributed in v=1 and the other half in v=2. A random, unweighted distribution of features in velocity space was chosen for this analysis, since an examination of the features that we used did not show a strong tendency toward clustering about the centers of the line profiles. In this hypothetical case, 5 ± 2 chance velocity pairs are expected between vibrational states and in the actual comparison 14 pairs were obtained. In the comparison of rotational transitions, we expect 4 ± 2 chance velocity pairs and obtain 8.

We can also estimate the expected number of similarly polarized pairs (using the criteria above), assuming that the features are randomly polarized. If m_1 and m_2 are allowed to lie between 0.0 and 1.0, then the probability that $m_2 \pm 0.1m_2$ overlaps $m_1 \pm 0.1m_1$ is $P_m = 0.4m_1$ for $0.0 \leq m_1 < 0.82$, and $P_m = 1.0 - 0.82m_1$ for $0.82 \leq m_1 \leq 1.0$. Averaging over the full range of m_1, the mean probability of overlap for random m_1 and m_2 is $\langle P_m \rangle = 0.18$. The probability of obtaining two random position angles within 20 degrees of each other is $P_\chi = 40/180 = 0.22$. Combining these probabilities we expect only 0.6 out of 14 velocity pairs to be similarly polarized in both m and χ by chance, and since 8 such pairs were found this can be taken as

additional evidence that v=1 and v=2 emission (for the same rotational transition) tends to arise in the same volume of gas. On the other hand, out of 8 velocity pairs found between J=1-0 and J=2-1 for v=1, none were similarly polarized, indicating either that the polarization mechanism behaves differently for different rotational transitions, or that different rotational transitions arise in different regions. The latter has also been suggested by Lane (1982) based upon comparison of total intensity profiles. Current maser models are unable to account for the coincidence of emission in different vibrational states (see Lane 1982 for discussion).

Turning briefly to individual sources, a striking example of correspondence of both velocity profiles and polarizations between v=1 and v=2 is the supergiant star VX Sgr. In Figure III-7 the profiles of v=1 and v=2, J=1-0 are almost identical. Also, the three strongest features (at 3.0, 4.0, and 8.5 km s^{-1}) are remarkably similar in I, m, and χ (see Table III-3). It would be difficult to explain how these masers could correspond so closely in velocity, total flux density, and polarization unless they are spatially coincident. Included in Figure III-7 is the v=1, J=2-1 spectrum, which looks quite different from those of J=1-0. Some features do coincide in velocity, but the polarizations are dissimilar.

Three of the eight sources examined (R Leo, Orion, and W Hya) showed no distinct features with the same velocity and polarization in v=1 and v=2. χ Cygni, the only source which was detected in four transitions, had similar velocity profiles and similar polarizations in v=1 and v=2, J=2-1, but the v=1 and v=2, J=1-0 profiles differed con-

siderably (Figure III-4).

The second approach taken in comparing the polarization in different transitions involves the quantities $\langle m \rangle$ and $\langle \chi \rangle$, which are derived from the integrals over the full velocity profiles of I, P, Q, and U. These were chosen in order to investigate the more general polarization properties of the total maser emission in each transition.

A remarkable similarity in $\langle m \rangle$ between transitions emerges for all transitions measured in a given source, although this quantity is different from source to source. This is displayed in Figures III-8a and 8b where $\langle m \rangle$ (v=1,J=1-0) versus $\langle m \rangle$ (v=2,J=1-0) and $\langle m \rangle$ (v=1,J=2-1) versus $\langle m \rangle$ (v=1,J=1-0) are plotted (using values from Table III-2). The only source which did not have similar fractional polarizations in all transitions was R Leo. In this source, the v=1, J=2-1 polarization was different from those of v=1 and 2, J=1-0 (Figure 8b). However, those observations were not strictly simultaneous, having been taken about two weeks apart. Perhaps significantly, R Leo was near optical maximum during this interval, and the polarization may have changed. Clarke, Waak, and Bologna (1982) monitored the total flux density from R Leo in v=1, J=1-0 during this period, and found rapid and substantial changes in profile width and intensity. The two transitions in R Leo that were measured within one day of each other (v=1 and 2, J=1-0) do show the same equality of $\langle m \rangle$ evident in the other sources.

A comparison of the profile-averaged position angle $\langle \chi \rangle$ between transitions (Figures III-8c and 8d) does not show the same correlation as was found for $\langle m \rangle$ (except in χ Cygni, which has similar $\langle m \rangle$ and $\langle \chi \rangle$ for all four transitions). The near equality of $\langle m \rangle$ in all transitions

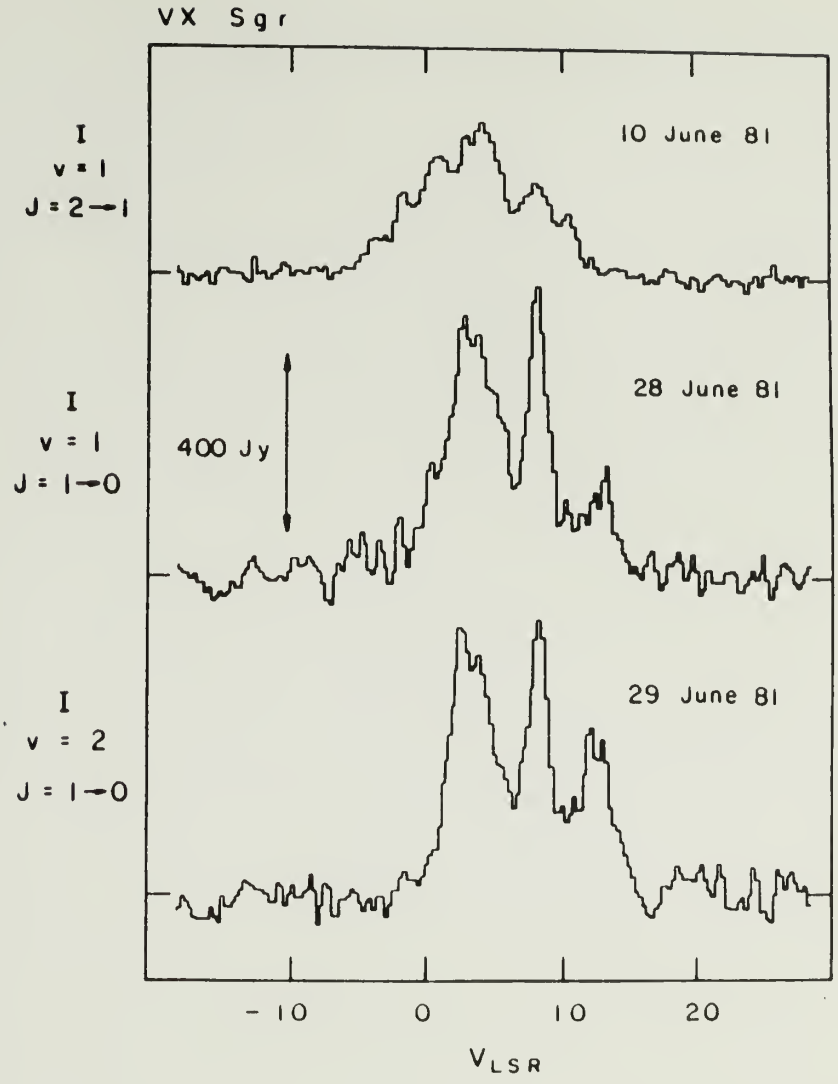

Fig.III-7. Comparison of total flux density spectra in three transitions (v=1 and v=2, J=1-0, and v=1, J=2-1) for VX Sgr. Note that the profiles of v=1 and v=2, J=1-0 are almost identical to each other, but that the v=1, J=2-1 profile is considerably different. The fractional polarizations and position angles of components at 3.0, 4.0, and 8.5 km s^{-1} are also very similar between the J=1-0 transitions (see Table III-3).

Fig.III-8a and b. (facing page) Comparison of $\langle m \rangle$ between different transitions. The solid line has slope one. In fig.III-8b, the only source which does not fall near the line is R Leo. However, the data were not strictly simultaneous and the polarization may have changed during the time interval between the J=2-1 and J=1-0 observations. See text for discussion.

Fig.III-8c and d. (second page) Comparison of $\langle \chi \rangle$ between different transitions. The solid line has slope one. Note lack of correlation in position angle between transitions, in comparison with the strong correlation of fractional polarization.

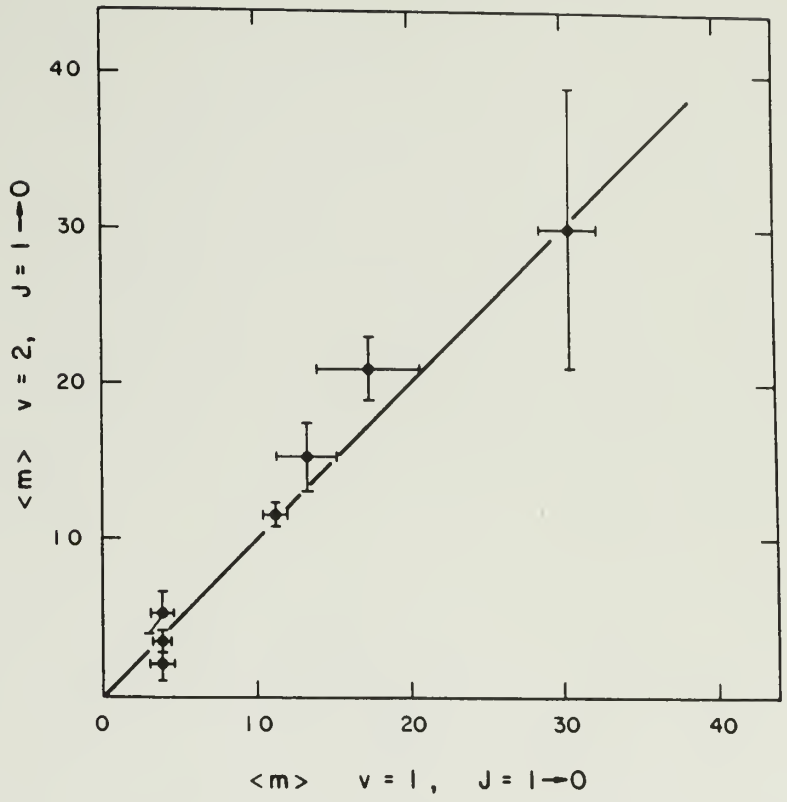
40
30
20
10
0
10
20
30
40
<m> v = 2, J = 1→0
<m> v = 1, J = 1→0

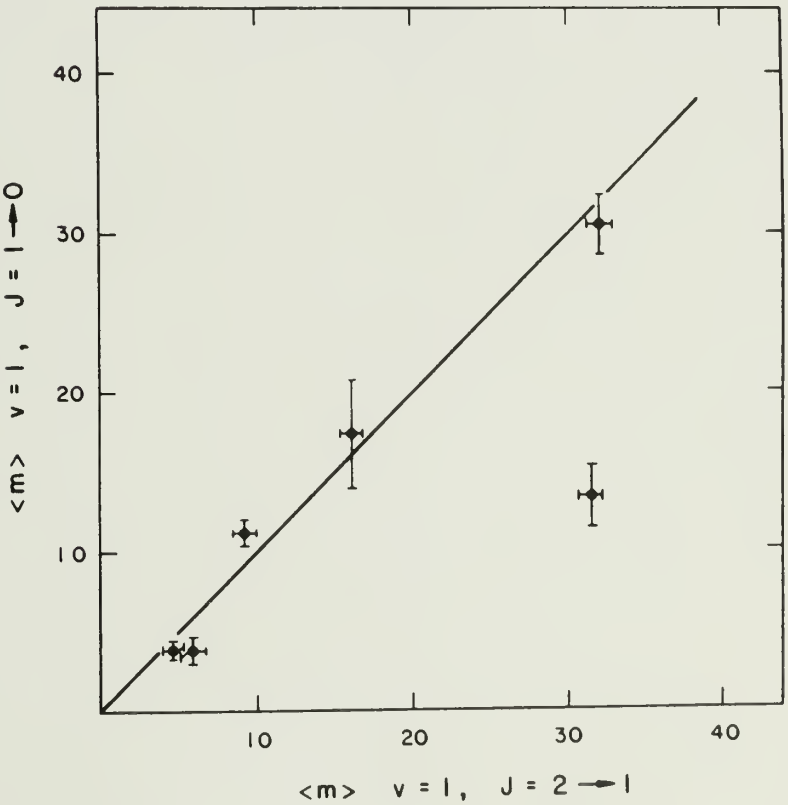
40
30
20
10
10
20
30
40
<m> v = 1, J = 1→0
<m> v = 1, J = 2→1

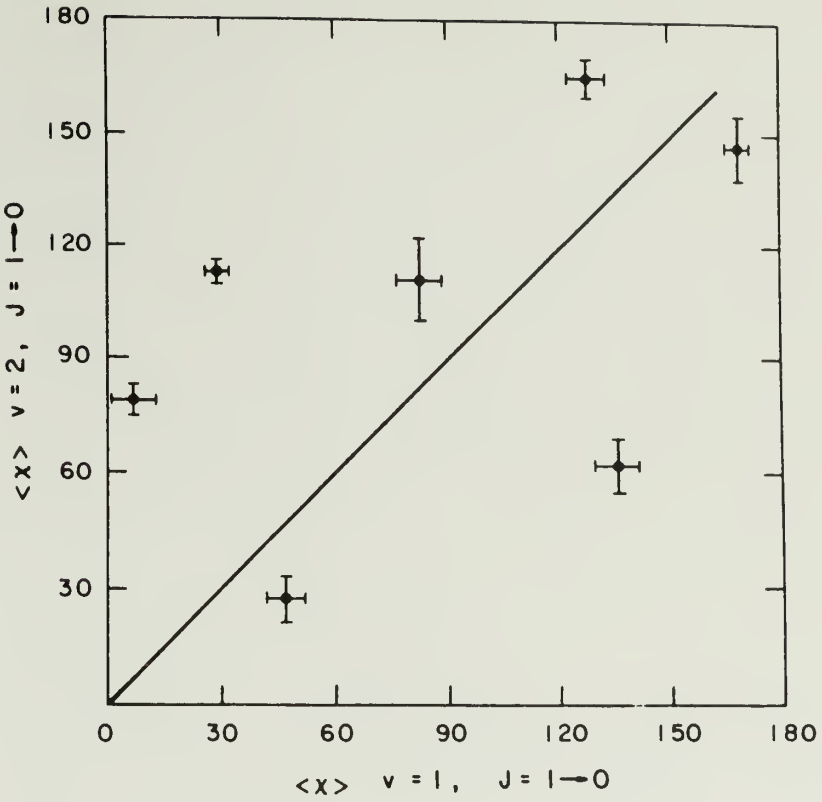
180
150
120
90
60
30
0
30
60
90
120
150
180
<χ> v = 2, J = 1→0
<χ> v = 1, J = 1→0

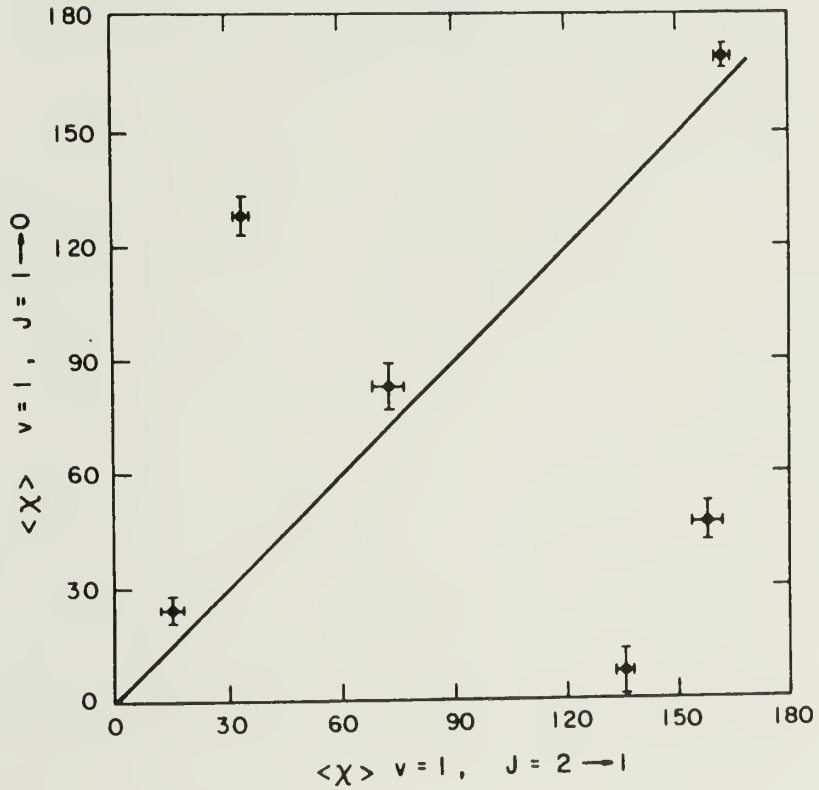
180
150
120
90
60
30
0
30
60
90
120
150
180
<χ> v = 1, J = 1→0
<χ> v = 1, J = 2→1

cannot be readily explained by invoking spatial coincidence of a majority of features since the profile-averaged position angles are generally different. Futhermore, we have already shown that although a significant number of features in v=1 and v=2 for the same rotational transition have similarly polarized counterparts, this number is less than half of all features identified. The correlation of $\langle m \rangle$ between J=1-0 and J=2-1 is surprising, since in that case no similarly polarized pairs of features were found between the two transitions in any source.

In Figure III-6 it can be seen that for some values of m (near m=30% and m=100%) the GKK theory predicts that m will change relatively little or not at all over a wide range in θ. From this it might be expected that $\langle m \rangle$ would show a higher degree of correlation between transitions than would $\langle \chi \rangle$, if we assume that the gain paths are oriented randomly with respect to magnetic field. We have estimated for each source the probability that the values of $\langle m \rangle$ will lie within the observed range, for random θ in the different transitions, and find in all cases that this probability is less than 0.10. This is a simplification since we have not taken into account the fact that $\langle m \rangle$ results from a number of individual masers in each transition, and that factors such as cross-relaxation (see §2 of Chapter IV) can alter the polarization. However, the uniformity in $\langle m \rangle$ is unlikely to occur for random orientations.

The equivalence of $\langle m \rangle$ between transitions might be easier to understand if the orientations are not random, and masers in all transitions tend to be amplified at some preferred angle to the magnetic

field, a possibility that was suggested earlier. Alternatively, SiO masers may be polarized by some mechanism other than that proposed by GKK. Western and Watson (1983a, b, and c) have proposed a polarization mechanism based on geometry and anisotropic pumping rather than magnetic fields. Bajarrabal and Nguyen-Q-Rieu (1981) have also discussed a polarization mechanism, but have not made quantitative estimates of the fractional polarization expected from their model.

In summary, even in sources where most of the velocity features do not have the same polarization in different transitions, the profile-averaged fractional polarizations are nevertheless generally the same, while the profile-averaged position angles are generally different. Sources which were found to have high or low polarization in the present work show similar characteristics in the spectra presented by THJC, even though considerable variation had occured in other properties of the maser radiation (profile shapes, intensities, etc.). These points suggest that the global properties which determine the average fractional polarization of the ensemble of maser spots around each star affect all transitions in the same way, and that these properties are relatively stable with time. Furthermore, the polarization properties might be influenced by stellar envelope expansion velocity, stellar luminousity, or some other related stellar property.

Time variability.

Six of the eight sources were observed more than once in v=1, J=2-1, and it is evident from Table III-2 that the profile-averaged polarizations varied considerably for some sources over the course of

this program. Examination of the data reveals no general trends in the variability characteristics from source to source. It appears that position angle can change considerably with only small variations in total or polarized flux, as in R Cas, or the position angle may remain constant while the total and polarized fluxes change substantially, as occured for χ Cygni. The increase in fractional polarization with increasing total flux for χ Cygni may mean that the cross-relaxation rate is comparable to the stimulated emission rate in this source (Goldriech, Keely, and Kwan 1973b). This effect has been seen in the linear polarization behavior of the H_2O masers in W75 S (Bologna et al. 1975). Variations in W Hya and VX Sgr showed no systematic relationship between total flux, fractional polarization, and position angle.

§3. Summary

We have reported the results of a program to monitor linear polarization of SiO masers in the v=1, J=2-1 transition in late-type stars and in Orion, and have presented near-simultaneous polarization measurements in several SiO maser transitions. The main findings of this work are :

1. Linear polarization was detected in every source observed. Profile averaged fractional polarizations ranged from ~ 3 - 37% , and individual maser features ranged in fractional polarization from ~ 0 - 67%.
2. Time variations in linear polarization were detected in some

sources, but these variations could not in general be related in any simple way to changes in total flux.

3. An inverse correlation was found between fractional polarization of the SiO maser lines and stellar expansion velocity. It is suggested that this may be a result of magnetic field geometry, variable type, or some stellar property related to expansion velocity such as stellar luminosity.
4. Comparison of velocity and polarization pairings of features in different SiO transitions indicate that emission from different vibrational states is spatially coincident, at least for some sources. The comparison of different rotational transitions shows significantly fewer pairings of features, indicating that masers of different rotational transitions do not arise in the same volume of gas.
5. The profile-averaged fractional polarizations show a uniformity between different transitions for a given source, even when individual velocity matched features are not similarly polarized. The profile-averaged position angles do not in general appear to be correlated between transitions.

CHAPTER IV

A MODEL FOR THE SiO MASERS IN ORION

§1. Introduction

Since their discovery as the first known sources of SiO maser emission by Snyder and Buhl (1974), the SiO masers in Orion have continued to attract considerable attention due to the apparently unique circumstances of their origin and their spectral and temporal properties. While all other known SiO maser sources exist in the vicinity of late-type Mira or supergiant stars, the Orion masers are associated with the intense infrared source IRc2 (Baud et al. 1980) located in the Orion KL Nebula and now thought to be powered by a young O or B star (Downes et al. 1981). The Orion maser spectrum in the v=1, J=2-1 transition shows a double-peaked profile which has been relatively constant in both intensity and shape over the past eight years, unlike the masers from late-type stars, which have irregular profiles that can change markedly on time scales of one year or less.

Using VLB interferometry, Lane (1982) found that the two components in SiO v=1, J=1-0 are spatially separated by 10^{15} cm (0".14). Wright and Plambeck (1983) measured a similar separation in v=1, J=2-1, at position angle -45°, and also determined that the masers lie within the error bars of the best infrared position for IRc2. Although little is known about the distribution of matter in the region where the masers are formed, on larger scales ($\sim 10^{17}$ cm) IRc2 is surrounded by a thick

disk of material observed in SO by Plambeck et al. (1982), and it is also thought to be the source of the high velocity bipolar flow seen in Orion (Wright et al. 1983). The disk is expanding with a projected velocity of about 18 km s^{-1}, as evidenced by SO line shifts and the velocities of H_2O masers embedded in the disk.

Linear polarization in the v=1, J=2-1 transition in Orion was first measured by Troland et al. (1979), who found weak polarization which they attributed to instrumental effects. Measurements reported in Chapter III demonstrate that the Orion masers were approximately 5% linearly polarized between January and June 1981. Furthermore, the fractional polarization was constant across the line profiles of both the -5 and +16 kms^{-1} components, and approximately equal in both components. Perhaps the most interesting aspect of these data is in the behavior of the polarization position angles, which rotate across the line profiles of both components in a highly symmetric fashion (see Figure IV-1a). The total rotation is about 60°, and the rate of change of position angle with velocity is about the same for the two components.

It is often stated in the literature that much can be learned from the study of SiO masers concerning physical conditions in the regions where they are formed, but only rarely do the masers themselves cooperate by exhibiting simple behavior which is open to ready interpretation. The unique symmetry displayed by the Orion masers in both total intensity and polarization must surely contain a message regarding the circumstances of their origin. The similar widths and intensities of the two components, and their spatial and velocity

Fig.IV-1a. (left) The measured polarized flux density (P), total flux density (I), and polarization position angle (χ) spectra for the Orion SiO masers. Note similar line profiles in both total and polarized intensity for the -5 and +16 kms^{-1} components, and symmetric rotation of position angles across the profiles. The polarized flux density has been expanded by a factor of five relative to the total flux density scale.

Fig.IV-1b. (right) Numerical results of model for the Orion SiO masers. The quantities plotted are the same as in Fig.IV-1a. The model assumes a magnetic field which is parallel to the velocity vector at each point. For model parameters see text.

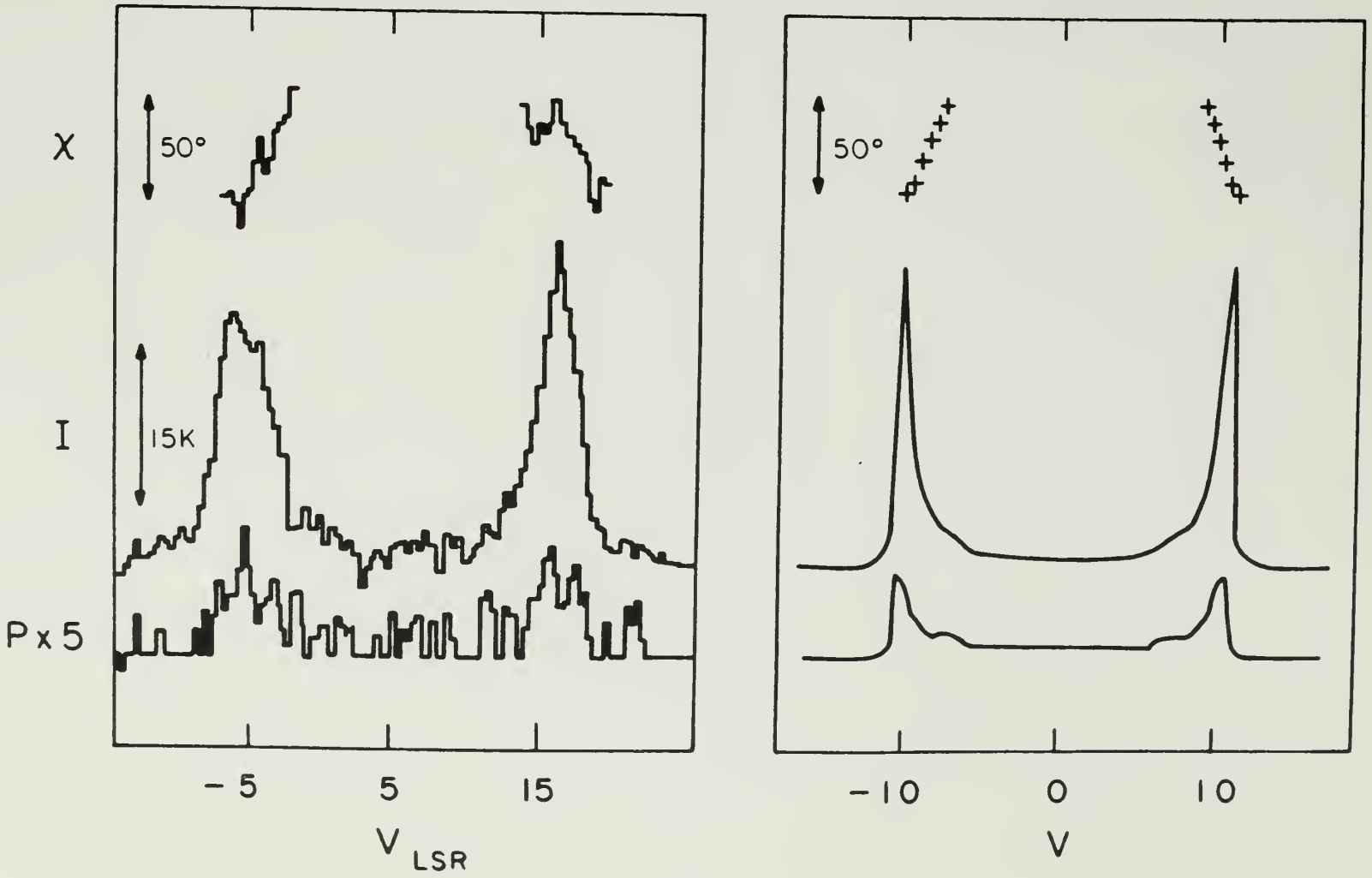
χ
50°
I
15K
P x 5
-5
5
15
V LSR
50°
-10
0
10
V

separations, indicate that the masers arise in a region of highly organized motion, and that physical conditions related to maser amplification must be quite uniform at the distances from the central source at which the masers are produced. Similar inferences based upon the maser polarization can be made once the polarization mechanism is specified. A detailed theory has been worked out by Goldreich, Keely, and Kwan (1973), in which maser polarization can be generated by the presence of a magnetic field in the masering gas. A model to explain the pumping and luminosity of the Orion masers has been presented by Elitzur (1982).

In this chapter we present a model to explain the velocity profiles of the total intensity and polarization of the Orion SiO masers, and show that the data are consistent with maser emission from a rotating and expanding (or contracting) disk with a magnetic field.

§2. The Model

The model assumes a disk with radial and azimuthal flows, and the treatment herein will concentrate on the kinematic effects of expansion and rotation on maser emission. It should be noted that the results of the model do not distinguish between expansion and contraction; henceforth only expansion will be discussed.

Geometry and kinematics.

The velocity laws have been taken for simplicity to be of the form $v_r = v_{r0}(\rho)^{\varepsilon}$ and $v_t = v_{t0}(\rho)^{\beta}$, where v_r and v_t are the radial and tangential velocities at radius r from the central star, v_{r0} and v_{t0}

are the initial velocities at $r = r_0$, and $\rho = r/r_0$. It has been assumed that all quantities are independent of height z in the disk. In order to further simplify the model and emphasize the kinematic effects, the pump rate has been taken to be constant with radius, and the maser emission has been assumed to be saturated. The gas density has been assumed to fall off as 1/r, although the specific density law chosen has little bearing on the overall results.

In general, the disk will be inclined at some angle i to the line of sight; the disk geometry and coordinate systems adopted are shown in Figure IV-2. The unprimed axes are those appropriate to describing quantities in the plane of the disk, while the primed coordinates are obtained from a rotation by i about the y-axis, and are more appropriate to the observer's view of the system. The x' axis is the observer's line of sight, and the y'- z' plane is the plane of the sky. The velocity at a point (x,y) in the disk is given by

$$\underline{v} = v_x \underline{x} + v_y \underline{y} \qquad \text{(IV-1)}$$

$$= (v_r x/r + v_t y/r)\underline{x} + (v_r y/r - v_t x/r)\underline{y}$$

The line-of-sight velocity along x' is $v_D = -v_x \cos(i)$.

The coherent gain path over which a maser can operate is limited to the length L (necessarily along x') over which the change in v_D is about equal to the thermal width Δv_{therm}. This is given approximately by

$$L = \Delta v_{therm} (\partial v_D / \partial x')^{-1}. \qquad \text{(IV-2)}$$

The relative maser gain at any point in the disk will be taken to be

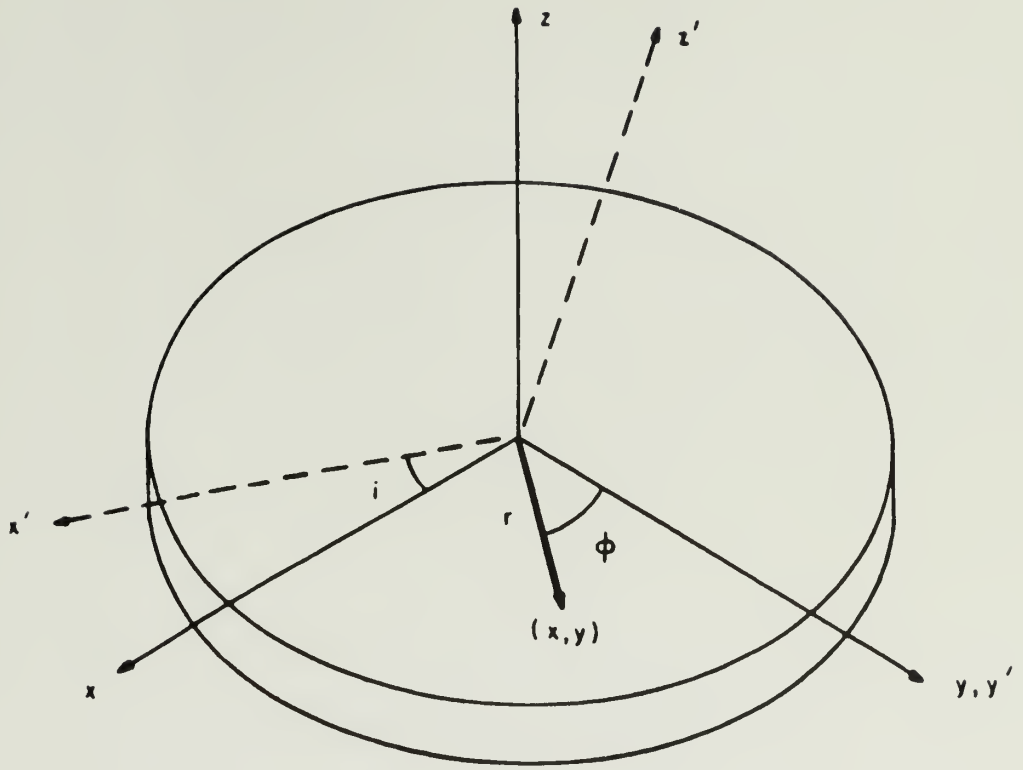

Fig.IV-2. Disk geometry and coordinate systems described in the text. Unprimed coordinates are appropriate for describing quantities measured in the plane of the disk, and primed coordinates are obtained by a rotation by angle i about the y axis.

proportional to L at that point, and inversely proportional to r (because of the falloff in density). The line-of-sight velocity gradient used in the calculation of L is

$$\begin{aligned} \partial v_D/\partial x' &= \cos(i)\partial v_x/\partial x \\ &= \cos(i)\{v_r r^{-1} - (1-\varepsilon)v_r x^2 r^{-3} - (1-\beta)v_t xy r^{-3}\}. \end{aligned} \qquad \text{(IV-3)}$$

If at some point in the disk the velocity gradients become too small, the gain length may be limited by the total thickness z_1 of the disk, in which case

$$L = z_1 \,/\, \sin(i). \qquad \text{(IV-4)}$$

Polarization.

The polarization of the maser radiation will be calculated using the maser polarization theory of Goldreich, Keely, and Kwan (1973). Briefly, in order to produce linear polarization, they require that :

1. The masers are saturated ($R > \Gamma$, where R is the stimulated emission rate, and Γ is the spontaneous decay rate out of the upper maser level).
2. A magnetic field is present of sufficient strength that the Zeeman splitting is greater than $(R\Gamma)^{1/2}$. Troland et al. (1979) calculated a lower limit of $B > 400$ μG in order that this condition be satisfied for SiO masers.
3. The stimulated emission rate must be greater than the rate of "cross-relaxation," a process which reduces population differences between magnetic sublevels in the upper maser state.

The fractional maser polarization, m, predicted by that theory is a function of the angle θ between the magnetic field direction and the maser gain direction, and is given by

$$m = \mathrm{abs}\{(3\sin^2\theta - 2) / 3\sin^2\theta\} \qquad \text{for } \sin^2\theta > 1/3 , \qquad \text{(IV-5)}$$

$$m = 1 \qquad \text{for } \sin^2\theta < 1/3 .$$

The position angle χ of the electric vector of the polarized emission is parallel to the projection of $\underline{B}$ on the sky for $\theta < 55°$, and is perpendicular to the projection of $\underline{B}$ for $\theta > 55°$ (at $\theta = 55°$, $m = 0$).

Since polarization position angle is defined by the magnetic field direction, a field which is constant in direction across the disk cannot produce rotation of position angle (assuming that Faraday effects are unimportant in the masering regions). Therefore, in order to reproduce the observed position angle behavior it is necessary to invoke a field which changes in direction across the regions of maser emission. The following simple magnetic field geometries satisfy this condition in that their directions rotate with azimuthal angle φ around the disk:

1. A field which is parallel to the velocity vector at every point. (This situation could be obtained if a weak field was frozen into the moving medium and dragged out by mass motions.)
2. A purely radial field.
3. A purely tangential field.

For the purpose of illustration, the maser polarization will be calculated for field configuration 1 above. In this case, since $\underline{B}$ is parallel to $\underline{v}$, the position angle is defined at each point by the

projection of $\underline{v}$ onto the plane of the sky (the y'- z' plane). In the observer's coordinates, the projection of $\underline{v}$ onto the sky is

$$\underline{v}'_{sky} = v_y \underline{y}' - v_x \sin(i) \underline{z}' \qquad \text{(IV-6)}$$

Position angle on the sky is conventionally measured from north toward east, and if we take the z' axis as north, then east would be in the direction of the -y' axis. The position angle, χ_v, of $\underline{v}'_{sky}$ at position (x,y) in the disk is then given by

$$\begin{aligned} \tan\chi_v &= \big(1/\sin(i)\big) v_y/v_x \qquad \text{(IV-7)} \\ &= \big(1/\sin(i)\big)\{(v_r y - v_t x)/(v_r x + v_t y)\} \ . \end{aligned}$$

The polarization position angle of the maser radiation (χ) will either be equal to χ_v (if $\theta < 55°$) or $\chi_v + 90°$ (if $\theta > 55°$). The angle θ between the field direction (parallel to $\underline{v}'$) and maser gain direction, is found from

$$\begin{aligned} \cos\theta &= \underline{v}' \cdot \underline{x}' \ / \ |\, v' \,| \\ &= \cos(i)\ (v_t y/r + v_r x/r) \ / \ (v_r^2 + v_t^2)^{1/2} \ . \qquad \text{(IV-8)} \end{aligned}$$

This angle also determines the fractional polarization of the maser, given by Equation IV-5.

The resultant polarization from a disk is computed numerically by first forming the run of Stokes parameters versus position (x,y) in the disk, using the relations

$$Q(x,y) = \big(L(x,y)/r\big) m(x,y) \cos 2\chi(x,y) \ , \qquad \text{(IV-9)}$$

$$U(x,y) = \big(L(x,y)/r\big) m(x,y) \sin 2\chi(x,y) \ . \qquad \text{(IV-10)}$$

At each point, the line-of-sight velocity v_D is calculated, and velocity channels are constructed with width approximately 0.5 kms^{-1}. All values of Q(x,y) and U(x,y) with velocities appropriate to a given channel are summed separately to yield a net $Q(v_D)$ and $U(v_D)$ for that channel. Finally, the polarized intensity (in relative units) and position angle as a function of velocity are calculated from the Stokes parameters. The relative total intensity is calculated in a similar way.

§3. Results and Discussion

In order to calculate the total intensity and polarization spectra from the model, a number of parameters must be specified. These include the velocity exponents β and ε, the initial velocities v_{0t} and v_{0r}, the inclination angle i, the thickness and radial extent of the disk, and the magnetic field geometry. The numerical results indicate that significant polarization position angle rotation across the line profiles will occur only if the radial and tangential velocities are of the same order throughout much of the disk. Pure expansion or pure rotation in the disk will produce flat position angle profiles.

Rotation of position angle occurs because emission at different velocities originates at different positions in the disk, and since the magnetic field direction changes with position, a variation of position angle with velocity results. This effect is illustrated in Figure IV-3, where the location of emission in the disk is plotted for several different velocities. Though emission in a given velocity channel arises over an extended region, for clarity it has been represented by a

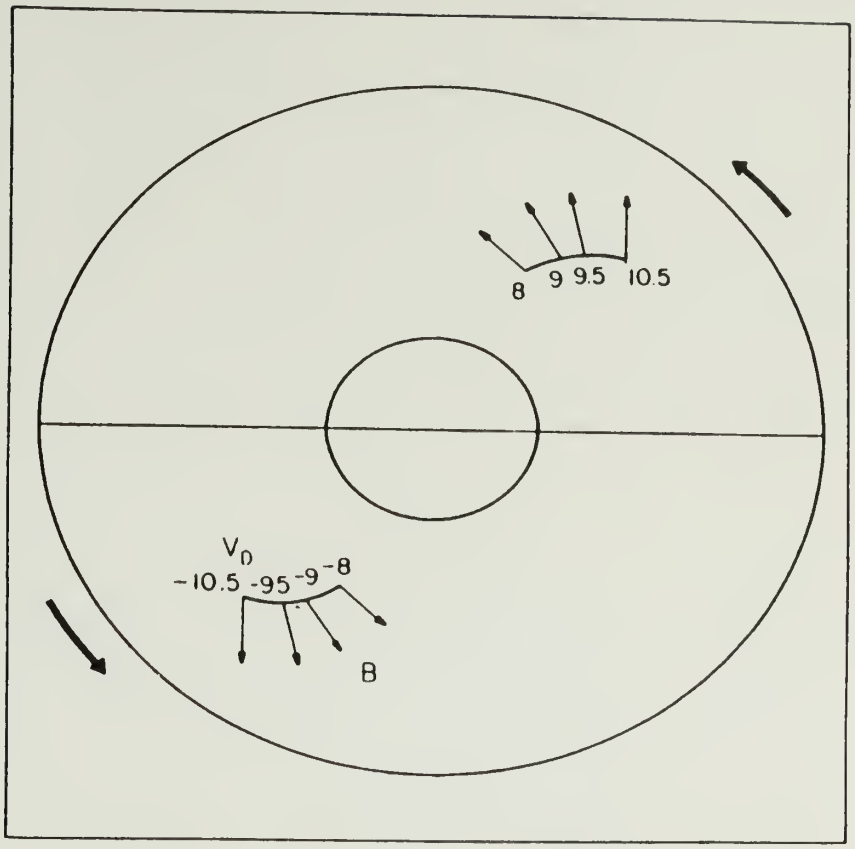

Fig.IV-3. Illustration of the change in position of the integrated emission from the disk for different line-of-sight velocities (V_D). Also shown is the direction of the magnetic field as a function of velocity and position for the model in which $\underline{B}$ is parallel to $\underline{v}$. For the model parameters given in the text (those used to generate Fig.IV-1b), the electric field of the maser polarization is perpendicular to $\underline{B}$.

single point in Figure IV-3, the intensity weighted centroid of the emission. Also plotted in Figure IV-3 is the magnetic field direction for several velocity channels. It can be seen that the direction rotates with velocity.

The observed velocity separation of the two peaks, plus the condition that both rotation and expansion must be present, have been used to set the initial velocities and the range of radial integration for a given ε and β. Specifically, the radial extent of the masing region has been chosen to lie approximately between $0.4r_{eq}$ and $1.5r_{eq}$, where r_{eq} is the radius at which $v_t = v_r$.

A plot of the numerical results is presented in Figure IV-1b for a model which represents the general features of the observed total flux and polarization spectra of the Orion SiO masers. For this model, $\underline{B}$ is parallel to $\underline{v}$, $\varepsilon = 0.5$, $\beta = -0.5$, $i = 57°$, $v_{0t} = -21$ kms^{-1}, $v_{0r} = 9$ kms^{-1} $r_{eq} = 5\text{x}10^{14}$ cm, $r_0 = 2\text{x}10^{14}$ cm, and $z_1 = 2\text{x}10^{14}$ cm (the last three quantities are subject to an arbitrary scaling factor). The greater widths of the observed line profiles, in comparison to those of the model, may be due to turbulent motions in the flow (Elitzur 1982). The calculated spectra are not very sensitive to changes in β and ε, and are similar to those shown in Figure 1b for $0.2 < \varepsilon < 2$ and $-2 < \beta < -0.2$. The fractional polarization, however, varies considerably with inclination angle. This is because the longest gain paths, which produce the strongest emission in the line profile, occur near those points in the disk where the velocity vectors are most nearly pointing toward the observer. At these points, θ approaches a minimum value, $\theta \cong i$ (in the $\underline{B}$ parallel to $\underline{v}$ case).

Therefore, the fractional polarization at the line peaks will behave in a manner similar to that given by Equation IV-5, with θ replaced by i (see Figure III-5 for a plot of Equation IV-5). In order to obtain the observed value of $m \cong 5\%$, i must be near 45° or 60°, if the fractional polarization is strictly determined by Equation IV-5. In reality, the polarization may be lowered by the effects of turbulence or cross-relaxation, making the inclination uncertain. In addition, the true field geometry is unknown, and cannot be derived uniquely from the fractional polarization, because field geometries 2 and 3 are also capable of reproducing the general features of the polarization data.

The model correctly predicts the approximate magnitude of position angle rotation for most combinations of the variable parameters and field geometries, again provided that $v_r \sim v_t$. In Figure IV-3, the direction of position angle rotation is toward smaller angles with higher absolute velocity, in accordance with the observed Orion maser polarization. This direction can be reversed (i.e., higher position angles toward higher absolute velocity) by changing the sign of either v_{t0} or i, but not both.

The position angles may be offset by a constant amount from the values shown in Figure IV-3, due to several effects:

1. The position angles depend on choice of magnetic field , and on whether θ is greater or less than 55° over the line profile (because of the 90° flip in the polarization vector at this angle).

2. A simple rotation on the sky of the apparent major axis of the disk will add a constant offset to the position angles.
3. Faraday rotation in the intervening medium may offset the position angles. Faraday effects could be significant as the radiation passes through the HII region in front of the source, but this is very uncertain since the magnetic field strength in the ionized gas is not known. The magnetic field in the KL Nebula has been measured by Hansen (1982) who finds a field strength of 4 mG using the Zeeman splitting of OH masers. If the field strength in the Orion nebula HII region was of this order, Faraday rotation could be significant because of the high density of free electrons. Using B = 1 mG, an electron density $n_e = 2 \times 10^3$ cm^{-3}, and a pathlength of 0.5 pc, a maximum Faraday rotation of roughly 10 radians is obtained at 86 GHz, if the field has no reversals and is parallel to the line of sight. The actual Faraday rotation is probably less than this, and the differential rotation between the two maser components is expected to be unimportant because of their small separation.

Because of these factors, the polarization cannot be used to uniquely constrain the magnetic field configuration, or the spatial orientation of the disk. Instead, one can estimate the position angle of the disk apparent major axis by comparing the predicted positions of the total intensity emission with the measured interferometry positions. Wright and Plambeck (1983) found the two components separated along a line at position angle -45°, with the redshifted component to

the northwest and the blueshifted component to the southeast. Figure IV-3 shows that the emission at the line peaks predicted by the model is produced at an angle of about 45° to the apparent major axis, which means that the apparent major axis must lie along an east-west line (position angle 90°). The model predicts, therefore, that the 10^{15} cm disk which produces the SiO maser emission is not coplanar with the 10^{17} cm disk of Plambeck, et al. (1982), which has an apparent major axis along position angle 45°.

§4. Conclusion

Evidence for disk geometries in maser producing regions and in the vicinity of bipolar outflows has been accumulating in recent years. Van Blerkom and Auer (1976) proposed a rotating Keplerian disk to explain a triple-peaked profile in the SiO maser emission from VY Canis Majoris. OH and H_2O masers from disk structures have been discussed by Morris et al. (1982), and Elmegreen and Morris (1979). Evidence has been presented for disks in the bipolar HII regions S106 (Bally and Scoville 1982), and NGC2071 (Bally 1982), both of which may be rotating. Of course, the site of the Orion masers is surrounded by the 10^{17} cm disk seen in SO, which is expanding. OH masers in OH104.9 are thought to be produced in a region which is both expanding and rotating (Norris et al. 1982), though the geometry appears to be more spherical than disk-like.

The model presented in this chapter uses the line profiles of both the total intensity and, more importantly, the polarization of the Orion masers to infer via simple kinematic effects the presence of a

rotating and expanding disk. In order to produce the observed rotation of polarization position angle with velocity, the radial and azimuthal velocities must be comparable. Though the exact nature of the magnetic field configuration in this disk cannot be derived from the model, the field is constrained to be of a type which rotates with azimuth around the disk.

CHAPTER V

LINEAR POLARIZATION AND TOTAL FLUX DENSITY VARIATIONS OF ACTIVE EXTRAGALACTIC OBJECTS AT 87 GHz

§1. Introduction

The millimeter wavelength properties of variable extragalactic radio sources have not been extensively studied, in comparison to other regions of the spectrum. At centimeter wavelengths variations in the flux density and polarization of a large number of sources have been closely followed, often with both high time resolution and long temporal baselines, and at multiple frequencies (e.g., Aller 1968; Dent and Kapitzky 1974; Andrew et al. 1977; Seielstad and Berge 1975; Altshuler and Wardle 1976). Such studies have formed the basis for much of our current understanding of the compact radio emitting regions of quasars, BL Lac objects, and active galactic nuclei. However, it is still unclear how the centimeter properties relate to those at meter wavelengths (e.g., Jones 1982), and to those at millimeter wavelengths (Epstein et al. 1982, hereafter EFMS).

Although several programs to monitor the millimeter total flux density of variable sources, on both short and long timescales, have been reported (Hobbs and Dent 1977; Epstein et al 1980; Balonek 1982; EFMS), only a few measurements of λ3mm polarization have appeared in the literature. Hobbs, Maran, and Brown (1978, hereafter HMB) presented preliminary polarization measurements at one epoch for 3C273,

3C345, 3C84, and 3C274 at 99 GHz using the NRAO 11m telescope. Rudnick et al. (1978, hereafter ROJPS) made multifrequency measurements, including λλ9 and 3mm, of six sources, which showed a general increase in the degree of polarization toward short radio wavelengths. Jones and Rudnick (1979) confirmed this trend for thirteen sources at λ3mm.

In this chapter the first accurate, high time resolution measurements of linear polarization in variable extragalactic sources at millimeter wavelengths are reported. Sixteen sources were observed over a seven month period in 1981 and 1982, at typical intervals of one to three weeks for the strongest sources, and even more frequently (every few days) over a two month period for 0J287. As expected, rapid and substantial variations were detected in the polarized flux density and position angle for several sources. Two rapid (timescales of order one week) and closely spaced outbursts in total flux density were seen in 0J287, with little simultaneous change in the polarization.

The aim of this chapter is to present the observational results, together with discussion of the sources based on these measurements alone. In future work, a comparison will be made between these observations and similar as yet unpublished centimeter observations, taken during the same period as part of a continuing monitoring program at the University of Michigan (Aller 1970). It is hoped that such a comparison, of both total flux and polarization, will help to clarify the relationship between the emitting regions at centimeter and millimeter wavelengths.

§2. Results and Discussion

Plots of the total flux density (S_T), position angle (χ), and polarized flux density (S_p) versus time are presented in Figure V-1 for ten active extragalactic sources. Table V-1 lists polarization and total flux measurements for all the sources. The polarized flux density has been corrected for noise bias, in accordance with the prescription of Wardle and Kronberg (1974). As can be seen in the plots occasional measurements were made of just the total flux density and not the polarization, or vice versa. Polarization position angles with uncertainties greater than 16° are not plotted. The observed sources form a rather heterogeneous group of objects, chosen mostly on the basis of their total flux density strength at λ3mm. They include:

- two "normal" (weakly polarized optically) quasars (3C273 and 2145+06);
- seven objects classified by Moore and Stockman (1981) as Highly Polarized Optical Quasars (HPOQs) (0736+01, 1156+295, 3C279, 3C345, CTA102, 3C446, and 3C454.3);
- four BL Lac objects (0235+164, OJ287, 1749+09, and BL Lac);
- one Seyfert nucleus (3C84);
- one optically unidentified object (NRAO150), and one object with a spectrum which peaks in the infrared (1413+13).

The predominence of HPOQs and BL Lac objects reflects the fact that nearly all of these types of sources (jointly classified as "blazars" by Angel and Stockman 1980) have flat or inverted radio spectra, and as

Fig.V-1. Plots of the total flux density (S_T), position angle (χ), and polarized flux density (S_P) versus time for ten sources. Flux densities are in Janskys and position angles are in degrees. Error bars represent plus and minus one standard deviation. In order to increase the signal-to- noise, the points on a small number of occasions represent averages of measurements taken a few days or less apart. All of the individual measurements can be found in Table V-1.

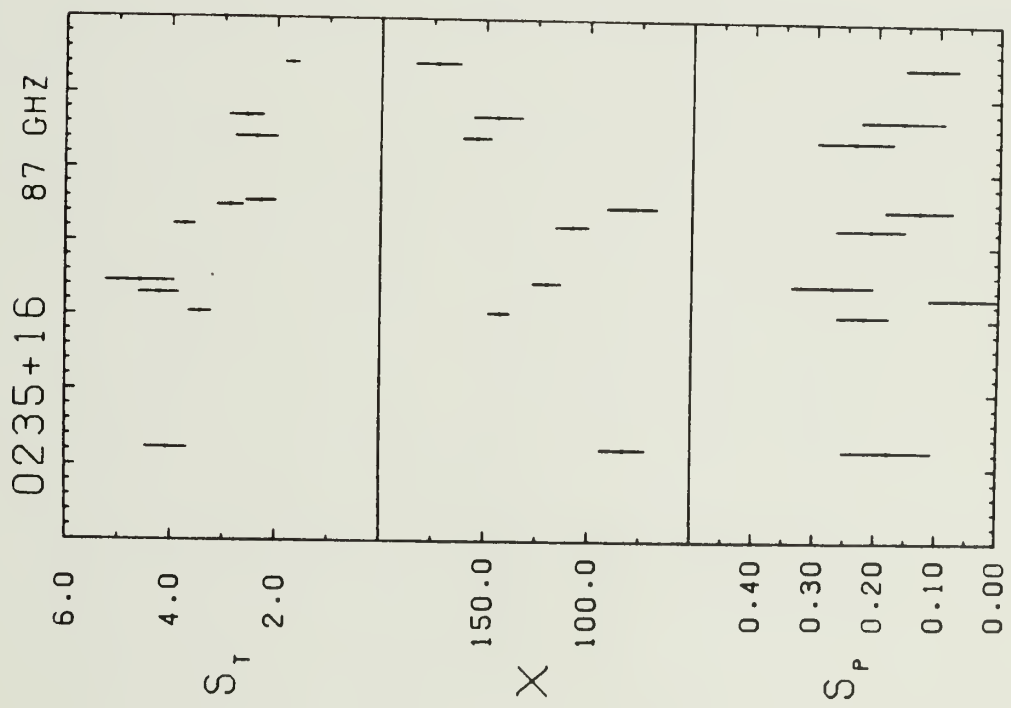
0235+16 87 GHZ
6.0
4.0
2.0
S_T
150.0
100.0
X
0.40
0.30
0.20
0.10
0.00
S_P
81.9
82.1
82.3
82.5
TIME (YR)

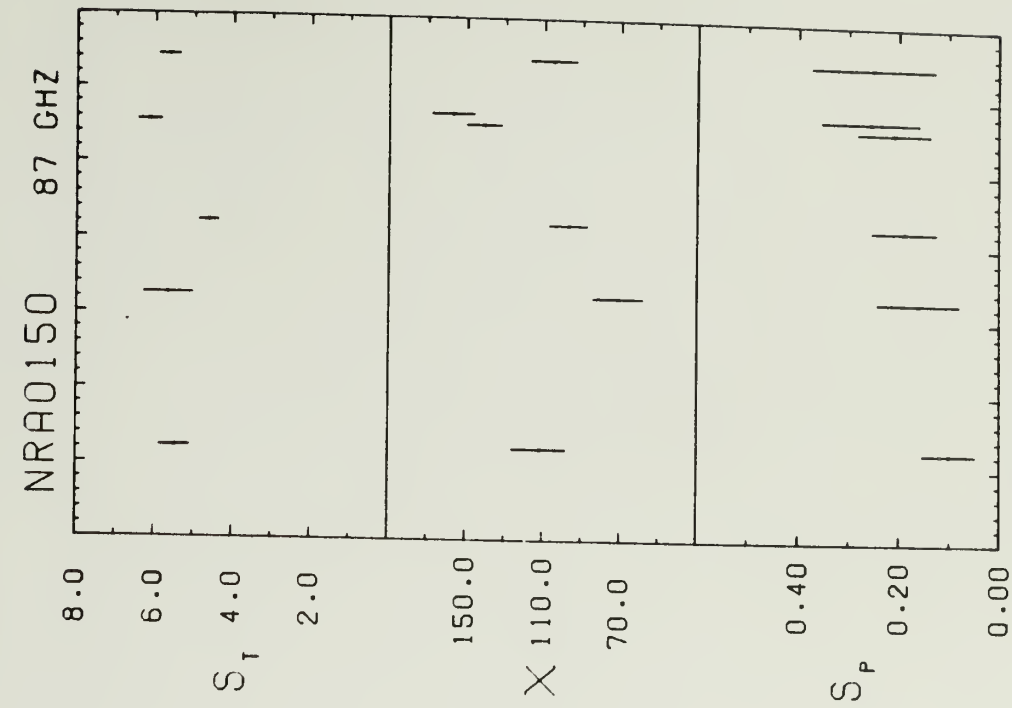
NRAO150 87 GHZ
8.0
6.0
4.0
2.0
S_T
150.0
110.0
70.0
X
0.40
0.20
0.00
S_P
81.9
82.1
82.3
82.5
TIME (YR)

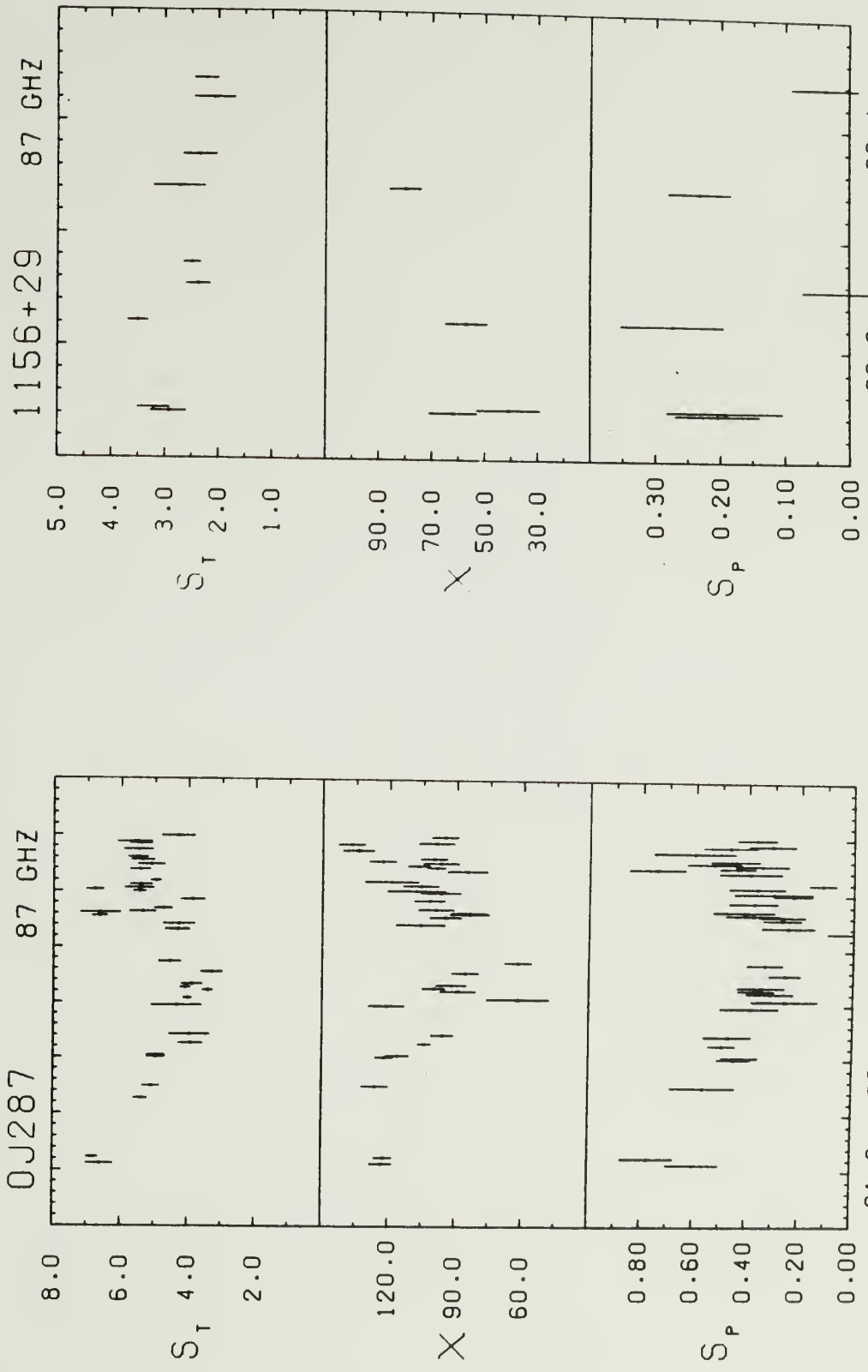
OJ287
87 GHZ
8.0
6.0
4.0
2.0
S_T
120.0
90.0
60.0
X
0.80
0.60
0.40
0.20
0.00
S_P
81.9
82.1
82.3
82.5
TIME (YR)
1156+29
87 GHZ
5.0
4.0
3.0
2.0
1.0
S_T
90.0
70.0
50.0
30.0
X
0.30
0.20
0.10
0.00
S_P
82.2
82.4
TIME (YR)

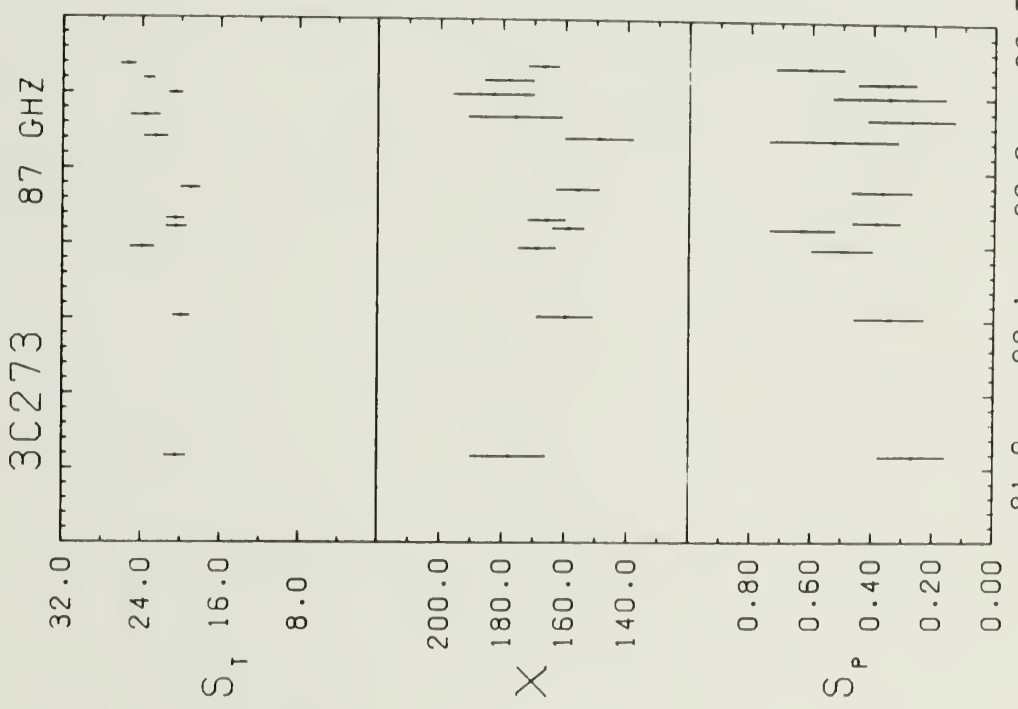
3C273
87 GHZ
32.0
24.0
16.0
8.0
S_T
200.0
180.0
160.0
140.0
X
0.80
0.60
0.40
0.20
0.00
S_P
81.9
82.1
82.3
82.5
TIME (YR)

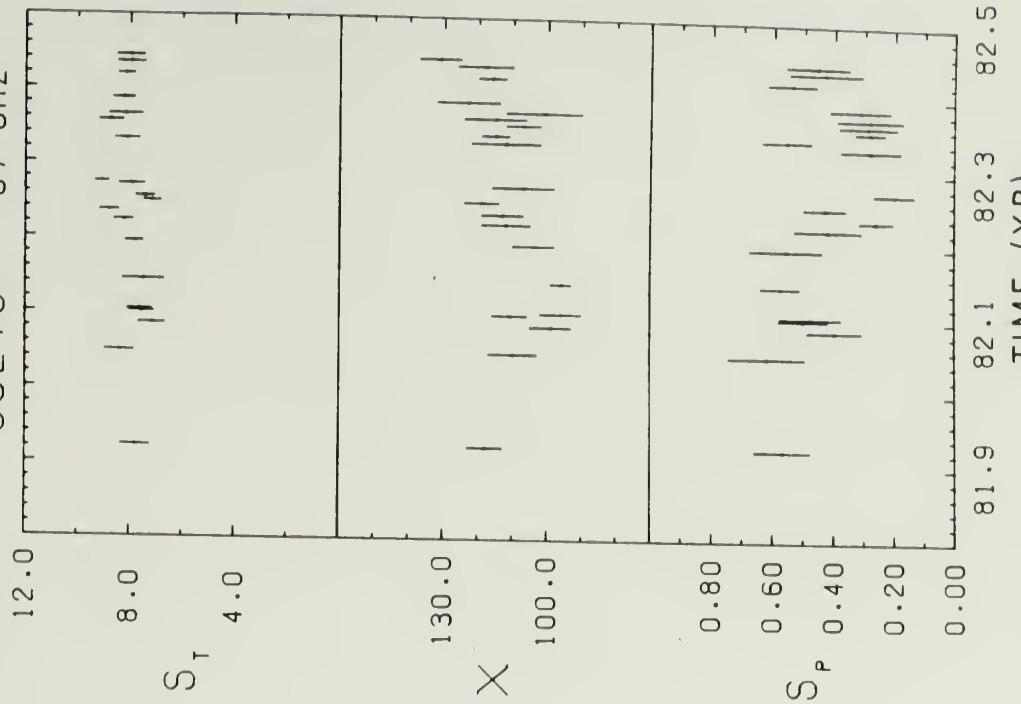
3C279
87 GHZ
12.0
8.0
4.0
S_T
130.0
100.0
X
0.80
0.60
0.40
0.20
0.00
S_P
81.9
82.1
82.3
82.5
TIME (YR)

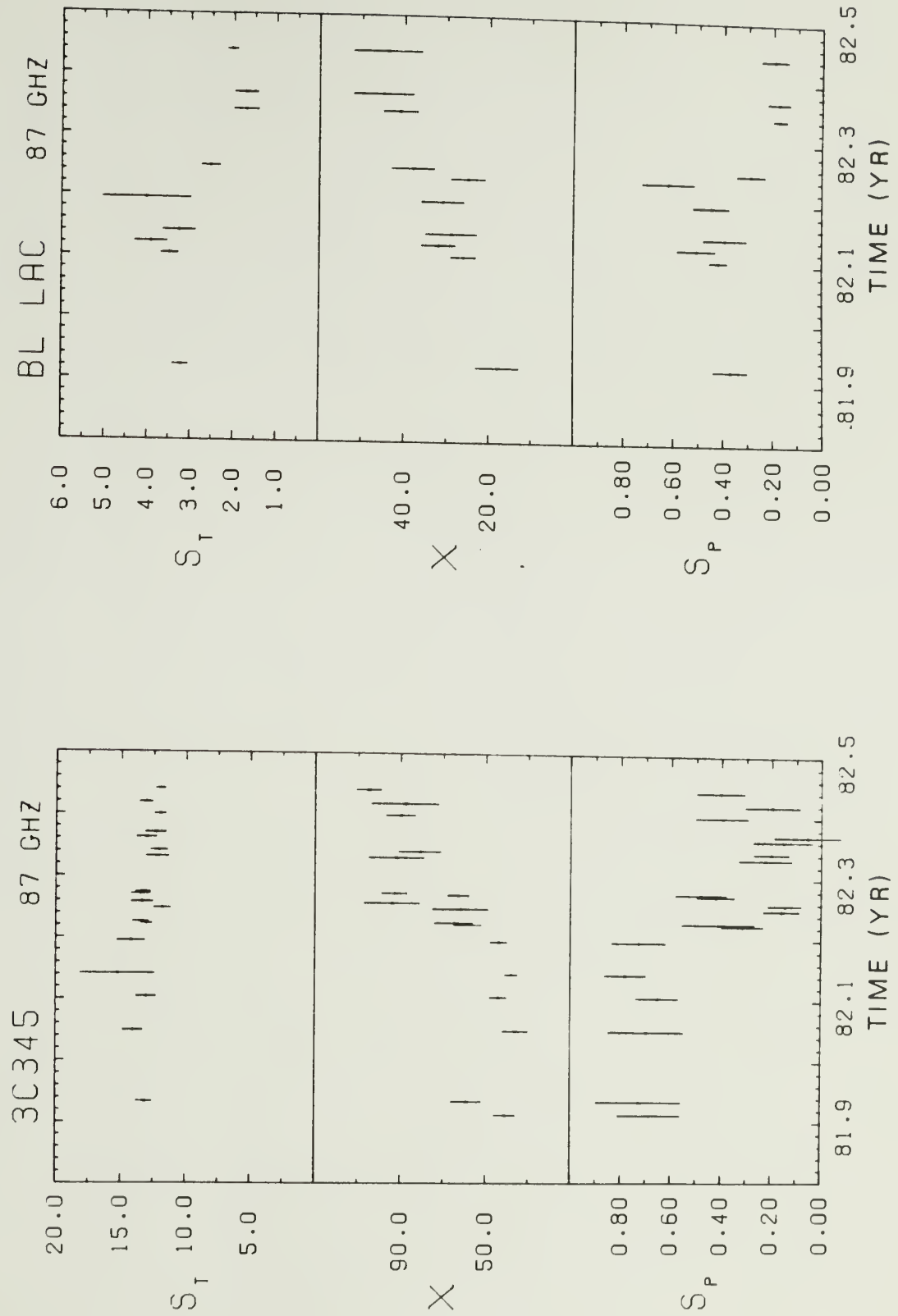
BL LAC 87 GHZ
S_T
6.0
5.0
4.0
3.0
2.0
1.0
X
40.0
20.0
S_P
0.80
0.60
0.40
0.20
0.00
81.9
82.1
82.3
82.5
TIME (YR)
3C345 87 GHZ
S_T
20.0
15.0
10.0
5.0
X
90.0
50.0
S_P
0.80
0.60
0.40
0.20
0.00
81.9
82.1
82.3
82.5
TIME (YR)

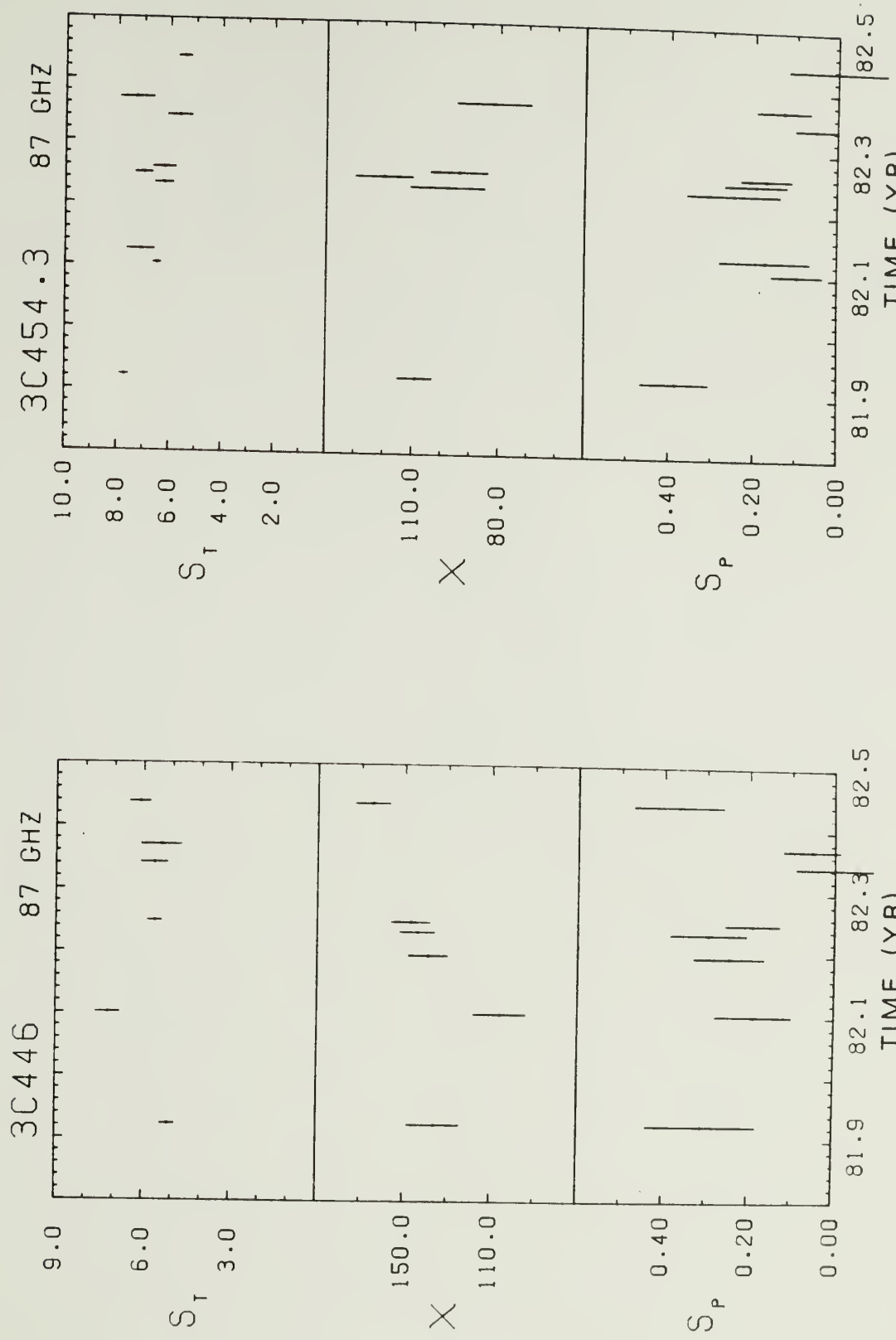
3C454.3
87 GHZ
10.0
8.0
6.0
4.0
2.0
S_T
110.0
80.0
X
0.40
0.20
0.00
S_P
81.9
82.1
82.3
82.5
TIME (YR)
3C446
87 GHZ
9.0
6.0
3.0
S_T
150.0
110.0
X
0.40
0.20
0.00
S_P
81.9
82.1
82.3
82.5
TIME (YR)

Table V-1

Polarization and Total Flux Density
Measurements of Active Extragalactic Objects

Source	Date	S_P(Jy)	ΔS_P	χ(°)	$\Delta\chi$	S_T(Jy)	ΔS_T
0235+164	12/4/81	.180	.073	83	11	4.07	.40
	2/8/82	.221	.042	143	5	3.44	.22
	2/15/82	.059	.055	-	-	4.22	.38
	2/23/82	.271	.066	120	7	4.58	.65
	3/27/82	.210	.056	108	8	3.74	.20
	4/2/82	.131	.055	79	12	2.87	.25
	4/4/82	-	-	-	-	2.29	.29
	5/6/82	.236	.062	154	7	2.38	.40
	5/16/82	.159	.068	144	12	2.57	.33
	6/10/82	.112	.043	172	11	1.71	.14
NRAO150	12/4/81	.101	.053	112	15	5.47	.35
	2/23/82	.161	.082	71	15	5.64	.63
	3/27/82	.189	.065	97	10	4.62	.25
	5/11/82	.209	.073	141	9	6.13	.31
	5/16/82	.256	.098	157	11	-	-
	6/12/82	.251	.123	105	14	5.63	.30
3C84	11/29/81	.257	.304	-	-	52.4	2.3
	2/8/82	.432	.182	28	12	48.2	0.9
	2/16/82	.451	.223	132	14	55.7	4.2
	2/22/82	.421	.286	-	-	54.7	4.7
	3/27/82	.233	.191	-	-	47.7	1.4
	4/1/82	-	-	-	-	47.8	1.0
	4/4/82	-	-	-	-	48.2	2.9
	5/11/82	.105	.146	-	-	50.3	1.4
0736+01	12/4/81	.192	.049	41	7	2.50	.22
	2/16/82	.165	.063	68	11	1.86	.39
	3/18/82	-	-	-	-	2.02	.20
	4/2/82	.120	.045	141	11	2.56	.31
	4/4/82	.042	.048	-	-	3.07	.48
	5/11/82	-	-	-	-	2.27	.60

Table V-1 (cont.)

Source	Date	S_P(Jy)	ΔS_P	χ(°)	$\Delta\chi$	S_T(Jy)	ΔS_T
OJ287	11/29/81	.600	.100	123	5	6.60	.40
	12/4/81	.774	.100	122	4	6.82	.17
	1/19/82	.565	.122	126	6	5.09	.25
	2/7/82	.449	.062	122	4	4.95	.26
	2/8/82	.426	.068	116	5	-	-
	2/16/82	.494	.051	104	3	3.92	.38
	2/22/82	.473	.089	96	5	3.96	.61
	3/13/82	.391	.111	121	8	4.34	.75
	3/18/82	.259	.125	62	14	4.02	.12
	3/23/82	.315	.088	89	8	3.42	.15
	3/25/82	.367	.068	100	5	4.09	.15
	3/27/82	.348	.089	92	7	3.89	.31
	4/4/82	.258	.059	86	6	3.30	.32
	4/10/82	-	-	-	-	4.25	.47
	4/11/82	.334	.068	62	6	4.54	.34
	5/2/82	~0	.102	-	-	4.32	.36
	5/6/82	.248	.100	106	11	4.29	.47
	5/11/82	.270	.072	95	7	6.63	.22
	5/13/82	.270	.087	84	9	6.61	.59
	5/14/82	.381	.102	84	8	5.36	.39
	5/16/82	.415	.116	99	8	4.74	.27
	5/22/82	.380	.093	102	7	3.87	.36
	5/27/82	.230	.072	97	9	5.45	.19
	5/28/82	.304	.149	108	14	6.77	.25
	5/29/82	-	-	-	-	5.46	.43
	5/31/82	.366	.106	106	8	5.41	.32
	6/3/82	.118	.050	119	12	4.97	.15
	6/10/82	.374	.119	85	9	5.43	.30
	6/11/82	.345	.189	123	16	5.12	.39
	6/12/82	.737	.105	99	4	-	-
	6/13/82	.436	.068	107	5	4.65	.31
	6/15/82	.348	.101	97	8	-	-
	6/16/82	.530	.102	123	6	5.36	.35
	6/18/82	.450	.093	100	6	5.50	.30
	6/23/82	.603	.156	134	7	5.49	.43
	6/27/82	.469	.102	137	6	5.41	.32
	6/28/82	.309	.088	99	8	5.60	.51
	7/2/82	.369	.076	95	6	4.30	.49

Table V-1 (cont.)

Source	Date	S_P(Jy)	ΔS_P	χ(°)	$\Delta\chi$	S_T(Jy)	ΔS_T
1156+295	2/22/82	.204	.065	62	9	2.93	.33
	2/23/82	.193	.089	41	13	3.21	.30
	3/23/82	.274	.079	57	8	3.50	.19
	4/4/82	~0	.072	-	-	2.39	.22
	4/11/82	-	-	-	-	2.50	.16
	5/6/82	.232	.048	80	6	2.73	.48
	5/16/82	-	-	-	-	2.35	.31
	6/3/83	-	-	-	-	2.07	.38
	6/10/82	.038	.052	-	-	2.22	.22
3C273	11/29/81	.270	.145	173	15	-	-
	12/4/81	.324	.168	2	15	20.5	1.5
	2/7/82	.346	.114	160	9	20.0	0.8
	3/13/82	.500	.100	169	6	23.9	1.2
	3/23/82	.630	.106	159	5	20.5	1.0
	3/27/82	.389	.078	166	6	20.6	0.9
	4/11/82	.371	.099	156	7	19.0	1.0
	5/6/82	.529	.210	149	11	22.6	1.2
	5/16/82	.274	.144	176	15	23.6	1.5
	5/27/82	.347	.185	3	15	20.6	0.8
	6/3/82	.355	.096	178	8	23.3	0.6
	6/9/82	-	-	-	-	23.7	0.8
	6/10/82	.607	.112	167	5	25.4	0.8
3C279	12/4/81	.568	.091	118	5	7.79	.55
	1/19/82	.618	.125	110	6	8.40	.58
	2/2/82	.397	.089	99	6	7.17	.52
	2/7/82	.499	.080	111	5	7.55	.49
	2/8/32	.476	.100	96	6	7.65	.48
	2/23/82	.574	.063	96	3	7.51	.78
	3/13/82	.555	.119	104	6	7.85	.35
	3/27/82	.419	.110	112	7	8.26	.37
	3/28/82	.260	.056	113	6	8.79	.39
	4/2/82	.438	.092	120	6	7.15	.36
	4/4/82	.420	.103	117	7	7.44	.37
	4/10/82	.178	.076	110	12	7.93	.50
	4/11/82	.274	.135	103	14	9.09	.27
	5/2/82	.278	.100	112	10	8.13	.50
	5/6/82	.554	.081	115	4	-	-
	5/11/82	.280	.049	107	5	8.72	.47
	5/14/82	.287	.096	115	9	8.17	.65
	5/17/82	.281	.109	101	11	-	-

Table V-1 (cont.)

Source	Date	S_P(Jy)	ΔS_P	χ(°)	$\Delta\chi$	S_T(Jy)	ΔS_T
3C279	5/17/82	.281	.109	101	11	-	-
	5/22/82	.314	.101	123	9	8.25	.42
	6/3/82	.539	.079	116	4	8.13	.32
	6/9/92	.428	.120	118	8	7.96	.55
	6/12/82	.445	.103	131	6	7.98	.54
1413+13	2/23/82	.107	.035	109	9	2.22	.48
	3/13/82	.152	.072	167	14	-	-
	3/25/82	.076	.062	-	-	1.83	.14
	5/11/82	~0	.055	-	-	2.55	.39
	6/10/82	-	-	-	-	2.19	.28
3C345	11/29/81	.685	.124	41	5	-	-
	12/4/81	.727	.169	59	7	13.2	0.6
	1/19/82	.698	.149	36	6	14.1	0.8
	2/8/82	.654	.085	44	4	13.1	0.8
	2/22/82	.782	.081	38	3	15.3	2.9
	3/13/82	.728	.107	44	4	14.2	1.1
	3/27/82	.316	.082	58	7	13.0	0.4
	3/28/82	.412	.144	65	9	13.5	0.6
	4/2/82	.160	.071	62	13	11.9	0.6
	4/5/82	.147	.067	94	13	13.4	0.9
	4/10/82	.422	.074	63	5	13.5	0.7
	4/11/82	.481	.100	93	6	13.3	0.6
	5/2/82	.255	.106	92	12	12.2	0.9
	5/6/82	.202	.071	81	10	12.1	0.7
	5/11/82	-	-	-	-	13.8	0.6
	5/13/82	.154	.119	-	-	13.1	0.8
	5/16/82	.056	.134	-	-	12.3	0.8
	5/27/82	.398	.106	90	7	12.0	0.5
	6/3/82	.197	.110	88	16	13.1	0.5
	6/11/82	.404	.096	95	7	12.0	0.4
1749+09	2/7/82	.148	.026	2	5	2.50	.25
	2/23/82	.092	.055	-	-	2.18	.29
	3/27/82	-	-	-	-	1.74	.22
	4/2/81	-	-	-	-	1.73	.24
	5/16/82	-	-	-	-	1.40	.44
	6/10/82	.019	.088	-	-	2.78	.22
2145+06	2/8/82	.108	.070	-	-	2.47	.21
	4/4/82	.067	.073	-	-	3.36	.23

Table V-1 (cont.)

Source	Date	S_P(Jy)	ΔS_P	χ(°)	$\Delta\chi$	S_T(Jy)	ΔS_T
BL Lac	12/4/81	.369	.068	18	5	3.22	.18
	2/8/82	.418	.035	26	3	3.48	.20
	2/15/82	.507	.076	32	4	3.92	.38
	2/22/82	.392	.087	29	6	3.26	.38
	3/13/82	.447	.072	31	5	4.02	1.0
	3/27/82	.620	.104	25	4	-	-
	4/2/822	.287	.056	38	5	2.53	.22
	5/6/82	.171	.027	41	4	1.71	.29
	5/16/82	.176	.045	45	7	1.71	.27
	6/11/82	.194	.054	44	8	2.03	.12
3C446	12/4/81	.310	.129	136	12	5.12	.24
	2/7/82	.190	.089	106	13	7.20	.41
	3/13/82	.247	.082	139	9	-	-
	3/27/82	.296	.089	144	8	-	-
	4/2/82	.193	.064	147	9	5.61	.25
	5/6/82	~0	.091	-	-	5.62	.47
	5/16/82	.054	.067	-	-	5.37	.70
	6/10/82	.367	.105	165	8	6.12	.36
CTA102	5/17/82	.085	.065	-	-	2.74	.46
3C454.3	12/4/81	.386	.081	109	6	7.71	.17
	2/8/82	.095	.060	109	18	6.48	.15
	2/16/82	.172	.107	88	17	7.11	.53
	3/27/82	.247	.110	98	13	6.21	.36
	4/2/82	.194	.073	120	10	6.99	.33
	4/5/82	.169	.061	94	10	6.21	.44
	5/6/82	.052	.049	-	-	5.62	.47
	5/16/82	.130	.064	82	14	7.27	.65
	6/10/82	~0	.118	-	-	5.43	.24

a result are strong at millimeter wavelengths. Three sources (OJ287, 3C279, and 3C345) were observed more frequently than the others, due to their inherent interest and the relatively high availability of telescope time (because of the unavailability of galactic molecular line sources) during the LST range when they were in the sky.

Discussions of some of the more interesting sources are given below. Information on the λ3mm total flux behavior prior to 1982 referred to in the discussions is from Balonek (1982) and Dent and Balonek (1983).

0235+164. When the polarization observations commenced, this source was at the peak of a λ3mm total flux density outburst that began at 1981.5, and which declined back to its pre-outburst level by the time of the last observation. One of the initial aims of this program was to investigate the phenomenon of linear rotation of polarization position angle with time, for which this source was the first known example (Ledden and Aller 1979). Other sources exhibiting position angle rotation have been reported by Altshuler (1980), and Aller, Hodge, and Aller (1981), but generally the effect is only seen for short periods after the maximum of an outburst. Since frequency dependent mechanisms such as Faraday rotation are ruled out because the rotations are often seen to track precisely at different centimeter wavelengths, the above authors suggest physical rotation of the magnetic field structure as the simplest explanation. Ledden and Aller (1979) suggested that the physical rotation may be occurring continuously deep in the core of the emitting region, but that it is

usually masked by opacity effects at centimeter wavelengths (except, for example, after an outburst, when the source becomes transparent). Hence the motivation for millimeter observations: the millimeter opacity should be much smaller than the centimeter opacity, and this should provide an unobscured view of the site of the putative rotation. If opacity is an important factor, the observations reported here have the extra advantage that the source was in the declining phase of an outburst, when it might be expected to be most transparent. However, no good evidence for uniform rotation was found. The mean value of position angle is 125°, with an RMS scatter about the mean of 34°. Attempts to find a better fitting line of constant slope, by introducing 180° phase shifts, failed to reduce the scatter. No convincing case of large amplitude linear rotation of position angle with time was seen for any source during this program, although the data are insufficient to rule out this phenomenon in some sources.

NRA0150. The total flux density of this source was in a quiescent phase at λ3mm prior to and during the observations, the weakest it has been during the last 12 years. The polarized flux density shows a mildly increasing trend, while the position angle varied over a range of 90°. The data are too sparse to discern any definite trends in the position angle variations.

3C84 (NGC1275). This well known Seyfert nucleus has consistently shown weak or non-existent (< 1%) polarization at all radio frequencies (see Tabara and Inoue 1978 for a compilation of radio observations), although in the optical it has shown polarization as high as 6% (see Angel and Stockman 1980). Four of the six λ3mm measurements are con-

sistent with zero polarization, and the two measurements with signal to noise ratio greater than 2 are both below the 1% level (see Table V-1).

0J287. This is one of the most highly variable sources known at both optical and radio frequencies with an extensive literature documenting its behavior (see Angel and Stockman 1981; and Epstein et al. 1980, and references therein). Perhaps the most interesting aspect of 0J287 seen here are two successive, extremely rapid outbursts in the total flux density, which occurred just prior to 1982.4. In the first outburst, S_T increased by 50% (from 4.3 to 6.6 Jy) in less than 5 days, then fell back to its original level in a week or less. This outburst occurred after S_T had bottomed out at 4 Jy, following a longer term outburst which began at 1980.5 and reached a maximum total flux density of about 7 Jy at 1981.5. The second rapid outburst immediately followed the first, and consisted of a 75% rise (3.9 to 6.8 Jy) in about 6 days, followed by a quick decline to an intermediate level of 5.5 Jy, where S_T remained for the next month.

Although several large variations with timescales of days have been seen previously in this source and others, practically all of these events have been dropouts in the flux density, rather than rises (Epstein et al. 1980; hereafter EFMS). The outbursts reported here are therefore rather unusual in that they involve large changes on timescales of days, which include both rises and falls. Interestingly, these rapid events appear to have been unpolarized, in contrast to the radiation associated with the preceding long term outburst which was polarized at a constant level of about 10%. Although there was measurable polarized flux density present during these events, it would

appear that this was due to the base level component of total flux density upon which the rapid outbursts were superposed.

A previous λ3mm measurement of the polarization was made by ROJPS, giving 12.4 ± 1.5% at 92 ± 6°. These are close to the mean values of 9.8% at 100° found here. At short centimeter wavelengths, the position angle is generally between 70° and 100° , with only occasional excursions outside this range (Aller, Aller, and Hodge 1981; Altshuler and Wardle 1976). The optical polarization has also shown a similar position angle (Kinman 1978; Impey and Brand 1981), and changes in the fractional polarization in the optical and radio have shown a long term correlation (Wardle 1978). VLBI experiments show a circular Gaussian source structure down to a resolution of 0.3 milliarcseconds (Pauliny Toth et al. 1981).

3C273. The total flux density and polarization varied only mildly, if at all, in this source, which was undergoing an outburst of ~ 10-15 Jy that began at about 1980.0. The polarization position angle averaged 167°, similar to the mean value of about 150° generally seen at centimeter wavelengths (see Tabara and Inoue 1978) and the λ3mm value of 153 ± 4° measured by ROJPS. This direction is approximately perpendicular to the axis along which the superluminal expansion is taking place (Pearson et al. 1981), and implies a magnetic field which is parallel to the jet.

3C279. The position angle varied between 96° and 130°, with a mean value of 111°, again approximately perpendicular to the VLBI structure at PA 30° (Pauliny Toth et al. 1981). The polarized flux density fell off by about a factor of two during the observations,

while the total flux density remained fairly constant, with perhaps some flickering at the 15% level, at the peak of a small outburst. This source has been discussed by Aller and Olsen (1971), who found that χ is, at different times, either parallel or perpendicular to the direction of the superluminal expansion. They attributed this to a 90° flip in the magnetic field as a separating component evolves and encounters ambient material in its path. A view more in line with the current models might invoke changes in the magnetic field structure as the source travels down a jet, as will be discussed for the next source.

3C345. During the observations, this source was at the peak of a large outburst which began in 1978. The polarized flux density was constant at about 0.7 Jy ($m \cong 5\%$) from 1981.9 to 1982.2, then dropped to 0.1 - 0.2 Jy ($m \cong 1\%$) over a period of three weeks. This falloff was accompanied by a rotation of 50° in position angle, but with little or no corresponding change in total flux density. By 1982.4, Sp had risen somewhat to about 0.4 Jy ($m \cong 3\%$) and χ had stabilized at 90° (at 1983.2 m and χ were still about 3% and 90°). This sort of behavior - rapid changes in polarization with no change in total flux density - has been seen previously in several sources, at both optical and radio wavelengths (see Impey, Brand and Tapia 1981, and references therein). Altshuler and Wardle (1977) have pointed out the difficulties of interpreting polarization variations of this type, which are probably not due to Faraday rotation or optical depth effects (see also Wardle 1978).

Changes in the polarization like those seen here for 3C345 may

be due to changes in the magnetic field structure in which the radiating particles find themselves as an outburst progresses. In this context, it is interesting to note that the polarization variations with time in 3C345 are qualitatively similar to the polarization variations with distance along the large scale jets of some radio galaxies (e.g., Fomalont et al. 1980). In particular, these jets often exhibit three regimes: one near the base, where the polarization is strong, and the field well-ordered and more of less parallel to the jet axis; this is followed by a weakly polarized, disordered region where the magnetic field changes direction; finally, further from the nucleus, the polarization increases in strength and the field becomes perpendicular to the jet axis. For 3C345, the final position angle of 90° indicates a field which is indeed almost perpendicular to the direction (position angle -79°) along which the superluminally expanding VLBI components are being ejected (Unwin et al. 1983).

It is thus tempting to associate the variations in polarization with changes in magnetic field structure as the radiating particles propagate along a jet, although the observed rotation of only 50° in χ makes the analogy less than perfect. Aller, Aller, and Hodge (1981) have suggested a similar scenario to account for the polarization variations seen in several sources at centimeter wavelengths. It must be pointed out that the size scales of the extended radio galaxy jets and the region of the millimeter variability are different by a factor of at least 10^4. However, this should not be too disconcerting, since the fields in the jets of the galactic source SS433 might be quite similar to those in radio galaxy jets (Hjellming and Johnston 1981),

and Rees (1981) has argued that jet formation mechanisms may be similar on all size scales (see also Marsher 1980).

BL Lac. The extensively studied class prototype has shown many of the extremes of behavior of variable sources at centimeter wavelengths, including large and rapid variations in total and polarized flux density, and extremely rapid rotation in position angle, but has also exhibited more quiescent periods (e.g., Aller, Aller, and Hodge 1981). The interval represented here finds BL Lac peaking and then declining from a small outburst, of duration about one year. The fractional polarization was constant at about 10 to 12%, as the polarized flux density closely tracked the variations in total flux density. The position angle increased monotonically by 20° meanwhile, and all variations appear to be well resolved in the data.

3C454.3. The fractional polarization varied between 1 and 5%, with no apparent systematic trends, while the total flux density was on the declining side of a large outburst which peaked at 10 Jy in 1981.6. The position angle varied between 80 and 120° (also apparently randomly, with this time resolution), with a mean value of 101°, close to the direction of the VLBI structure at position angle 115° (Pauliny Toth et al. 1981), implying a mean magnetic field aligned perpendicular to the jet axis.

§3. Conclusions

Since it is extremely likely that BL Lac is, at times, as active at millimeter as at centimeter wavelengths, the unremarkable characteristics of this source found here should serve as a reminder that the

limited time interval of this study is insufficient to disclose the full range of variations in individual sources. It is perhaps more useful to consider the range of behavior presented by the sources as a group. From an examination of Figure V-3, and from the above discussions, it would appear that the millimeter variations are qualitatively similar to those seen at other radio wavelengths. To what extent they are quantitatively the same, on a source by source basis, will have to await the comparison with the concurrent centimeter observations.

That no source was seen to undergo large amplitude linear rotation of position angle with time argues that the intermittent nature of this phenomenon at centimeter wavelengths is not due to opacity effects. At 87 GHz, the synchrotron opacity should be two orders of magnitude smaller than it is at 15 GHz and below, the frequencies where the rotations have been seen. If the continuously rotating magnetic field structure of, say, a spinar becomes visible only when the radiation is unusually transparent at centimeter wavelengths, it should be commonly visible in the millimeter band, but was not observed here for any source.

The rapid outbursts in total flux density seen in 0J287 emphasize the point, made by EFMS, that the full time spectrum of millimeter variations cannot be determined without almost daily measurements. The observation of significant (~ 20%) changes in one day (which include outbursts in this case, in contrast to the quenchings seen in other instances) brings the form and timescale for the most rapid millimeter variations into the range of the optical variability (see Epstein et

al. 1980, for discussion and references on rapid radio and optical variability). The implied brightness temperature of $\sim 10^{14}$ K ($z = .306$) for the OJ287 outbursts points up the need for relativistic source motion to boost the intensity, but no more so than have other events at lower frequencies (e.g., Ledden, Aller, and Dent 1976; Padrielli 1982).

Finally, several sources have polarization position angles indicating magnetic fields which are either parallel or perpendicular to the direction of the milli-arcsecond structure (3C273, 3C274, 3C279, 3C345, and 3C454.3). Since large-scale jets in radio galaxies usually have magnetic fields which are either parallel or perpendicular to their axes, and since the characteristics of jets may be similar on all size scales (e.g., SS433), the observed radio polarization may be providing indirect evidence for jet or jet-like structures. Indeed, some sources may show the effects of changing magnetic fields as the radiating particles propagate along a jet, as was suggested here to account for the variations in 3C345.

CHAPTER VI

TOTAL FLUX DENSITY SPECTRA FROM CENTIMETER TO MILLIMETER WAVELENGTHS

§1. Introduction

In Chapter V, where the λ3.5mm total flux density and polarization measurements were presented, reference was made to similar data at centimeter wavelengths obtained as part of a continuing program at the University of Michigan. This data has been made available to the author, and in this chapter observations at 87 GHz (FCRAO), 4.8, 8.0, and 14.5 GHz (University of Michigan, kindly supplied by H. Aller), and 31 and 90 GHz (NRAO, kindly supplied by W. Dent) will be combined in an effort to analyze the broadband total flux density spectra of a sample of compact variable sources. The University of Michigan data set also includes linear polarization measurements, but comparison of the centimeter and millimeter polarizations will be left to future work.

It is not the intent here to attempt to explain the detailed multi-frequency behavior of the flux density variations of all of the sources. While it is generally thought that the standard adiabatic expansion model of van der Laan (1966) and its various modifications (e.g., Peterson and Dent 1973) can qualitatively account for the variations observed in many sources (see review by Kellerman and Pauliny-Toth 1981), such simple models usually fail when applied quantitatively. Most real outbursts probably evolve in such a way that optical depth

effects and expansion losses are important, but other factors including source geometry, relativistic motion, and particle acceleration may complicate the picture considerably. To paraphrase a comment made by Rees (1981) in a slightly different context, the understanding of detailed variations in quasars may be as difficult and challenging as computational meteorology.

Instead a more modest approach is proposed, emphasizing the following points:

1. To document the broadband spectra of 13 compact variable sources.
2. To compare the observed spectral shapes with those expected from model predictions, and derive physical parameters based on the models.
3. To discuss a variable source model and apply it to the spectral evolution of one source particularly well suited to analysis (0235+164) because of the comparatively simple nature of its variations.

These points will be addressed following an outline of the general problem of compact source spectra, and somewhat more detailed discussions of current models for explaining the observed spectral shapes and spectral evolution.

§2. Broadband Spectra

Background.

One of the outstanding problems in the study of compact extragalac-

tic radio sources is the origin of their broadband continuum spectra. Implicit in the spectral flux density distribution and its variability are clues to understanding the energy distribution of the radiating particles, their means of acceleration and energy loss, and the geometric structure of the radiating regions. It is almost universally assumed that incoherent synchrotron radiation from relativistic electrons is the fundamental emission mechanism in the radio regime. One piece of evidence strongly supporting this assumption is the observation of significant linear polarization from a broad range of source types, including unresolved compact variables, through kiloparsec scale jets, on up to megaparsec scale radio lobes. Furthermore, it is commonly assumed that the radiating electrons conform to a power law distribution in energy, such that $n(E) = n_1 E^{-\gamma}$.

This latter assumption is clearly justified for resolved, extended structures such as radio galaxy lobes and jets, for in these cases the observed flux density spectra are power laws, the natural result of power law electron distributions. However, for compact variable sources this is frequently not the case. Indeed, such sources often exhibit spectra which are much too broad and flat to be consistent with radiation from a single, homogeneous region of power law electrons (e.g., Marscher 1977b). Such a region will produce a spectrum which falls off as $S_\nu \propto \nu^\alpha$ ($\alpha \sim -0.5$) in the high optically thin regime, and which rises as $S_\nu \propto \nu^{2.5}$ in the self-absorbed part of the spectrum. Between these two regimes is the spectral turn-over, which occurs at some peak frequency designated ν_m.

Spectra which rise below the turnover with indices as large as 2.5

are almost never seen in compact sources, and often the spectra are not simple power laws at low or high frequencies. In view of this, it has long been recognized (e.g., Kellerman and Pauliny-Toth 1968) that the homogeneous, single component, power law electron model is inadequate for the description of compact sources, and that other models must be sought. These models fall into two basic classes:

Inhomogeneous source models. In this class of models the power law electron distribution is retained, but the radiating region is generalized to include some type of non-uniformity. The geometry might be such that the source is made up of a number of spatially separate uniform components, each with different values of physical parameters relevant to the spectrum (B, n, γ, etc.). Alternatively, the source might be a single non-uniform region with smoothly varying values of these parameters (Condon and Dressel 1973; deBruyn 1976; Marscher 1977a; Blandford and Konigl 1979; Konigl 1981). In either case the flattening of the spectrum is accomplished by superposition of spectra with different turnover frequencies, and a variety of shapes can result.

Non-power law electron distributions. The most widely discussed alternative to the power law distribution is the relativistic Maxwellian distribution, in which the electrons are thermal but moving at near the speed of light. The electrons still radiate predominantly by the synchrotron mechanism in the presence of a magnetic field. It has been suggested that this distribution may be produced naturally in the shocked region behind a relativistically expanding blast wave, and its spectral properties have been analysed in detail by Jones and

Hardee (1979). The advantage of the Maxwellian in the present context is that it is capable of producing broad, gently curved spectra, over a decade or more in frequency, from a single homogeneous source component.

Observational attempts to assess the viability of these models have been made in a number of studies over the past few years, with ambiguous results. Cotton et al. (1980) made multifrequency Very Long Baseline Interferometry (VLBI) and total flux density measurements of the flat spectrum source 0735+178, in order to determine if the spectrum is due to a single spatial component or multiple components. They found three distinct components from VLBI, and inferred the presence of a fourth from the total flux density measurements. Their data are inconsistent with the single, inhomogeneous component model. Wittels, Shapiro and Cotton (1982) performed a similar experiment on another flat spectrum source with similar results.

However, a disturbing aspect of this interpretation is that the individual subcomponents must have spectral peaks which are arranged in frequency in such a way as to produce an overall flat spectrum. Cotton et al. dubbed this a "cosmic conspiracy", as there is no known physical mechanism which could reproduce such a highly tuned arrangement in a large number of sources.

Cook and Spangler (1981) took a somewhat different tack by fitting multiple homogeneous or inhomogeneous source theoretical spectra to observed total flux density spectra alone (without VLBI measurements). Their results indicate that the multiple homogeneous component model is highly unlikely, but that a multiple inhomogeneous component model

requires less contrivance and may be generally applicable. Such an approach unfortunately yields little information about source geometry or subcomponent characteristics.

Spangler (1980) compared the spectral shapes of a large sample of sources with those expected from the tapered (inhomogeneous) source model of Marscher (1977a) and the relativistic Maxwellian model. He found that some sources are fit quite well by the Maxwellian, others are consistent with the tapered source model, while a third class are not well-represented by either. In a follow-up to this study, VLBI measurements were made of ten of these sources (Spangler et al. 1981), two of which showed more than one component. The remaining eight sources were consistent with single component models in the homogeneous source (one source), tapered source (three sources), or Maxwellian (two to four sources) categories.

Ennis, Neugebauer, and Werner (1982) discussed radio spectra from centimeter wavelengths through λ1mm, together with infrared-optical data. They found that the spectra of many sources are consistent with synchrotron radiation from a relativistic jet with power law electrons (an inhomogeneous source model). O'Dea, Dent, and Balonek (1983) have used spectral variations to decompose the radio spectrum of 3C84 into a series of multiple, homogeneous components.

Our approach to this problem will be similar to that of Spangler (1980) discussed above. In what follows, the two models which will be fit to the observations are reviewed in some detail.

Models.

Inhomogeneous jets. Here we will follow the relativistic jet analysis of Konigl (1981) as representative of the class of inhomogeneous source models. The tapered spherical source model of Marscher (1977a) gives similar results. In the Konigl model it is assumed that the jet is viewed at a small angle to its axis, that the magnetic field strength and particle density are given as simple power law functions of distance R along the jet axis (R=0 at the source core), and that the electron distribution is a power law function of energy such that

$$B(R) = B_1 R^{-b} , \qquad \text{(VI-1)}$$

$$n(E,R) = K R^{-k} E^{-\gamma} . \qquad \text{(VI-2)}$$

The resultant synchrotron spectrum is characterized by power laws above and below the turnover frequency, viz., $S_{thk} \propto \nu^{\alpha thk}$ and $S_{thn} \propto \nu^{\alpha thn}$ (α_{thk} and α_{thn} correspond to Konigl's $-\alpha_{s1}$ and $-\alpha_{s2}$ respectively). The power law indices depend on b and k (Konigl's m and n), and γ, according to lengthy but straightforward algebraic expressions given by Konigl. At the turnover, the power laws join together smoothly. Fits to the data for α_{thk} and α_{thn} will be used to derive possible values for k and b.

Relativistic Maxwellian distribution. In this case the source is assumed to be homogeneous with the electron energy distribution given by

$$n(\gamma) = \tfrac{1}{2}\, n_o \gamma^2\, T^{-3} \exp(-\gamma/T) \qquad \text{(VI-3)}$$

where γ is the energy of the electrons in units of $m_e c^2$ (γ not to be confused with the power law index used earlier), and T is their temperature in units of $m_e c^2/k$. See Jones and Hardee (1979, hereafter JH) for more details on this and the following.

The solution of the transfer equation (see, e.g., Jones and O'Dell 1977 for the general solution) gives

$$I_\nu = 2m_e T \nu^2 \left(1 - e^{-\tau_\nu} \cosh \zeta_Q \tau_\nu\right) . \qquad \text{(VI-4)}$$

The optical depth is given by

$$\tau_\nu = \tau_1 z^{-2} I(z) \qquad \text{(VI-5)}$$

where $z = \nu/\nu_T$, with

$$\nu_T = 1.5T^2 \, (eB\sin\theta \, / \, 2\pi m_e c) , \qquad \text{(VI-6)}$$

the characteristic synchrotron frequency for electrons of energy $Tm_e c^2$, and θ the propagation angle relative to the magnetic field. The parameter τ_1 is the optical depth at $z = 1$ ($\nu = \nu_T$) and is given by

$$\tau_1 = 4.37 \times 10^{-10} \, nh \, / \, T^5 B , \qquad \text{(VI-7)}$$

where n is the electron density and h is the pathlength. The function I(z) is related to $I_1(z)$ in JH: $I(z) = I_1(z)/I_1(1)$. The normalized absorptivity for linearly polarized radiation, ζ_Q in Equation VI-4, is given in exact form by JH, but for our purposes the approximation

$$\zeta_Q \cong 0.62 \, z^{0.045} \qquad \text{(VI-8)}$$

will be sufficiently accurate.

An interesting feature of the relativistic Maxwellian spectrum is that its shape is determined by a single parameter, τ_1. Low values of τ_1 produce broad, gently curved spectra, while high values produce narrower spectra, as can be seen in Figure VI-1 where the spectral shapes are presented for various values of τ_1.

§3. Spectral Analysis

The data set.

Total flux density spectra will be derived from measurements at 4.8, 8.0, 14.5, and 87 or 90 GHz, and also 31 GHz data when available, for the sources discussed in Chapter V. It is particularly important that the data at all frequencies be simultaneous for the following analysis, since significant changes are seen in some sources on timescales of a few weeks or less, and such changes can seriously distort the broadband spectral shape.

Previous studies of broadband spectra in which the data are not strictly simultaneous may be biased by such effects. Therefore, spectra will be formed only if the measurements at all frequencies are within a week or two of each other. Occasionally exceptions will be taken to this policy by including 31 GHz measurements taken as much as a month before or after the other frequencies, but this will be done only if no significant variability is evident at 14.5 GHz during the period in question.

The model fitting procedure.

The spectra will be fit to the relativistic jet and Maxwellian

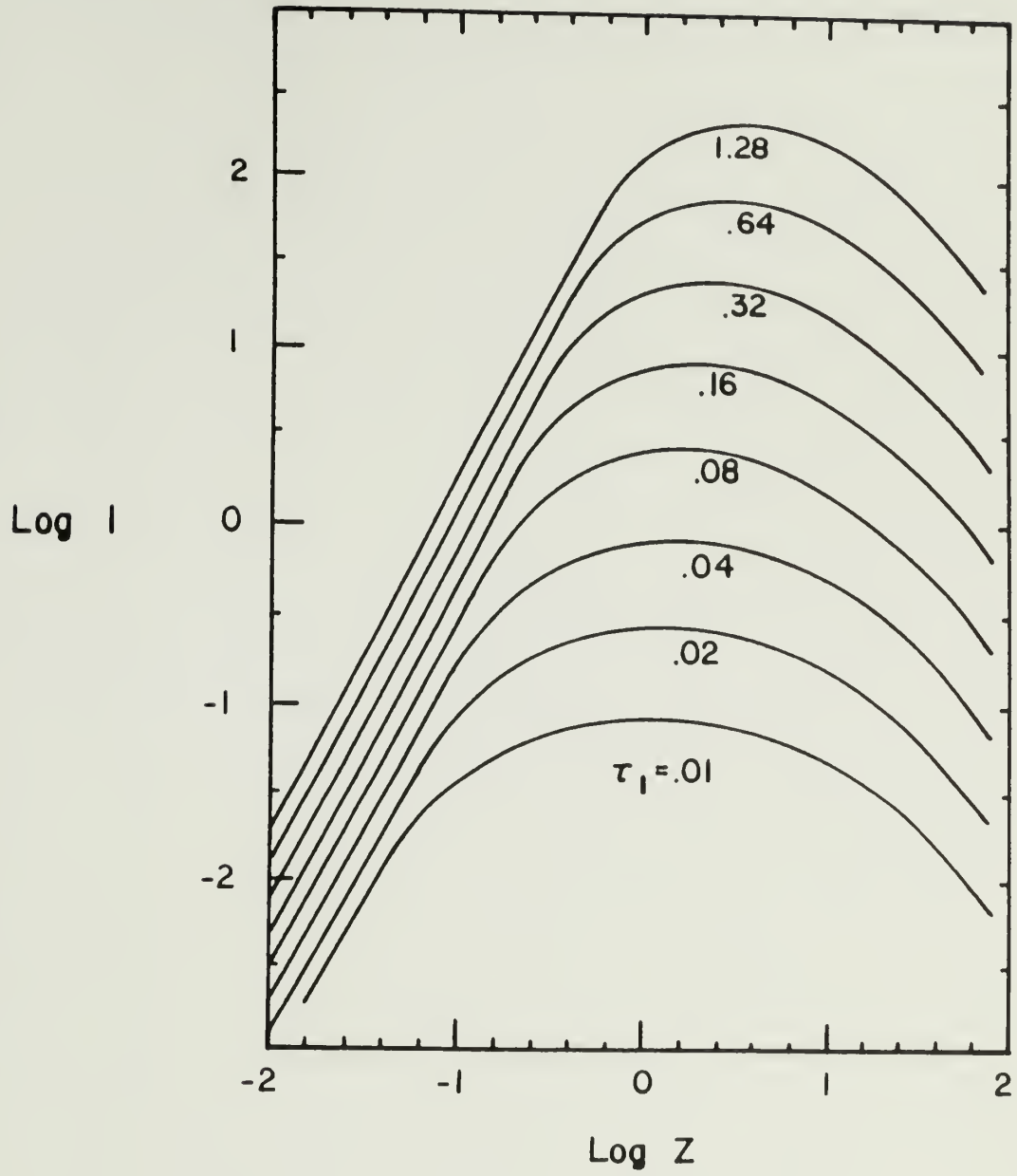

Fig.VI-1. Plot of spectral intensity, I, versus z, the frequency normalized by the characteristic frequency ν_T for electrons at temperture T, for different values of optical depth at $\nu = \nu_T$. The intensity units are arbitrary.

models following the procedure of Spangler (1980), who generated templates of the theoretical Maxwellian spectra which were then fit to the data by eye (a method known in some circles as "ocular estimation"). A least squares analysis is unnecessary for our purposes, and at any rate would be impractical in the present instance because of the function I(z) in the Maxwellian optical depth. This function consists of an integral over a hyperbolic Bessel function, and has no simple analytic form.

Two parameters of potential physical interest can be derived from the Maxwellian spectral fits. One is the characteristic synchrotron frequency of electrons with temperature T, $\nu_T \propto T^2B$. The other is the optical depth at this frequency, $\tau_1 \propto nh/BT^5$. Because the spectral shape changes rather slowly with τ_1 (Figure VI-1), there is considerable uncertainty in this parameter as derived from the spectral fits. In practice it was found that theoretical spectra with values of τ_1 a factor of two higher or lower than the "best fit" value are generally consistent (given the errors) with the observed spectra. Surprisingly, fits over this range of a factor of four in τ_1 do not significantly change the derived value of ν_T, and hence measurement of this parameter can be considered to be somewhat more accurate than that of τ_1.

The derived parameters of the jet model fits of interest here are the optically thin and thick spectral indices. These indices, as discussed above, can give information on the spatial distribution of particles and fields within the context of that model.

Results and discussion.

The results of the model fitting procedure are summarized in Table VI-1, which includes values for ν_T and τ_1 from the Maxwellian model, and α_{thk} and α_{thn} from the Konigl jet model for each source. The fits to the source spectra for both models are displayed in Figure VI-2. It is apparent from this figure that many sources can be fit extremely well by both models. No clear distinction can be made between them for these sources, which include NRA0150, 0J287, 1413+13, and BL Lac. Sources which are slightly better fit by the Maxwellian are 0235+164, and 3C345, and those slightly better fit by the power law jet model are 3C279, 1749+09, and 2145+06. The power law model gives clearly better fits to the spectra of 3C446 and 3C454.3, while 3C84 and 3C273 are rather poorly fit by both models. These last two sources are known to be complex in structure.

It is perhaps not surprising that the power law jet model gives excellent fits in many cases, since only five data points are being fit with a model requiring three parameters for specification. The Maxwellian requires only two parameters while still managing to fit many of the sources quite well.

In 0J287 and 0235+164 the optically thin spectral index in the power law fit is close to zero, or even slightly inverted. This may be inconsistent with optical and infrared data, a point discussed by Marsher (1977b), and Ennis, Neugebauer, and Werner (1982). The essence of the argument is that if $\alpha_{thn} \cong 0$ at 90 GHz, a lower limit to the synchrotron frequency characteristic of the high energy electron cutoff is about 10^{14} Hz. This leads to predicted infrared flux densities

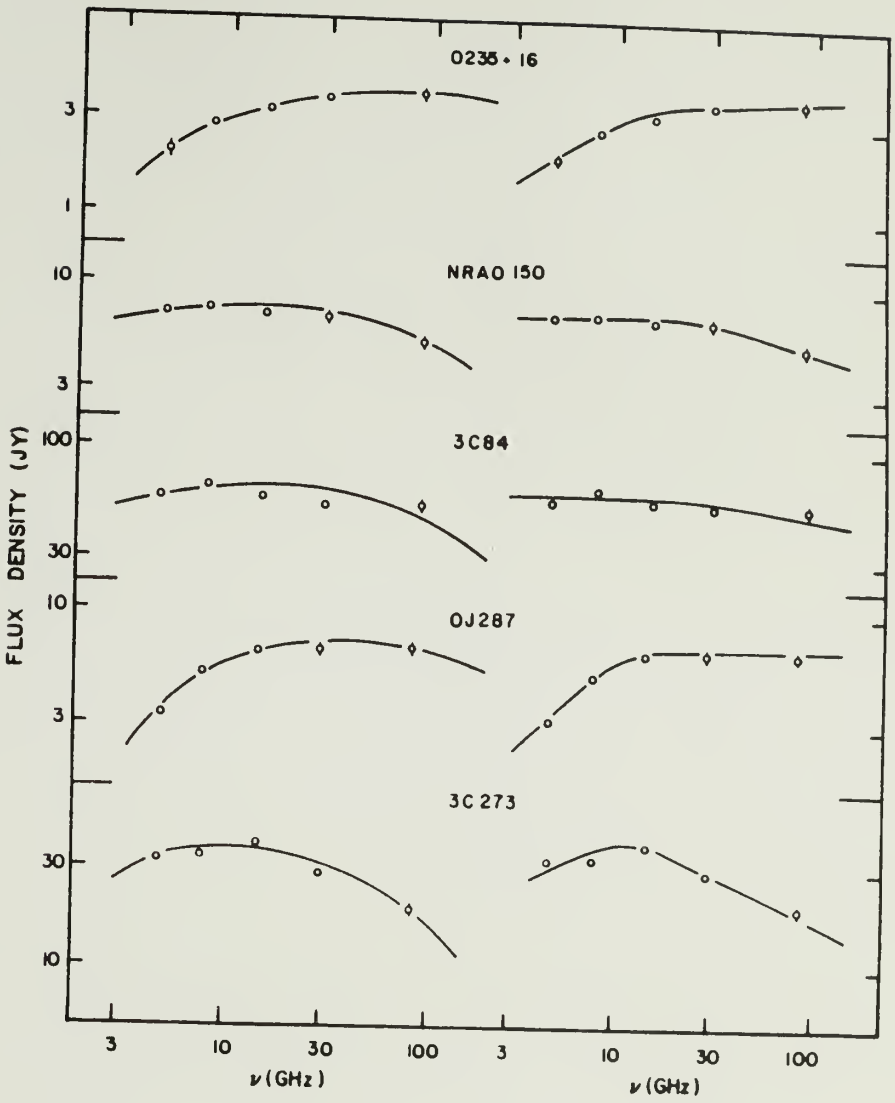

Fig.VI-2. Spectral fits to five frequencies for 13 sources. The same data are plotted on the left and right, and the solid curves are fits to a relativistic Maxwellian spectrum (left) and the inhomogeneous jet model with power law electrons (right). Parameters derived from the fits are given in Table VI-1. Continued on next two pages.

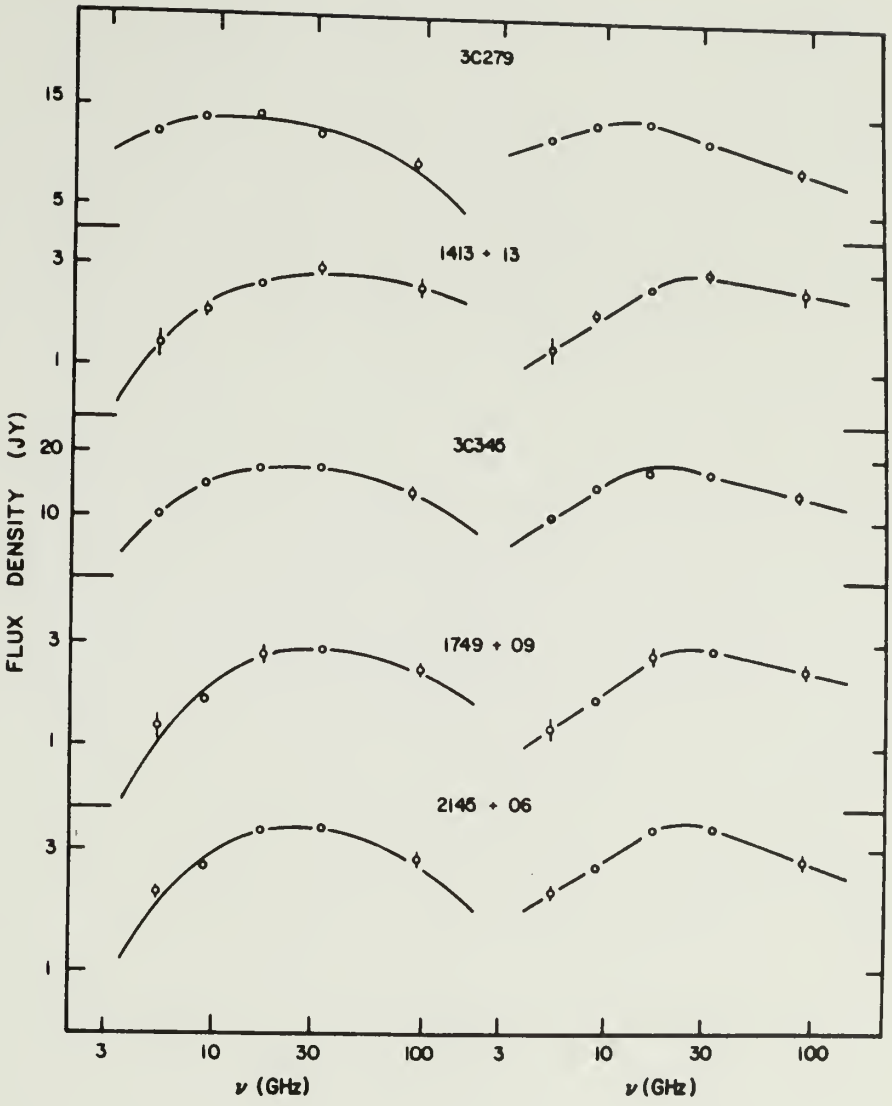
3C279
1413 + 13
3C345
1749 + 09
2145 + 06
FLUX DENSITY (JY)
15
5
3
1
20
10
3
1
3
1
3
10
30
100
ν (GHz)

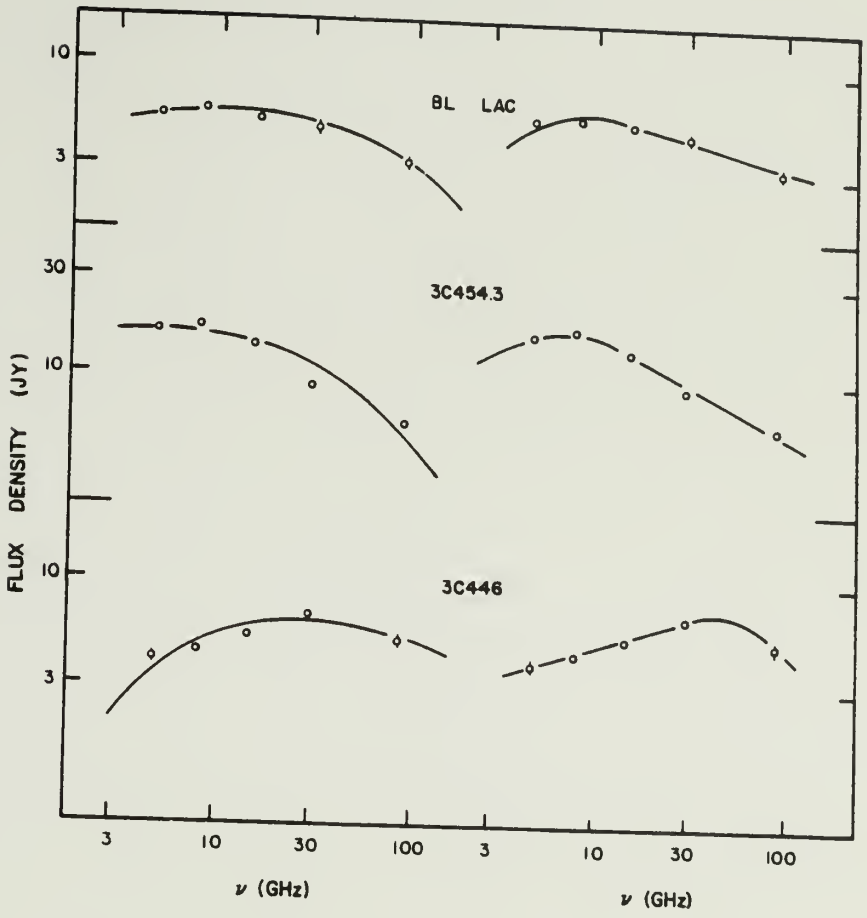
BL LAC
3C454.3
3C446
FLUX DENSITY (JY)
10
3
30
10
10
3
3
10
30
100
3
10
30
100
ν (GHz)
ν (GHz)

Table VI-1. Parameters Derived from Spectral Fits

Source	Date	ν_T(GHz)	τ_1	α_{thn}	α_{thk}
0235+164	1981.92	54	.005	+.10	.61
NRAO150	1982.54	11	.001	-.27	.00
3C84	1982.54	13	.001	?	?
0J287	1981.91	24	.08	.00	.90
3C273	1982.10	8	.08	-.43	?
3C279	1982.03	7	.08	-.30	.32
1413+13	1982.53	22	.08	-.17	.64
3C345	1981.91	14	.16	-.24	.63
1749+09	1982.53	12	.32	-.17	.64
2145+06	1982.53	8	.64	-.36	.60
BL Lac	1981.92	7	.002	-.25	?
3C446	1982.53	16	.08	?	.30
3C454.3	1982.53	3	.08	-.50	?

which are an order of magnitude or more higher than those observed. Though we do not have simultaneous infrared data for these sources, previous measurements (see Jones et al. 1981) indicate that, barring uncharacteristically large infrared flares, the transparent index $\alpha_{thn} = 0$ may be untenable. If the high frequency spectral index is due to partial opacity, we would expect a sharper falloff in the flux density at low frequencies than that which is seen. These considerations would tend to favor the Maxwellian model for 0235+164 and 0J287, but are hardly definitive.

In assessing the physical significance of the power law indices derived from the Konigl jet model, it is helpful to plot α_{thk} versus α_{thn} for each source together with curves predicted by the model for various values of k and b. This is done in Figure VI-3, where the solid curves represent the predicted behavior of the indices for various integer combinations (k,b). Estimated uncertainties in both indices are $\pm 0.1 - 0.2$. The combinations are as indicated in the figure, and it can be seen that five sources (0235+164, 1413+13, 3C345, 1749+09, 2145+06) lie very close to the (2,2) curve. Given the uncertainties, these sources are probably also consistent with the (1,3) curve, but physical considerations tend to favor the (2,2) combination. The values k=2 and b=2 are expected from a freely expanding relativistic jet in which the component of the field parallel to the jet axis dominates (see e.g., Blandford and Rees 1974). These values are also expected from a non-relativistic wind with a frozen-in field (this would be more appropriate to the Marscher 1977a tapered source model; see Spangler 1980). The (1,3) combination is not predicted by any of

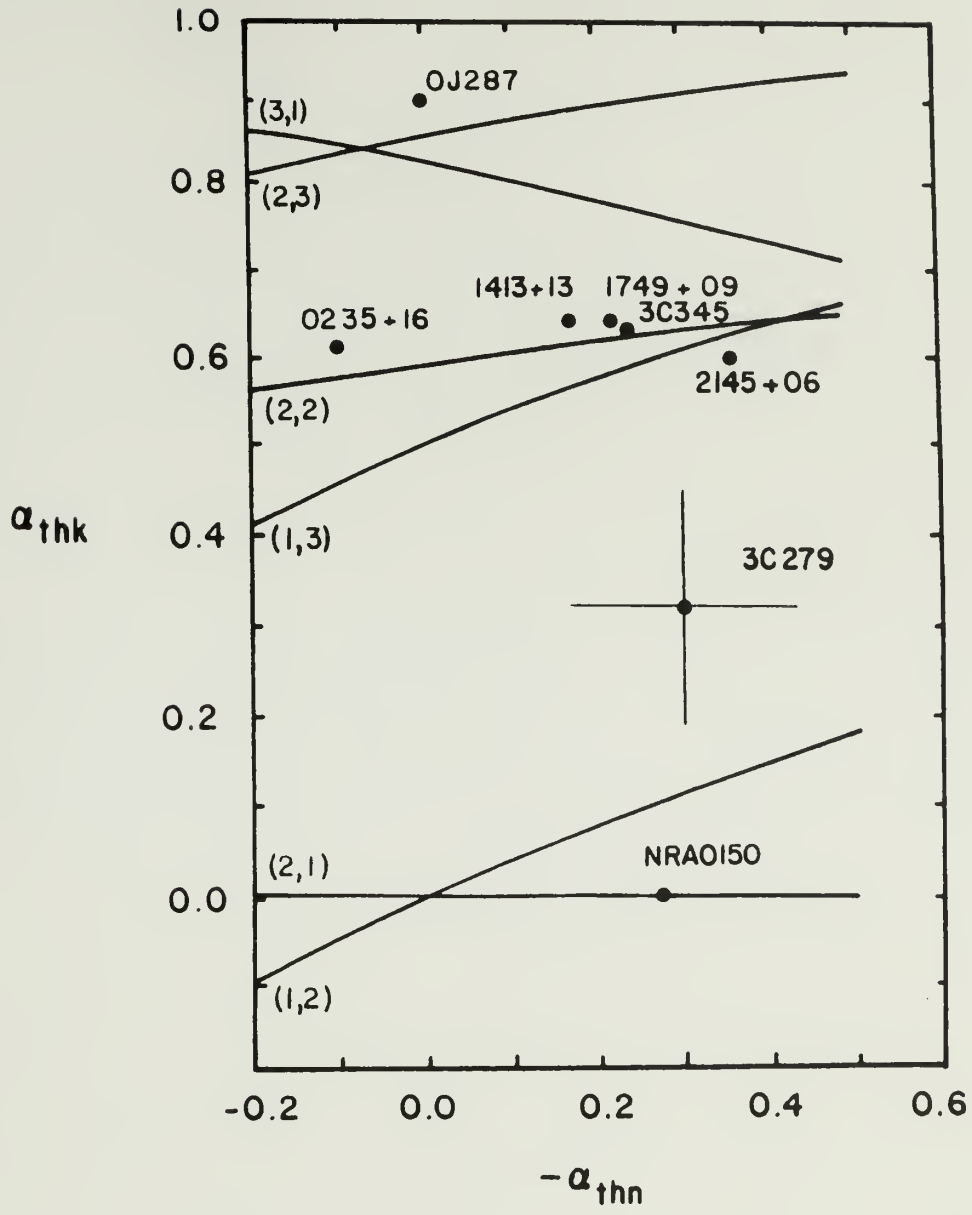

Fig.VI-3. Plot of optically thick versus optically thin spectral indices for 8 sources in which both indices could be determined. The solid curves are predictions of the relativistic jet model of Konigl (1981), for different integer combnations (m,n), as described in the text. Typical estimated error bars are shown for 3C279.

the wind or magnetic dipole models considered by Spangler in a similar context.

One source, NRAO150, falls on the (2,1) curve, and this combination would be expected from a free jet in which the perpendicular field component dominates, or from a wind with a turbulently generated field. OJ287 is consistent with the (2,3) or (3,1) curves, but these combinations are not predicted by any jet model known to the author. A final source, 3C279, does not lie close to any of the curves, at least not those plotted here for integer values of k and b.

The Maxwellian parameters ν_T and τ_1 alone provide little information on physical conditions within the sources, at least on the basis of spectra which are considered at only a single epoch or which are non-variable. They involve at least four physical parameters (B, T, n, and h) and perhaps a fifth (the relativistic Doppler factor if the source is moving at speeds close to that of light). However, we shall see later that the Maxwellian spectral evolution can be used to derive model dependent values for k and b, albeit in a somewhat different context than that discussed above.

In fitting spectra to idealized models we must acknowledge the fact that real sources must invariably be complex to some degree; this is true to the extent that the observed spectrum is never the pure reflection of a single component, be it smoothly non-uniform or homogeneous. This is evident at or below frequencies of a few gigaHertz, where the flux density is often dominated by an extended component with an optically thin power law spectrum. Other complicating effects are the superposition of radiation associated with different outbursts, and

underlying constant components. Outbursts are often seen to overlap, causing unassessable distortion of the spectrum. It seems clear that evaluation of the intrinsic spectrum and its evolution with time will be best accomplished for cases in which the source is undergoing a large, isolated outburst, which rises from and then returns to some low base level.

A few such cases are to be found in the data set, including 3C345, 3C454.3, and 0235+164. These would appear to be the best candidates for examining spectral evolution with time. For 3C345, the flux was at the peak of a large outburst that began in 1978, but the period covered by the observations available here was too short to show significant evolution. In 3C454.3, the spectral turnover evolved toward lower frequencies with time, and the optically thin power law index remained constant at a value of about -0.5. This result is qualitatively consistent with the predictions of the standard adiabatic expansion model with power law electrons. The best example of a large, isolated outburst with a low base level is to be found in the case of 0235+164. This source will be singled out for detailed discussion of its spectral evolution in the next section.

§4. A Blast Wave Model and the Spectral Evolution of 0235+164

In this section we will discuss total flux density variations in the BL Lac object 0235+164, and present calculations wherein the full analytic expression for the radiation spectrum of a relativistic Maxwellian particle distribution is included in the blast wave model of Blandford and Mckee (1976 and 1977, hereafter BMI and BMII). In BMII the relativistic Maxwellian spectrum was analysed in the optically thick and thin limits, wherein it was assumed that the spectrum rises as $\nu^{1/3}$ when the source is transparent. This is true over a limited spectral region, but we can see from Figure VI-1 that the spectrum eventually turns over and declines precipitously at high frequencies. The breadth of the $\nu^{1/3}$ regime depends on the optical depth at the characteristic frequency ν_T. Here we develop expressions which describe the variations of flux density as a function of time and frequency for a blast wave with a Maxwellian spectrum, and apply these expressions to variations observed in 0235+164. Although this model does not give a fully satisfactory account of the behavior of 0235+164, it does explain some aspects of the 1981-82 outburst. Rather than having the model stand or fall on the basis of this particular example, we present the calculations in the spirit of providing a framework within which other sources might be analysed in the future.

We have chosen 0235+164 for closer scrutiny because of three factors which, taken as a whole, make this source unique among those studied here:

1. The source was undergoing a rapid, isolated outburst (as can be seen in Figure VI-4, ignoring for the moment the solid curves).

2. The spectral shape varied considerably during the observations.

3. The spectrum (shown in Figure VI-2a) is extremely well fit by the Maxwellian model and, for reasons discussed above, may be inconsistent with a power law model.

We have fit the spectrum to a relativistic Maxwellian at five epochs, and values for ν_T and τ_1 have been derived for each (the first was fit to five frequencies, the rest to four - 31 GHz data were not available at the later times).

In Figure VI-4 flux densities are plotted versus time at 4.8, 8.0, 14.5 GHz (lower panel), and at 87-90 GHz (upper panel), together with a model fit to be discussed below. It appears that the outburst began in late June or early July of 1981, and we will take July 1 as the start of the burst. Then the behavior of ν_T and τ_1 as a function of time t_o after July 1 can be examined. The evolution of ν_T is shown in Figure VI-5, where it can be seen that this parameter closely follows a power law with time; the error bars represent the approximate range over which the spectral fits were acceptable. A least squares fit yields $\nu_T \propto t_o^{-2.2\pm0.2}$, where the error in the exponent is based upon the scatter of the points about the best fit line. The evolution of τ_1 is shown in Figure VI-6, where the error bars are estimated and are intended to reflect the rather large uncertainties in fitting this parameter noted earlier. A power law fit gives $\tau_1 \propto t_o^{1.1\pm0.5}$ with the

Fig.VI-4. Total flux density variability of 0235+164 for 1981-82, at four frequencies. Data in lower panel are from University of Michigan Radio Astronomy Observatory. Solid curves are blast wave model fit, as discussed in the text.

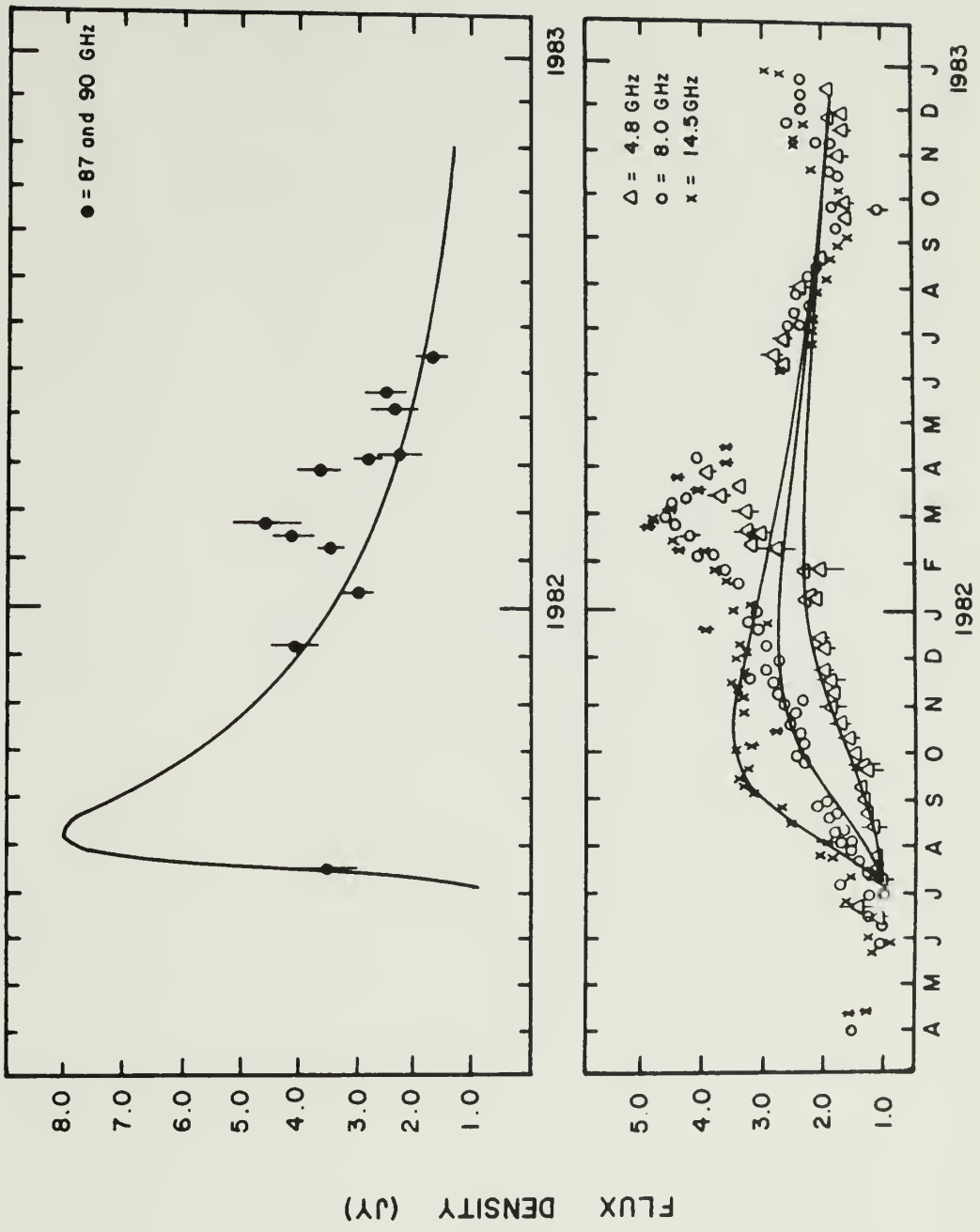
● = 87 and 90 GHz
△ = 4.8 GHz
o = 8.0 GHz
x = 14.5GHz
1982
1983
A M J J A S O N D J F M A M J J A S O N D J
8.0
7.0
6.0
5.0
4.0
3.0
2.0
1.0
FLUX DENSITY (Jy)
TIME (MONTHS)

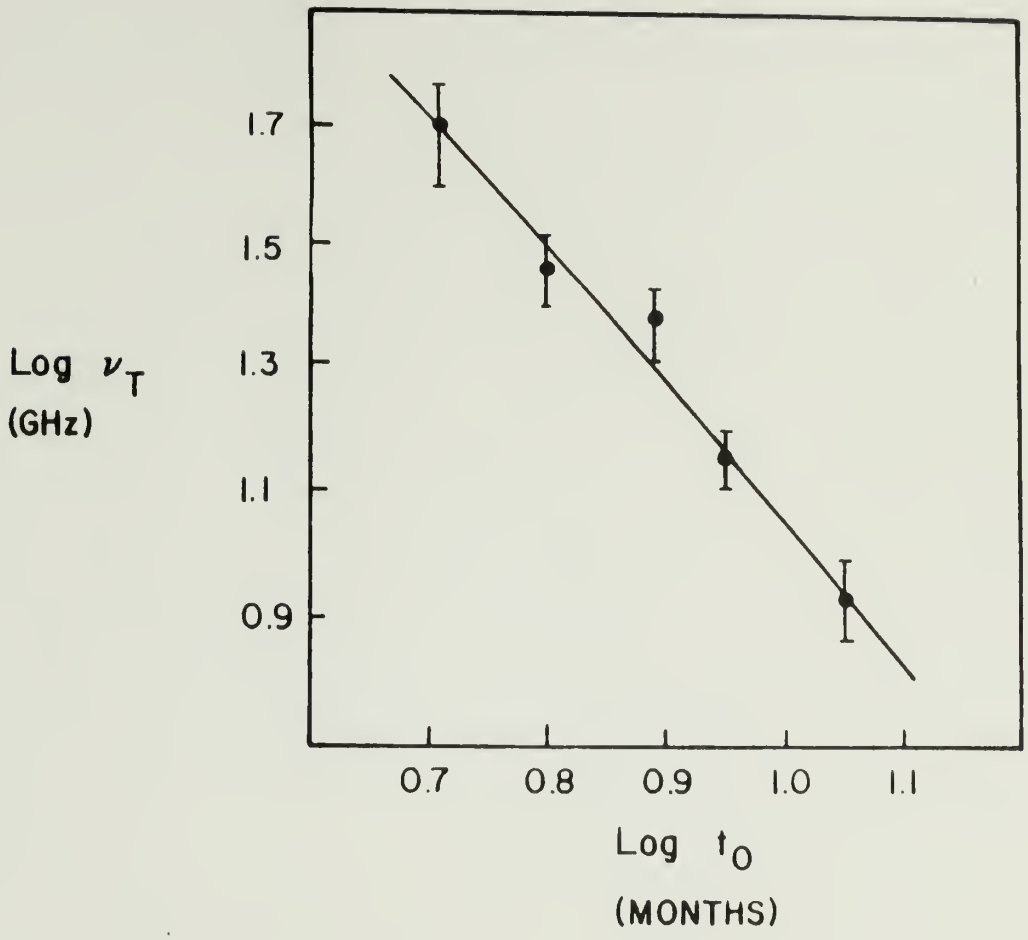

Fig.VI-5. Variation of the characteristic frequency ν_T with time, derived from relativistic Maxwellian spectral fits to the data presented in Fig.VI-4. Errors on the data points represent the estimated range over which the fits were acceptable. Solid line is least squares fit to a power law, yielding $\nu_T \propto t_o^{-2.2\pm0.2}$.

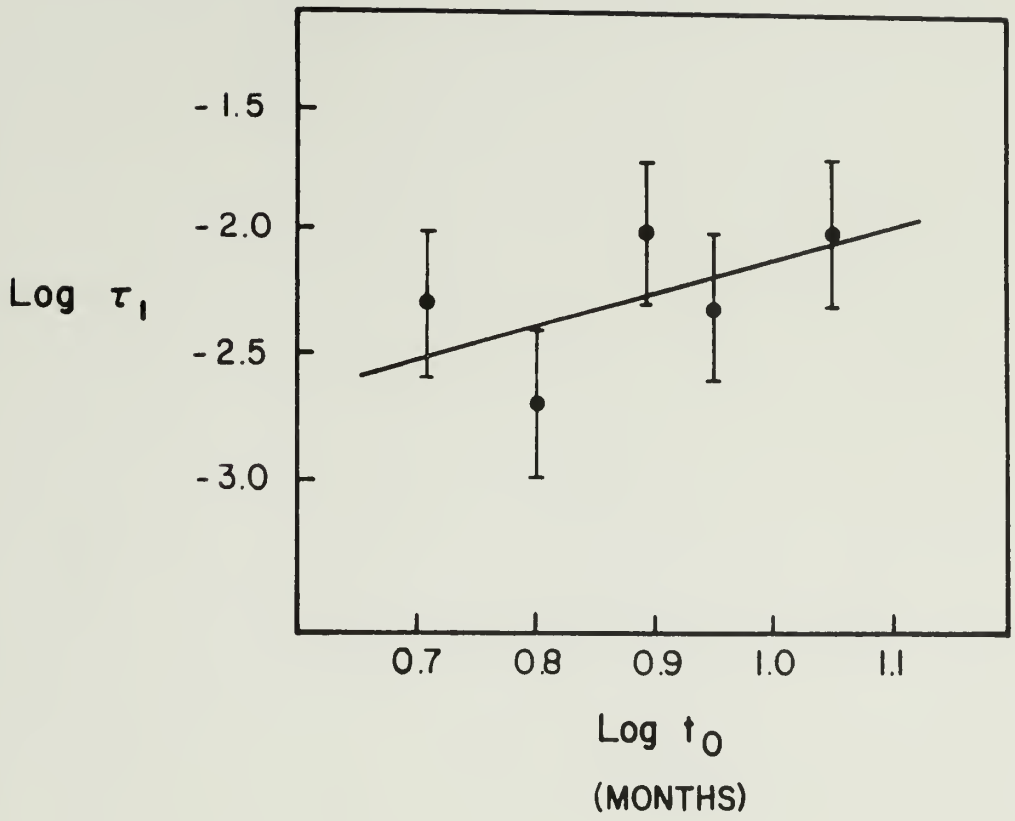

Fig.VI-6. Same as above for variation of τ_1, the optical depth at frequency ν_T. Error bars reflect estimated factor of 2 uncertainty about the "best fit" value. The solid line is from a least squares fit, giving $\tau_1 \propto t_o^{1.1\pm0.5}$. The error in the exponent is from the scatter about the best fit line; using the uncertainties on the data, the exponent error is ±1.1.

exponent error again based on the scatter of the points, but given the error bars τ_1 could also be fit by a line of zero slope.

It has been suggested that a relativistic blast wave might generate a Maxwellian particle distribution (e.g., JH), so this model seems an attractive choice to explain the Maxwellian spectral shape and the variations of ν_T and τ_1. The blast wave model, as developed in BMI and II, is quite comprehensive and only the essential details will be outlined here.

A large supply of energy is assumed to originate from a central source, either impulsively or by steady injection. This gives rise to a relativistically expanding shock with bulk Lorentz factor $\Gamma = (1 - \beta^2)^{-1/2}$, where $\beta = v/c$. At the shock front, particles swept up from the ambient medium are accelerated. The characteristic thickness of the shock (the region in which particles are maintained at high energies) is (BMI)

$$h \cong R/\Gamma^2 , \qquad \text{(VI-9)}$$

in the stationary observer's frame, and in the shock frame

$$h_s \cong R/\Gamma , \qquad \text{(VI-10)}$$

where R is the radius of the shock from the central source; the subscript s will denote quantities measured in a frame moving with the shock. The shock radius is given by (BMI)

$$R = k_o \Gamma^2 \beta c t_o , \qquad \text{(VI-11)}$$

where k_o is a constant that depends on redshift and t_o is time measured

by the observer (the constant k_o and other k constants to follow are dimensionless; they are defined in BMII).

A similarity solution for the shock Lorentz factor gives (BMII)

$$\Gamma^2 \propto t_o^{-m/(m+1)}, \qquad \text{(VI-12)}$$

where m depends on the variation of density with radius in the ambient medium, and whether the energy supply is impulsive or steady. In what follows we shall assume that the shock is extremely relativistic (ER). For an ER impulsive shock into a uniform medium, m = 3 (where the density of the ambient medium is $n_a \propto R^{-k}$, with k = 0 in this case). For an ER impulsive shock into a "wind", m = 1 (k = 2). In the analogous cases for a steady injection shock, m = 1 (k = 0) or m = 0 (k = 2). Other values of m are allowed, depending on the value of k.

The density behind the shock is (BMI)

$$n_s = 2.8\ \Gamma\ n_a = 2.8\ \Gamma\ n_{a1}\ r^{-k}, \qquad \text{(VI-13)}$$

where $r = R/R_1$. The subscript 1 will denote quantities evaluated at some reference time $t_o = t_{o1}$ after the start of the outburst. Thus, R_1 and n_{a1} are the shock radius and ambient density at time t_{o1}. The electron temperature (in units of $m_e c^2/k$) behind the shock is (BMII)

$$T_s = 1/3\ k_e\ k_\gamma\ \Gamma\ \beta^2\ (m/m_e), \qquad \text{(VI-14)}$$

where m is the mean mass per particle, which will be taken (following BMII) to be 1.95×10^{-24} g corresponding to He/H = 0.1 by number. The parameter k_e is the fraction of particle energy behind the shock that goes into the electrons, and $k_\gamma = .71\ k_w$, where k_w is the ratio of

particle enthalpy to rest energy density in the ambient medium. The post-shock magnetic field is given by (BMII)

$$B_s = 2.8\ \Gamma\ B_a = 2.8\ \Gamma\ \ B_{a1}\ r^{-b}. \qquad \text{(VI-15)}$$

The Maxwellian spectral parameters ν_{Ts} and τ_{1s} in the shock frame are then given by Equations VI-6 and 7 with $B = B_s$, $T = T_s$, etc.

The transformation of these quantities to the observer's frame is accomplished using

$$\nu_T = \delta\ \nu_{Ts} \cong k_\nu \Gamma\ \nu_{Ts} \qquad \text{(VI-16)}$$

$$\tau_1 = \delta^{-1}\ \tau_{1s} \cong k_\nu^{-1}\ \Gamma^{-1}\ \tau_{1s} \qquad \text{(VI-17)}$$

where $\delta \cong k_\nu \Gamma$ is the Doppler factor of the shock with a redshift correction included in k_ν (see BMII and Ozernoi and Sazonov 1969). We then obtain

$$\nu_T = 2.4\text{x}10^{13}\ \left(k_e^2\ k_\gamma^2\ k_\nu\ \sin\theta\right)\ \Gamma^4\ \beta^4\ B_{a1}\ \ r^{-b}\ \ \text{Hz}, \qquad \text{(VI-18)}$$

$$\tau_1 = 5.9\text{x}10^{-25}\ \left(k_e^5\ k_\gamma^5\ k_\nu\ \sin\theta\right)^{-1}\ x$$

$$n_{a1}\ B_{a1}^{-1}\ R_1\ \Gamma^{-7}\ \beta^{-10}\ r^{1+b-k}. \qquad \text{(VI-19)}$$

Next we will derive the dependence of the flux density on time and frequency. Assuming a simple cylindrical geometry for the observable radiating region, the observed flux is just

$$S_\nu = \Omega\ I_\nu, \qquad \text{(VI-20)}$$

where Ω is the solid angle subtended by the source. For a spherical ER blast wave, only a small area of the source is seen due to forward

Doppler boosting, justifying the use of cylindrical geometry. The angular radius seen by a distant observer is given in BMII as

$$\Theta = k_\theta R \; / \; \Gamma D_L, \tag{VI-21}$$

where D_L is the luminosity distance, and k_θ depends on m and redshift.

The source solid angle is then

$$\Omega = \pi\Theta^2 = \pi k_\theta{}^2 \, R^2 / \, \Gamma^2 D_L{}^2. \tag{VI-22}$$

For the relativistic Maxwellian, the spectral intensity in the shock frame will be taken to be

$$I_{\nu s} = 2 m_e T_s \, \nu_s{}^2 \left(1 - e^{-\tau \nu s}\right). \tag{VI-23}$$

This is similar to Equation VI-3, except that the factor $\cosh(\zeta_Q \tau_\nu)$ has been dropped for simplicity since numerical experiments show that this factor has little effect on the spectral shape. Transforming to the observer's frame,

$$I_\nu \;\; = \;\; \delta^3 \, 2 m_e T_s (\delta^{-1}\nu)^2 \left(1 - e^{-\tau}\nu\right), \tag{VI-24}$$

where the factor δ^3 is due to Doppler enhancement and $\delta^{-1}\nu = \nu_s$ is the transformed frequency (see Ozernoi and Sazonov 1969). The optical depth is

$$\tau_\nu = \tau_1 \, z^{-2} \, I(z). \tag{VI-25}$$

Here $z = \nu/\nu_T$, with ν_T given by Equation 18, and τ_1 is given by Equation VI-19. Finally, using Equations VI-14, 20, 22, 24 and 25 the

observed flux density is

$$S_\nu = .41\, k_\nu k_e k_\gamma k_\theta^2\, k_o^2\, c^2\, D_L^{-2}\, \Gamma^4\, \beta^4\, t_o^2\, \nu^2 \times \{1 - \exp(-\tau_1 z^{-2}\, I(z))\} \quad \text{Jy} . \qquad \text{(VI-26)}$$

The time dependences of ν_T and τ_1 are contained implicitly in Equations VI-18 and 19 in the variables Γ, r and β. Since we are considering the ER case, $\beta \cong 1$ and its small variation with time can be ignored for the time being without appreciable error. Then with Γ given by Equation VI-12 and $r \propto t_o^{1-m/(m+1)}$, the time dependence in Equations VI-18 and 19 can be written explicitly as

$$\nu_T \propto t_o^{\alpha_1}, \qquad \text{(VI-27)}$$

$$\tau_1 \propto t_o^{\alpha_2}, \qquad \text{(VI-28)}$$

where $\alpha_1 = (b-2)\, m/(m+1) - b$ and

$\alpha_2 = (2.5-b+k)\, m/(m+1) + (b-k) + 1.$

The observed variations of these quantities in 0235+164 are roughly $\nu_T \propto t_o^{-2}$ and $\tau_1 \propto t$, where the latter is not demanded by the data but is, at any rate, that given by the best power law fit. The variation of ν_T is predicted by Equation VI-27 if b = 2, independent of the value of m. The variation of τ_1 is accounted for if the shock is powered by steady injection and if it propagates into a wind-like density distribution. Then m = 0, k = 2, and with b = 2, we find $\alpha_2 = 1$.

With m = 0, Γ (and β) will be constant with time, which also implies that the shock is isothermal. This is because the steady power

supplied by the central source is just counterbalanced by the constant rate of sweeping up and acceleration of particles at the shock front. Having chosen values for m, b, and k based on the observed variations in ν_T and τ_1, we can evaluate the k constants (assuming an ER shock) with the exception of k_γ and k_e. The first depends on whether the ambient medium itself is relativistic. We will assume that it is not. The second is the fraction of the particle kinetic energy behind the shock that goes into the electrons. This fraction is unknown (although it is assumed to be 0.5 in BMII), but we will restrict its value below. The k constants are then $k_\gamma = 0.71$, $k_o = 2(1+Z)^{-1}$, $k_\theta = (1+Z)^2/2$, and $k_\nu = 1.4/(1+Z)$, with Z the redshift.

It is now possible to write out explicitly, for the model we are considering, the expressions derived above. Measuring time in months (t_{o1} = 1 month),

$$\nu_T = 1.1 \times 10^{12} (1+Z)^{-1} k_e^2 \Gamma^4 \beta^4 B_{a1} \sin\theta \; t_{om}^{-2}$$
$$\equiv \nu_{T1} \; t_{om}^{-2} \qquad \text{(VI-29)}$$

$$\tau_1 = 3.0 \times 10^{-22} (1+Z) k_e^{-5} n_{a1} (B_{a1} \sin\theta)^{-1} R_1 \Gamma^{-7} \beta^{-10} \; t_{om}$$
$$\equiv \tau_{11} \; t_{om}. \qquad \text{(VI-30)}$$

From the fits to the spectral parameters shown in Figures VI-5 and 6, we obtain the empirical values $\nu_{T1} \cong 1700$ GHz and $\tau_{11} \sim .001$.

Equation (26) becomes

$$S_\nu \cong 2.6 \times 10^{-22} \left((1+Z)/D_{L9}^2 \right) k_e \Gamma^4 \beta^4 \; t_{om}^2 \; \nu^2$$
$$\times \left\{ 1 - \exp\left(-\tau_{11} \; t_{om}^{-3} \; z_1^{-2} \; I(z_1 \; t_{om}^{-2}) \right) \right\} \text{ jy} \qquad \text{(VI-31)}$$

where $z_1 = \nu/\nu_{T1}$ and D_{L9} is the distance in gigaparsecs. This expression gives a good fit (the solid lines in Figure VI-4) to the early opaque and partially opaque variations of the flux density if $\nu_{T1} = 1700$, $\tau_{11} = .002$, and if

$$2.6 \times 10^{-22} \left((1+Z)/D_{L9}^2\right) k_e \Gamma^4 \beta^4 = 3 \times 10^{-21} . \quad \text{(VI-32)}$$

where the left side is from Equation VI-31 and the right side is from the empirical fit to the early flux density variations.

The value of ν_{T1} used in the fit is the same as that given by the later spectral variations, and that of τ_{11} is roughly consistent with the later variations (given the rather large uncertainties in the measurement of τ_1).

The redshift of 0235+164 is $Z = .852$, and with $H_o = 75$ km s^{-1} Mpc^{-1} and $q_o = 0.5$ the luminosity distance is $D_{L9} = 4.0$ Gpc. Then from Equation VI-32, $\Gamma\beta = 3.2\ k_e^{-1/4}$. For $k_e = 0.5$, as assumed in BMII, $\Gamma = 3.9$ and $\beta = .97$. However, from Equation VI-14, these values produce an excessively high electron temperature, $T_s = 5 \times 10^{12}$ K, behind the shock. This is a problem because for a Maxwellian the optically thick brightness temperature in the shock frame equals the physical temperature, which in this case exceeds the well known limit of 10^{12} K beyond which inverse Compton losses dominate the electron energetics. In order to avoid catastrophic Compton losses at early times when the radiation density is high, we need $T_s \leq 10^{12}$ K. If we enforce the condition that $T_s = 10^{12}$ K, then Equations VI-32 and 14 can be simultaneously satisfied if $k_e = .06$, $\Gamma = 6.5$, and $\beta = .987$. According to Burbidge, Jones, and O'Dell (1974), it is generally assumed that

$k_e > .01$, although it could be as small as the ratio m_e/m_p, so adopting the value $k_e = .06$ does not appear to be unreasonable. The other physical parameters of the shock and ambient medium can then be calculated from Equations 11, 29, and 30, with $\nu_{T1} = 1700$ GHz, $\tau_{11} = .002$, and $k_e = .06$:

$$\Gamma \cong 6.5$$

$$T_s \cong 1 \times 10^{12} \text{ K (assumed)}$$

$$R_1 \cong 1 \text{ pc}$$

$$n_{a1} \cong 1 \text{ cm}^{-3}$$

$$B_{a1} \cong 0.1/\sin\theta \text{ G} .$$

The approximate dependences of these quantities on the electron energy fraction k_e are $T_s \alpha\ k_e^{.75}$, $\Gamma \alpha\ k_e^{-.25}$, $R_1 \alpha\ k_e^{-.5}$, $n_{a1} \alpha\ k_e^{2.75}$, and $B_{a1} \alpha\ k_e^{-1.0}$.

The luminosity of injection from the central source can also be calculated, assuming the shock is spherically symmetric, using Equation (2) in BMII,

$$L_I t = k_\sigma\ w_1\ \Gamma^4\ \beta^2\ (4/3\ \pi R^3) \qquad \text{(VI-33)}$$

where w_1 is the relativistic enthalpy ahead of the shock ($w_1 \cong n_a mc^2$ for a non-relativistic medium). We find that $L_I \cong 2\times10^{49}\ (k_e/.06)^{.75}$ erg s^{-1}. The outburst considered here was observed to last for about one year, but since the timescale in the observer's frame is compressed by a factor $\sim 2\Gamma^2/(1+Z)$ (due to relativistic kinematic effects), in fact it lasted about 40 years. Then the total energy of the outburst is $E \sim 2\times10^{58}\ (k_e/.06)^{.25}$ erg. These rather large energy requirements could be reduced if the shock is not spherically symmetric. This

probably would not seriously affect the basic physics (see BMII), and could reduce L_I and E by a factor of 100 if the shock is confined to a jet with $\Omega_{jet}/4\pi \sim 10^{-2}$, a value typical of observed radio jets. In that case, the jet would have to be pointed directly toward us, a seemingly unlikely situation. However, only a small fraction of optical quasars are radio-loud, and statistics bear out the argument that radio emission is seen only from those sources which are preferentially oriented along our line of sight (e.g., Kellerman and Pauliny-Toth 1981 and references therein). Thus, if 0235+164 does have a jet-like geometry, its radio emission is seen because it is among the minority of sources which happen to be oriented toward us, a situation similar to that encountered in the lighthouse model for pulsars.

Discussion.

In Figure VI-4, note that at early times, especially when the source is opaque or partially opaque at a given frequency, the model fits the data well. However, the level of the total flux density begins to deviate considerably from the model during December 1981 - January 1982 (depending on frequency), even though the spectral shapes at this time and later remain consistent with that predicted by the model. Indeed, the variations in spectral shape at these times were used to derive the parameters of the model which correctly predict the early variations in the flux density. If the model developed here is in fact appropriate for this outburst, we must conclude that at the end of 1981 the blast wave encountered conditions that deviated from the idealized case treated here. At this time, for example, the shock may have reached a

radius where the ambient density deviated from a smooth R^{-2} variation. This could result in a speedup or slowdown of the shock, changing Γ and consequently the factor by which the flux was Doppler boosted. The detailed effects of such deviations on other model parameters are difficult to evaluate, given the idealized similarity treatment in BMI. If the shock was propagating down a jet, with its axis close to the line of sight, curvature or kinks in the jet could also change the flux density level, as the forward boosted beam changed its angle to the line of sight.

The values for physical parameters of the shock and ambient medium calculated above should be considered only approximate, the major uncertainty being the shock temperature and the corresponding value of k_e. Some quantities (most notably n_a) are rather strongly dependent on k_e, while the shock Lorentz factor and the total energy of the outburst depend on k_e to only the .25 power. The purpose of the foregoing analysis is to demonstrate that the blast wave model with a Maxwellian particle distribution can explain some aspects of the variations in 0235+16, while predicting reasonable physical conditions in the inner few parsecs near the energy source. The values of n_a and B_a are well within the range predicted by Burbidge, Jones & Odell (1974) for a number of sources based upon non-relativistic models with power law electrons. The total energy requirements of the outburst are also lower than predicted by them for several sources.

This is not to imply, however, that the energy requirements for a spherical blast wave are not still large, providing an argument in favor of collimation along the line of sight. If we assume that the

injected energy was collimated in a jet with $\Omega_{jet}/4\pi \cong 10^{-2}$, then the total energy of the outburst was $\sim 2\times10^{56}$ erg, with $L_I \sim 2\times10^{47}$ erg s^{-1}. If the energy is supplied by accretion onto a supermassive object,

$$L_I \sim 10^{47} \dot{M} \text{ ergs } s^{-1}, \qquad \text{(VI-34)}$$

where $\dot{M}$ is the accretion rate in solar masses per year (Equations VI-34 and 35 are from Pacini & Salvati 1981). Thus the outburst in 0235+16, if collimated, would require an accretion rate of about two solar masses per year.

For electrodynamic models (e.g., spinars)

$$L_I \sim 10^{47} (R/10^{16}\text{cm}\ \ B/100\text{G})^2 \text{ ergs } s^{-1}, \qquad \text{(VI-35)}$$

where R is the size of the region containing a strong field B. In this case R or B need only be slightly larger than 10^{16} cm or 100 G respectively.

In addition to reducing energy requirements, another point in favor of collimation is the following. If the blast wave were spherically symmetric, the entire medium surrounding the central source would be disrupted during each outburst. Since outbursts occur every few years or few decades, it would be difficult to see how the medium could recover so rapidly. On the other hand, if the damage is confined to a narrow cone, only a small fraction of the medium is disrupted and the cone can be refilled between outbursts.

The subject of this study, 0235+164, is one of the most active and interesting extragalactic objects known. During an outburst in 1975 the implied brightness temperature (from light travel time arguments)

was 10^{15} K, one of the highest ever observed at centimeter wavelengths (Ledden, Aller, and Dent 1976), and it was also the first source in which linear rotation of polarization position angle with time was seen (Ledden and Aller 1979). It has already been discussed in terms of relativistic blast wave models by Blandford and Rees (1978) and Marscher (1978). Marscher proposed a blast wave impinging upon a screen at a distance of about 20 parsecs to explain the 1975 outburst, in a model which assumed a power law electron distribution. His total energy for the outburst of about 3×10^{57} erg is comparable to or greater than that found here, depending on if the shock is collimated. The main differences between that model and the one proposed in this chapter are that here we assume a continuous medium and a Maxwellian particle distribution, the latter assumption being motivated by the systematic variations of the source spectrum when fit to the Maxwellian spectral shape. Although in general the blast wave model has been discussed somewhat less in recent years, it appears capable of explaining several aspects of the 1981-82 outburst in 0235+164.

§5. Conclusion

In this chapter, in contrast to those previous, we have concentrated on total flux density rather than polarization. Extragalactic source spectra have been analyzed on the basis of two current models of broadband spectral shapes. It was found that the relativistic Maxwellian and inhomogeneous source models both give acceptable fits to the observed spectra in many sources. Two out of thirteen sources were clearly better fit by the latter, but two others may be inconsistent

with the inhomogeneous power law electron model because in these cases it predicts excessively large flux densities in the infrared. It would appear that the data utilized here, from wavelengths of 6cm to 3mm, are insufficient to discriminate between the models in most cases. Clearly, simultaneous observations at these wavelengths and at λ1mm would provide a more definitive test of these models. The Maxwellian spectrum would be expected to drop off more rapidly at high frequencies in comparison to the inhomogeneous power law model. Steps have already been taken in this direction (Ennis, Nuegebauer, and Werner 1982), favoring the power law interpretaton.

Within the context of the inhomogeneous jet model, we found that five of the eight sources for which both thick and thin spectral indices could be determined are consistent with jets in which both the particle density and magnetic field fall off as R^{-2}. This is expected in a free relativistic jet in which the field component parallel to the jet axis dominates. One source had $n \alpha R^{-2}$ and $B \alpha R^{-1}$, values expected from a jet in which the perpendicular field component dominates. In large scale radio galaxy jets both situations are seen - in the inner regions of powerful jets B is parallel to the axis, while farther out it becomes perpendicular. This is because the parallel component falls off as R^{-2} while the perpendicular component falls off as R^{-1}. Eventually the latter dominates. In weaker jets, the perpendicular component is always the larger. For a majority of sources in this small sample, then, the derived jet parameters are consistent with what one might expect on the basis of both theory and observation.

The last subject treated in this chapter, the model for 0235+164, has both appealing and negative features. The model does not, without additional assumptions, explain the secondary rise in the flux level at the end of 1981. On the other hand, the model fits the early flux density variations fairly well, and it accounts for the spectral variations with time. Finally, the derived physical parameters of the ambient medium into which the shock propagates seem quite reasonable for conditions expected in the inner few parsecs of a galactic nucleus.

BIBLIOGRAPHY

Chapter II

Balonek, T.J. 1982, Ph.D. Dissertation, Univ. of Massachusetts.

Hobbs, R.W. 1968, Ap.J., 153, 1001.

Hobbs, R.W., and Waak, J.A. 1972, A.J., 77, 342.

Hobbs, R.W., Maran, S.P., and Brown, L.W. 1978, Ap.J., 223, 337 (HMB).

Johnston, K.J., and Hobbs, R.W. 1969, Ap.J., 158, 145.

Kirschbaum, H.S., and Chen, S. 1957, IRE Trans. Mic. Th. and Tech., MTT-5, 199.

Kraus, J.D. 1965, Radio Astronomy, McGraw-Hill.

Martin, D. 1958, Mad Mag., 123, 21.

Penzias, A.A., and Burrus, C.A. 1973, Ann. Rev. Astron. Astrophys., 11, 51.

Ulich, B.L. 1981, A.J., 86, 1619.

Vaucouleurs, G. de, Angione, R., and Fraser, C.W. 1968, Astrophys. Lett., 2, 141.

Wannier, P.G., Scoville, N.Z., Barvainis, R. 1983, Ap.J., 267, 126.

Wardle, J.F.C., and Kronberg, P.P. 1974, Ap.J., 194, 249.

Wilson, A.S. 1972, M.N.R.A.S., 157, 229.

Wright, M.H.C., and Forster, J.R. 1980, Ap.J., 239, 873.

Chapter III

Bologna, J.M., Johnston, K.J., Knowles, S.H., Mango, S.A., and Sloanaker, R.M., 1975, Ap.J., 199, 86.

Bujarrabul, V., and Nguyen-Q-Rieu 1981, Ast.Ap., 102, 65.

Cahn, J.H., and Wyatt, S.P. 1978, Ap.J., 224, L79.

Clarke, R.O., Troland, T.H., and Johnson, D.R. 1983, Ap.J., Submitted.

Clarke, R.O., Waak, J.A.,and Bologna, J.M. 1982, Preprint.

Dickenson, D.F., Reid, M.J., Morris, M., Redman, R. 1978, Ap.J., 220, L113.

Elitzur, M. 1982, Ap.J., 262, 189.

Goldreich, P., Keely, D.A.,and Kwan, J.Y. 1973a, Ap.J., 179, 111.

_____ 1973b, Ap.J., 182, 55.

Kukarin, B.V., et al. 1969, General Catalogue of Variable Stars (3rd ed.; Moscow: Astronomical Council of the Academy of Sciences in the USSR).

Lane, A.P. 1982, Ph.D. Dissertation, Univ. of Massachusetts.

Penzias, A.A., and Burrus, C.A. 1973, Ann.Rev.Astron.Ap, 11, 51.

Reid, M.J. 1976, Ap.J., 207, 784.

Schwartz, P.R., Waak, J.A., and Bologna, J.M. 1979, A.J., 84, 1349.

Troland, T.H., Heiles, C., Johnson, D.R., Clarke, F.O. 1979, Ap.J., 232, 143.

Wardle, J.F.C., and Kronberg, P.P. 1974, Ap.J., 194, 249.

Chapter IV

Bally, J., and Scoville, N.Z. 1982, Ap.J., 225, 497.

Bally, J. 1982, Ap.J., 261, 558.

Barvainis, R., and Predmore, R. 1983, Preprint.

Baud, B., Bieging, J.H., Plambeck, R.L., Thornton, D.D.,, Welch, W.J., and Wright, M.C.H. 1980, in IAU Symposium 87, Interstellar Molecules, ed. B.H. Andrew (Dordrecht: Reidel), p. 545.

Downes, D., Genzel, R., Becklin, E.E., and Wynn-Williams, C.G. 1981, Ap.J., 244, 869.

Elitzur, M. 1982, Ap.J., 262, 189.

Elmegreen, B.G., and Morris, M. 1979, Ap.J., 229, 593.

Goldreich, P., Keely, D.A., and Kwan, J.Y. 1973, Ap.J., 179, 111.

Lane, A.P. 1982, Ph.D. Dissertation, University of Massachusetts.

Morris, M., Bowers, P.F., and Turner, B.E. 1982, Ap.J., 259, 625.

Norris, R.P., Desmond, P.J., and Booth, R.S. 1982, Nature, 299, 131.

Plambeck, R.L., Wright, M.C.H., Welch, J.H., Bieging, J.H., Baud, B., Ho, P.T.P., and Vogel, S.N. 1982, Ap.J., 259, 617.

Snyder, L.E., and Buhl, D. 1974, Ap.J., 189, L31.

Troland, T.H., Hieles, C., Johnson, D.R., and Clarke, F.O. 1979, Ap.J., 194, 249.

Van Blerkom, D., and Auer, L. 1976, Ap.J., 206, 775.

Wright, M.C.H., and Plambeck, R.L. 1983, Preprint.

Wright, M.C.H., Plambeck, R.L., Vogel, S.N., HO, P.T.P., and Welch, W.J. 1983, Ap.J.(Letters), 267, L41.

Chapter V

Aller, H.D. 1968, Ph.D. Dissertation, Univ. of Michigan.

Aller, H.D. 1970, Ap.J. 161, 1.

Aller, H.D., Aller, M.F., and Hodge, P.E. 1981, A.J., 86, 325.

Aller, H.D., Hodge, P.E., and Aller, M.F. 1981, in Extragalactic Radio Sources, IAU symposium No. 97, edited by D. Heeschen and M. Wade (D. Reidel).

Aller, H.D., and Olsen, E.T. 1971, A.J., 76, 671.

Altshuler, D.R., and Wardle, J.F.C. 1976, M.N.R.A.S, 82, 1-67.

Altshuler, D.R., and Wardle, J.F.C. 1977, M.N.R.A.S., 179, 153.

Altshuler, D.R. 1980, A.J., 85, 1559.

Andrew, B.H., Macleod, J.M., Harvey, G.A., and Medd, W.J. 1978, A.J., 83, 863.

Angel, J.R.P., and Stockman, H.S. 1980, Ann. Rev. Astron. Astrophys., 18, 321.

Balonek, T.J. 1982, Ph.D. Dissertation, Univ. of Massachusetts.

Dent, W.A., and Kapitsky, J.E. 1976, A.J., 81, 1053.

Dent, W.A., and Balonek, T.J. 1983, Private communication.

Dent, W.A. 1982, Private communication.

Epstein, E.E., Landau, R., and Rather, J.D.G. 1980, A.J., 85, 1427.

Epstein, E.E., Forgarty, W.G., Mottmann, J., and Schneider, E. 1982, A.J., 87,449 (EFMS).

Fomalont, E.B., Bridle, A.H., Willis, A.G., and Perley, R.A. 1980, Ap.J., 237, 418.

Hjellming, R.M., and Johnston, K.J. 1981, Nature, 290, 100.

Hobbs, R.W., and Dent, W.A. 1977, A.J., 82, 257.

Hobbs, R.W., Maran, S.P., and Brown, L.W. 1978, Ap.J., 223, 337 (HMB).

Impey, C.D., Brand, P.W.J.L., and Tapia, S. 1982, M.N.R.A.S, 198, 1.

Impey, C.D., Brand, P.W.J.L., Wolstencroft, R.D., and Williams, P.M. 1981, M.N.R.A.S., 200, 19.

Jones, T.W., and Rudnick, L. 1979, B.A.A.S., 11, 619.

Jones, T.W. 1981, in Low Frequency Variability of Extragalactic Radio Sources, edited by W.D. Cotton and S.R. Spangler (Publications Division, NRAO).

Kinman, T.D. 1978, in Pittsburgh Conference on BL Lac Objects, edited by A.M. Wolfe (University of Pittsburg).

Ledden, J.E., Aller, H.D., and Dent, W.A. 1976, Nature, 260, 752.

Ledden, J.E., and Aller, H.D. 1979, Ap.J. Lett., 229, L1.

Marsher, A.P. 1980, Ap.J., 235, 386.

Moore, R.L., and Stockman,H.S. 1981, Ap.J., 243, 60.

Padrielli, L. 1981, in Low Frequency Variability of Extragalactic Radio Sources, edited by W.D. Cotton amd S.R. Spangler (Publications Division, NRAO).

Pauliny Toth, I.I.K., Preuss, E., Witzel, A., Graham, D., Kellerman, K.I., Ronnang, B. 1981, A.J., 86, 371.

Pearson, T.J., Unwin, S.C., Cohen, M.H., Linfield, R.P., Readhead, A.C.S, Seielstad, G.A., Simon, R.S., and Walker, R.C. 1981, Nature, 290, 365.

Rees, M.J. 1981, in Extragalactic Radio Sources, IAU Symposium No. 97, edited by D. Heeschen and M. Wade (D. Reidel).

Rudnick, L., Owen, F.N., Jones, T.W., Puschell, J.J., and Stein, W.A.

1978, Ap.J. Lett., 225, L5.

Seielstad, G.A., and Berge, G.L. 1975, A.J., 80, 271.

Tabara, H., and Inoue, M. 1978,

Unwin, S.C., Cohen, M.H., Pearson, T.J., Seielstad, G.A., Simon, R.S., Linfield, R.P., Walker, R.C. 1983, Ap.J., 271, 536.

Wardle, J.F.C., and Kronberg, P.P. 1974, Ap.J., 194, 249.

Wardle, J.F.C. 1978, in Pittsburgh Conference on BL Lac Objects, edited by A.M. Wolfe (University of Pittsburg).

Chapter VI

Blandford, R.D., and Konigl,A. 1979, Ap.J., 232, 34.

Blandford, R.D., and Mckee, C.F. 1976, Phys. Fluids, 19, 1130 (BMI).

_____ 1977, M.N.R.A.S., 180, 343 (BMII).

Blandford, R.W., and Rees, M.J. 1974, M.N.R.A.S., 169, 395.

_____ 1978, in Pittsburg Conference on BL Lac Objects, edited by A.M. Wolfe (University of Pittsburg).

Burbidge, G.R., Jones, T.W., and O'Dell, S.L. 1974, Ap.J., 193, 43.

Cook, D.B., and Spangler, S.R. 1980, Ap.J., 240, 751.

Cotten, W.D., Wittels, J.J., Shapiro, I.I., Marcaide, J., Owen, F.N., Spangler, S.R., Ruis, A., Angulo, C., Clark, T.A., and Knight, C.A. 1980, Ap.J., 238, L123.

deBruyn, A.G. 1976, Astr. and Ap., 52, 439.

Ennis, D.J., Neugebauer, G., and Werner, M. 1982, Ap.J., 262, 460.

Jones, T.W., and Hardee, P.E. 1979, Ap.J., 228, 268.

Jones, T.W., and O'dell, S.L. 1977, Ap.J., 214, 522.

Jones, T.W., Rudnick, L., Owen, F.N., Puschell, J.J, Ennis, D.J., and

Werner, M.W. 1981, Ap.J., 243, 97.

Kellerman, K.I., and Pauliny-Toth, I.I.K. 1968, Ann. Rev. Astron. Ap., 6, 417.

_____ 1981, Ann. Rev. Astron. Ap., 19, 373.

Konigl, A. 1981, Ap.J., 243, 700.

Ledden, J.E., Aller, H.D., and Dent, W.A. 1976, Nature, 260, 752.

Ledden, J.E., and Aller, H.D. 1979, Ap.J., 229, L1.

Marscher, A.P. 1977a, Ap.J., 216, 244.

_____ 1977b, A.J., 82, 871.

_____ 1978, Ap.J., 224, 816.

Ozernoi, L.M., and Sazanov, V.N. 1969, Astrophys. Space Sci., 3, 395.

O'dea, C.P., Dent, W.A., and Balonek, T.J. 1983, to be published in Ap.J., March 1, 1984.

Peterson, L.W., and Dent, W.D. 1973, Ap.J., 186, 421.

Pacini, F., and Salvati, D. 1981, in Extragalactic Radio Sources, IAU Symposium 97, edited by D. Heeschen and M. Wade (D. Reidel).

Rees, M.J. 1981, in Extragalactic Radio Sources, IAU Symposium No. 97, edited by D. Heeschen and M. Wade (D. Reidel)

Spangler, S.R. 1980, Ap. Lett., 20, 123.

Spangler, S.R., Benson, J.M., Cordes, J.M., Hall, R.B., Jones, T.W., and Johnston, K.J. 1981, A.J., 86, 1155.

van der Laan, H. 1966, Nature, 211, 1131.